Functional characterization of the Ca^{2+}-activated Cl^{-} channel Ano2 in the olfactory system

---

Inaugural-Dissertation to obtain the academic degree
Doctor rerum naturalium (Dr. rer. nat.)

submitted to the Department of Biology, Chemistry and Pharmacy
of Freie Universität Berlin

by
Gwendolyn Billig
from Berlin

October 2011

This work was prepared from 1st September 2008 to 31 Oktober 2011 under the supervision of Prof. Dr. Dr. Thomas J. Jentsch at the Max-Delbrück-Centrum für Molekulare Medizin (MDC) and the Leibniz-Institut für Molekulare Pharmakologie (FMP) in Berlin.

1st Reviewer: **Prof. Dr. Dr. Thomas J. Jentsch**
Department Physiology and Pathology of Ion Transport
Max-Delbrück-Centrum für Molekulare Medizin (MDC) and Leibniz-Institut für Molekulare Pharmakologie (FMP), Berlin

2nd Reviewer: **Prof. Dr. Volker Haucke**
Institute for Chemistry and Biochemistry
Department of Biology, Chemistry and Pharmacy
Freie Universität Berlin

Date of defense: February 10, 2012

PREFACE

Part of this work has been published in:
Billig, G. M., Pál, B., Fidzinski, P., and Jentsch, T. J. (2011). Ca^{2+}-activated Cl^{-} currents are dispensable for olfaction. Nat. Neurosci 14, 763–769.

Part of the experimental data shown in this work were done by Balázs Pál and Pawel Fidzinski: Balázs Pál designed, performed and evaluated electro-olfactogram measurements, patch-clamp measurements and measurements with Cl^{-}-sensitive microelectrodes. Patch-clamp measurements with flash photolysis were designed, performed and evaluated by Balázs Pál and Pawel Fidzinski.

TABLE OF CONTENTS

LIST OF FIGURES

LIST OF TABLES

LIST OF ABBREVATIONS

ACIII	adenylate cyclase 3
Ano	anoctamin
ATP	adenosine triphosphate
bp	base pair
CaCC	Ca^{2+}-activated Cl^{-} channel
CaM	calmodulin
cAMP	cyclic adenosine monophosphate
cDNA	copy DNA, reverse-transcribed mRNA
cGMP	cyclic guanosine monophosphate
CNG	cyclic nucleotide–gated channel
Cre	Cre recombinase
C-terminal	carboxy-terminal
DCDPC	3’,5-dichlorodiphenylamine-2-carboxylic acid
DIDS	4,4’-diisothiocyanatostilbene-2,2’-disulfonic acid
DNA	deoxyribonucleic acid
DNase	deoxyribonuclease
dNTP	deoxyribonucleoside triphosphate
DRG	dorsal root ganglion
EDX	energy-disperse X-ray
EOG	electro-olfactogram
ES cell	embryonic stem cell
EST	expressed sequence tag
FLPe	enhanced flippase recombination enzyme
FRT site	flippase recognition target site
GC-D	Guanylate cyclase D
GFP	green fluorescent protein
GG	Grüneberg ganglion
G_i	inhibitory guanine nucleotide-binding protein with subunit α_i
G_o	inhibitory guanine nucleotide-binding protein with subunit α_o
G-olf	olfactory G protein
GPCR	G-protein coupled receptor
G_s	stimulatory guanine nucleotide-binding protein with subunit α_s
$G_{\beta/\gamma}$	guanine nucleotide-binding protein subunit β/γ
h	hour(s)
HEK cells	human embryonic kidney cells
HEPES	4-(2-hydroxyethyl)-1-piperazineethanesulfonic acid
HRP	horseradish peroxidase
IRES	internal ribosome entry site
KCC	$K^{+}Cl^{-}$ co-transporter
kDa	kilodalton
LacZ	bacterial gene for β-galactosidase
min	minute(s)
MOE	main olfactory epithelium

MPP4	membrane palmitoylated protein-4
mRNA	messenger ribonucleic acid
NCKX	$Na^+/Ca^{2+}-K^+$ exchanger
NCX	Na^+/Ca^{2+} exchanger
NFA	niflumic acid
Nkcc	$Na^+K^+2Cl^-$ co-transporter
NPPB	5-nitro-2-(3-phenylpropylamino) benzoic acid
N-terminal	amino-terminal
OMIM	Online Mendelian Inheritance in Man
OMP	olfactory marker protein
OPL	outer plexiform layer
OR	odorant receptor
OSN	olfactory sensory neuron
P	p-value
PBS	phosphate-buffered saline
PCR	polymerase chain reaction
PDZ	PSD-95, Dlg1 (Drosophila disc large tumor suppressor), ZO-1 (zonula occludens-1 protein)
PIP_2	phosphatidylinositol 4,5-bisphosphate
PLC	phospholipase C
PMCA	plasma membrane Ca^{2+}-ATPase
PSD-95	post-synaptic density protein 95
qRT-PCR	quantitative real-time PCR
RE	respiratory epithelium
RNA	ribonucleic acid
RT-PCR	reverse transcriptase PCR
s.e.m.	standard error of the mean
SDS	sodium dodecyl sulfate
SITS	4-acetamido-4’-isothiocyanostilbene-2,2’-disulphonic acid
SOM	septal organ of Masera
TMC	transmembrane channel-like protein
TMEM16	transmembrane protein of unknown function 16
TMS	transmembrane segment
TRPC2	transient receptor potential cation channel, subfamily C, member 2
V1R	vomeronasal receptor type I
V2R	vomeronasal receptor type II
VNO	vomeronasal organ
VSN	vomeronasal sensory neuron

SI units and SI prefixes are used according to the International System of Units.

Nomenclature and symbolism for amino acids and peptides follows the guidelines of the IUPAC-IUB Joint Commission on Biochemical Nomenclature (JCBN): “Nomenclature and symbolism for amino acids and peptides. Recommendations 1983.”.

ABSTRACT

Functional characterization of the Ca^{2+}-activated Cl^{-} channel Ano2 in the olfactory system.

Ca^{2+}-activated Cl^{-} currents have been described in a plethora of physiological processes including sensory transduction. In olfaction, Ca^{2+}-activated Cl^{-} channels (CaCCs) are thought to play a crucial role as amplifiers of the olfactory signal. Binding of odorants to olfactory sensory neurons (OSNs) generates a primary transduction current that is mediated by cyclic nucleotide-gated (CNG) channels. The concomitant Ca^{2+} influx then activates CaCCs that may account for up to 90% of the total receptor current. However, the unknown molecular identity of the underlying channel has precluded direct functional testing. Recently, Ano1 (Anoctamin-1, Tmem16a) has been cloned as the first *bona fide* CaCC with physiological functions in fluid secretion and smooth muscle contraction. Ano2 (Anoctamin-2, Tmem16b) is its closest homolog and likewise gives rise to Ca^{2+}-activated Cl^{-} currents. A physiological role of Ano2, though, has not been explored yet.

We investigated the function of Ano2 in mice and identified Ano2 as the CaCC of the olfactory transduction cascade. Expression of Ano2 was restricted to neuronal tissues with highest levels in the two sensory systems of smell and vision and low expression in several brain regions. In the olfactory system, the Ano2 channel localized to sensory cilia of olfactory neurons in the main olfactory epithelium (MOE) and to microvilli of sensory neurons in the vomeronasal organ (VNO). In the VNO, as in the retina, Ano2 co-localized with the related CaCC Ano1 which otherwise was mainly detected in apical membranes of glandular cells, consistent with its function in epithelial secretion.

Disruption of *Ano2* in mice abolished Ca^{2+}-activated Cl^{-} currents in the MOE and the VNO. Surprisingly, the loss of CaCC activity from OSNs only moderately affected the receptor potential in electro-olfactogram (EOG) recordings. Odor responses were reduced by ~40% in the fluid-phase configuration, while in air-phase EOGs we could not detect any changes. Neuronal input activity to the olfactory bulb and convergence of OSN axons to the olfactory glomeruli, where Ano2 is also located, were unchanged. Consistently, *Ano2*$^{-/-}$ mice showed normal olfaction-guided behaviors and did perform undistinguishable from their littermates in olfactory behavioral tasks. Neither olfactory discrimination ability nor odor sensitivity was affected. Our results show that CNG channels do not need a boost by CaCC to achieve near-physiological levels of olfaction. We conclude that in contrast to the prevailing view, Ca^{2+}-activated Cl^{-} currents are dispensable for olfactory signaling.

ZUSAMMENFASSUNG

Funktionelle Charakterisierung des Ca^{2+}-aktivierten Cl^{-}-Kanals Ano2 im olfaktorischen System.

Ca^{2+}-aktivierte Cl^{-}-Ströme sind an vielen physiologischen Prozessen beteiligt und wurden unter anderem in der Signaltransduktion sensorischer Systeme beschrieben. Besonders im Riechprozess wird ihnen eine essentielle Rolle als Verstärker des Geruchssignals zugeschrieben. Die Bindung von Geruchsstoffen an Riechneurone führt zur Aktivierung eines cAMP-kontrollierten Kationenkanals, der einen primären Transduktionsstrom vermittelt und unter anderem zu Ca^{2+}-Einstrom führt. Ca^{2+} wiederum aktiviert einen Ca^{2+}-aktivierten Cl^{-}-Kanal, von dem angenommen wird, dass er etwa 90% des gesamten Rezeptorstroms ausmacht. Da man die molekulare Identität dieses Kanals nicht kennt, konnte der Mechanismus bisher nicht funktionell überprüft werden. Kürzlich wurde Ano1 (Anoctamin-1, Tmem16a) als erster Ca^{2+}-aktivierter Cl^{-}-Kanal kloniert und konnte als essentielle Komponente der Flüssigkeitssekretion in Epithelien und der Kontraktion glatter Muskulatur identifiziert werden. Ano2 (Anoctamin-2, Tmem16b) ist ein eng verwandtes Homolog von Ano1 und vermittelt ebenfalls Ca^{2+}-aktivierte Cl^{-}-Ströme. Seine physiologische Funktion wurde jedoch bisher nicht untersucht.

In dieser Arbeit wurde die Expression und Funktion von Ano2 in Mäusen charakterisiert und Ano2 als der Ca^{2+}-aktivierte Cl^{-}-Kanal des Riechens identifiziert. Das Ano2-Protein konnte in den sensorischen Systemen des Riechens und Sehens sowie in geringen Mengen in spezifischen Gehirnregionen nachgewiesen werden. Im olfaktorischen System wurde der Ano2-Kanal in sensorischen Zilien der Riechneuronen und in sensorischen Mikrovilli des Vomeronasalorgans lokalisiert. Ausschließlich im Vomeronasalorgan und in der Retina kolokalisierte Ano2 mit dem verwandten Ano1-Kanal. Dieser war in der Nase außerdem prominent in Drüsenzellen exprimiert.

In *Ano2* Knockout-Mäusen konnten im Riechepithel und im VNO keine Ca^{2+}-aktivierten Cl^{-}-Ströme mehr nachgewiesen werden. Überraschenderweise führte der Verlust dieser Ströme nur zu einer moderaten Beeinträchtigung des Rezeptorpotentials in Elektroolfaktogramm (EOG)-Messungen. In der Flüssigphasen-Konfiguration des EOGs waren die Geruchsantworten um ~40% reduziert, während in der Luftphasen-Konfiguration kein Unterschied erkennbar war. Neuronale Input-Aktivität zum olfaktorischen Bulbus sowie die Konvergenz von Riechneuronen auf olfaktorische Glomeruli waren unverändert. In Übereinstimmung dazu zeigten *Ano2*$^{-/-}$ Mäuse keine Störungen des geruchsgesteuerten Verhaltens und schnitten in olfaktometrischen Tests normal ab. Weder die Fähigkeit zur Unterscheidung von Gerüchen noch die Detektionsgrenze für Geruchstoffe waren hier

beeinträchtigt. Unsere Ergebnisse zeigen, dass der primäre Rezeptorstrom durch cAMP-gesteuerte Kanäle keine Verstärkung durch Ca^{2+}-aktivierte Cl^{-}-Kanäle benötigt, um eine fast-physiologische Funktion des Geruchssinnes zu gewährleisten. Wir schlussfolgern, dass Ca^{2+}-aktivierte Cl^{-}-Ströme für die olfaktorische Signalverarbeitung entbehrlich sind.

1. INTRODUCTION

1.1. Ca^{2+}-activated Cl^{-} channels

Ca^{2+}-activated Cl^{-} channels (CaCCs) are activated by increases in intracellular Ca^{2+} concentrations. Their currents have been described in many physiological processes, including secretion from glands and epithelial cells, contraction of cardiac and smooth muscle, regulation of neuronal excitability and transduction of sensory stimuli (Hartzell et al., 2005). While Ca^{2+}-activated Cl^{-} currents have been studied by electrophysiologists since the early 1980s, the underlying channel proteins have remained in question and their physiological roles in many tissues are still elusive (Hartzell et al., 2005). In 2008, Ano1 (Anoctamin 1, TMEM16A) has been identified as a major component of CaCCs (Yang et al., 2008; Caputo et al., 2008; Schroeder et al., 2008) and, by now, it is apparent that at least part of the physiologically described Ca^{2+}-activated Cl^{-} currents are mediated by Ano1 and presumably by additional members of the *Anoctamin* gene family (Duran and Hartzell, 2011).

Depending on the electrochemical driving force for Cl^{-} across the membrane, opening of CaCCs results in either efflux or influx of Cl^{-}. In excitable cells, this corresponds to depolarization and hyper- and repolarization, respectively, and CaCCs are involved in regulating cell excitability. In non-excitable cells such as secretory epithelia, opening of CaCCs and concomitant Cl^{-} efflux triggers fluid secretion. Yet, in many cell types, the physiological outcome of CaCC activity is difficult to predict since Cl^{-} concentration gradients across the cell membrane are unknown. Detailed functional characterization is also hampered by the co-existence of Ca^{2+}-activated Cl^{-} currents with Ca^{2+}-activated cation currents and other Cl^{-} currents, the lack of specific inhibitors and, frequently, the unknown molecular identity.

CaCCs have been primarily described in epithelia, smooth muscle cells and in the sensory and nervous system (Hartzell et al., 2005). In epithelia, where intracellular Cl^{-} is high, CaCCs mediate fluid secretion. When apically located CaCCs are activated, Cl^{-} ions exit and Na^{+} ions follow passively resulting in the net secretion of NaCl and transepithelial water transport. Thus, epithelial CaCCs are assumed to play a key role in exocrine secretion in many types of glands and in hydration of the airway surface (Kidd and Thorn, 2000; Melvin et al., 2005). In smooth muscle cells, CaCC activity is thought to be depolarizing (Leblanc et al., 2005). Thus, when CaCCs open the concomitant depolarization favors activation of voltage-gated Ca^{2+} channels that mediate further Ca^{2+} influx and thereby increase muscle contraction.

CaCCs have also been identified in the sensory, the somatosensory and the central nervous system of many species including mammals and amphibians. Yet, the function of CaCCs in most neurons is poorly established. They have been speculated to underlie a variety of neuronal activities, such as sustained or transient depolarizations and hyper- and repolarizations (Scott et al., 1995; Frings et al., 2000). Olfactory sensory neurons (OSNs) are one of the few types of neurons in which Ca^{2+}-activated Cl^- currents have been extensively studied. Here, CaCCs mediate depolarization and are thought to play a key role in the amplification of the initial receptor current (see chapter 1.3.1.3). By contrast, in taste cells CaCCs seem to act hyperpolarizing and might contribute to adaptation (Taylor and Roper, 1994; Herness and Sun, 1999). Ca^{2+}-activated Cl^- currents have also been found in a variety of neurons and glia cells of the retina. They have been most prominently studied in photoreceptors where they activate in response to depolarization-evoked Ca^{2+} influx during the dark current. It is thought that CaCCs are involved in stabilizing the presynaptic membrane potential during synaptic activity (Lalonde et al., 2008).

In the somatosensory system Ca^{2+}-activated Cl^- currents have been described in subsets of dorsal root ganglion (DRG) neurons, spinal cord neurons, and autonomic neurons (Frings et al., 2000). In DRGs, where intracellular Cl^- is high, CaCCs have been suggested to be responsible for after-depolarizations following action potentials. In contrast, in spinal cord neurons intracellular Cl^- is low and here activation of CaCCs would stabilize the resting membrane potential or hyperpolarize the cell membrane. Thus, considering the slow inactivation kinetics of the CaCCs, they might limit repetitive firing and trains of action potentials in these cells. Other cell types, in which Ca^{2+}-activated Cl^- currents have been measured include vascular endothelial cells, Sertoli cells, mast cells, neutrophils, lymphocytes, brown fat adipocytes, cardiac myocytes, kidney cells and hepatocytes (Hartzell et al., 2005). In most of these tissues a physiological function for CaCCs has not been assigned yet.

Even though biophysical properties of CaCCs are not homogenous among different cells and tissues, some hallmark features common to native Ca^{2+}-activated Cl^- currents in many tissues have been identified (Hartzell et al., 2005). These “classical” CaCCs are characterized by a Ca^{2+}-controlled voltage-dependence. At non-maximal Ca^{2+} concentrations they are slowly activating and show outward rectification. Elevation of intracellular free Ca^{2+} progressively shifts the voltage-dependence to negative potentials until the current-voltage relationship becomes linear at saturating free Ca^{2+} levels. Specific inhibitors and activators for CaCCs are lacking but pharmacological sensitivity to a panel of inhibitors such as niflumic acid (NFA) and NPPB at low micromolar concentrations has been consistently described. The mechanisms underlying activation of CaCCs by Ca^{2+} are unknown and discrepant findings have been reported possibly reflecting heterogeneity of the underlying channels. Mechanisms described include activation by direct binding of Ca^{2+} as well as indirect activation by calmodulin (CaM) and by Ca^{2+}-dependent phosphorylation (Arreola et al., 1998; Kuruma and Hartzell, 2000; Park et al., 2001). Physiologically, the rise in intracellular free Ca^{2+} that triggers CaCC activity can be mediated either by Ca^{2+} entry through voltage- and ligand-gated channels or by release of Ca^{2+} from intracellular stores.

1.2. The *Anoctamin* gene family

1.2.1. Functions of Anoctamins

Members of the *Anoctamin* family are found throughout the eukaryotes, including protozoa, yeast, fly, worms, amphibians, reptiles, birds and mammals and are best represented in higher vertebrates (Milenkovic et al., 2010). In mammals, the *Anoctamin* (*TMEM16*) gene family comprises ten members, *Ano1–10* or *TMEM16A–K*, respectively (Yang et al., 2008; Schroeder et al., 2008; Hartzell et al., 2009). Ano1 and Ano2 are close homologs with ~60% sequence identity in the human proteins. Together with Ano3 and Ano4 as well as Ano5 and Ano6, that each are closely related, they represent one subgroup of the Anoctamin proteins. Ano7 and Ano9 are more distantly related (Figure 1). The close homologs Ano8 and Ano10 form the most divergent subgroup. They have only ~20% sequence identity with Ano1 and lack protein features shared by the rest of the protein family. Maximal conservation among the Anoctamin proteins is found in the predicted transmembrane segments.

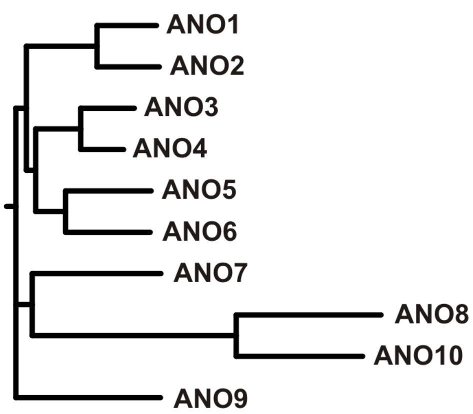

Figure 1 | Phylogeny of the human Anoctamin protein family.
Neighbor-joining phylogenetic tree of the human TMEM16 protein family calculated with the Protdist program. Accession numbers of RefSeq protein sequences used:
ANO1–ANO10; NP_060513.5, NP_065106.2, NP_113606.2, NP_849148.2, NP_998764.1, NP_001020527.2, NP_001001891.2, NP_066010.1, NP_060545.3, NP_001012302.2.

Ano1 and Ano2 have been shown to function as CaCCs. However, it is uncertain if all Anoctamin family members represent CaCCs (Duran and Hartzell, 2011), especially since alternative functions, including scramblase (Suzuki et al., 2010) as well as cation channel activity (Yang et al., 2011) for Ano6, have been suggested and electrophysiological measurements of Anoctamin members apart from Ano1 and Ano2 have been rarely reported (Schreiber et al., 2010; Yang et al., 2011).

The physiological importance of the *Anoctamin* family has been highlighted by the phenotypes associated with mutations of these genes in humans. Mutations of *ANO6* cause Scott syndrome, a rare bleeding disorder in which coagulation is disturbed (Suzuki et al., 2010), while mutations in *ANO5* underlie gnathodiaphyseal dysplasia (Tsutsumi et al., 2004) and several forms of muscular dystrophy (Bolduc et al., 2010). Mutations in *ANO10* are associated with a form of cerebellar ataxia (Vermeer et al., 2010). Notably, *ANO1* is highly expressed in some human cancers but its importance for cancer development is unclear (Ferrera et al., 2010). In mice, deletion of *Ano1* causes early postnatal death presumably due to asphyxia as a consequence of tracheal malformation and mucus accumulation (Rock et al., 2008, 2009). An overview of the reported functional activities of Anoctamins as well as their main expression sites and associated human diseases, as far as known, is given in Table 1.

Table 1 | The Anoctamin protein family: expression and function.

	Functional activity	Main expression	Human disease	Knock-out mouse model
ANO1 (TMEM16A)	CaCC	epithelia, smooth muscle	?	postnatal death (tracheal malformation, mucus accumulation)
ANO2 (TMEM16B)	CaCC	sensory neurons	?	see this work
ANO3 (TMEM16C)	?	nervous system	?	n/a
ANO4 (TMEM16D)	?	nervous system	?	n/a
ANO5 (TMEM16E)	?	?	muscular dystrophy, GDD*	n/a
ANO6 (TMEM16F)	scramblase, cation channel?	broad	Scott syndrome	n/a
ANO7 (TMEM16G)	?	prostate-specific?	?	n/a
ANO8 (TMEM16H)	?	?	?	n/a
ANO9 (TMEM16J)	?	?	?	n/a
ANO10 (TMEM16K)	?	?	cerebellar ataxia	n/a

* Gnathodiaphyseal dysplasia; n/a, not available

Anoctamins might be evolutionary related to the transmembrane channel-like *(TMC)* gene family (Hahn et al., 2009). Mutations of *TMC* genes are implicated in several human diseases, such as hearing loss and dermatosis (Kurima et al., 2003). However, the functional activity of TMC proteins is not known. Anoctamin and TMC proteins are predicted to share the same membrane topology. Also amino acids in some characteristic protein regions are conserved among both protein families (Hahn et al., 2009) as indicated in Figure 2.

1.2.2. Anoctamin protein structure

Anoctamin proteins are predicted to have eight transmembrane segments with cytoplasmic amino- and carboxytermini (Das et al., 2008; Milenkovic et al., 2010). Most likely, Anoctamin proteins exist as homodimers (Sheridan et al., 2011; Fallah et al., 2011). With the exception of the most distantly related Ano8 and Ano10, the extracellular segment between transmembrane segment (TMS) 5 and 6 is predicted to form a reentrant loop and the following extracellular loop harbors a conserved N-glycosylation site as exemplified in the schematic depiction of the mouse Ano2 protein in Figure 2. A segment around TMS1 represents a putative cyclic nucleotide binding site (Milenkovic et al., 2010) and this region also contains an amino acid stretch which is highly conserved between Anoctamin and TMC proteins (Hahn et al., 2009) [Figure 2].

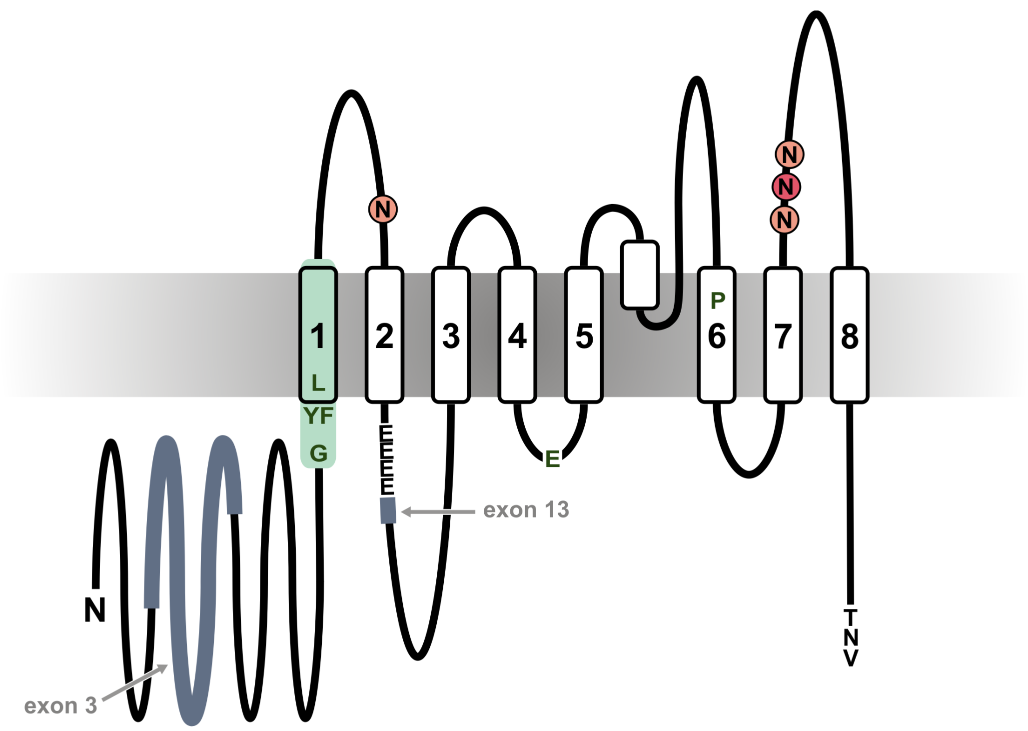

Figure 2 | Membrane topology model and structural elements of murine Ano2.
The 1002 amino acid isoform of mouse Ano2 contains eight predicted transmembrane segments (TMS1-8) and a putative reentrant loop between TMS5 and TMS6. Encircled N in red indicates predicted N-linked glycosylation motifs. The N-glycosylation site highlighted in dark red is highly conserved among Ano1–7 and 9. Skipping of exon 3 and exon 13 (blue) generates Ano2 splice isoforms. Amino acid residues identical among all Anoctamin and TMC proteins are depicted in dark green (Hahn et al., 2009). The light green box represents a putative cyclic nucleotide binding site conserved among Anoctamin proteins Ano1–7 and 9 (Milenkovic et al., 2010). EEEE represents the glutamic acid stretch that might be involved in voltage and Ca^{2+} sensing. TNV is the N-terminal PDZ class I binding motif also found in Ano5 and Ano9.

Even though Ano1 and Ano2 can be directly gated by Ca^{2+}, none of the Anoctamin paralogs harbors classical Ca^{2+} or CaM binding domains. Notably, all Anoctamin proteins with the exception of Ano8 and Ano10 contain an unusual acidic amino acid stretch in the first intracellular loop (Figure 2) that in Ano1 is crucial for voltage sensing (Xiao et al., 2011) and was previously postulated to bind Ca^{2+} similar to the “calcium bowl” of Ca^{2+}-dependent K^+ channels (Yuan et al., 2010). In studies with Ano1 it appeared that the adjacent amino acid stretch EAVK, coded by exon 13, is a key element in Ca^{2+} responsiveness (Xiao et al., 2011). The corresponding sequence in Ano2 is ERSQ, likewise coded by exon 13. As do Ano5 and Ano9, Ano2 bears a C-terminal PDZ class I binding motif that mediates interaction with structural proteins (Stöhr et al., 2009). Ano8 and Ano10 are special in that they do not harbor any predicted N-glycosylation sites. They miss the postulated reentrant loop and do not bear the acidic amino acid stretch in the first intracellular loop. Ano8 though is characterized by a different stretch of ~20 acidic amino acids situated in a region after TMS5. In contrast to Ano10 which with 660 amino acids in mouse, is the smallest protein of the Anoctamin family, Ano8 represents the biggest protein and is characterized and by a very long N-terminus.

Alternative splicing could be a common mechanism to regulate biophysical properties of Anoctamin proteins. Investigation of the electrophysiological properties of Ano1 splicing isoforms in mice shows that exon inclusion or skipping affects Ca^{2+} sensitivity and voltage dependence (Ferrera et al., 2009). For murine Ano2 the presence of tissue-specific splice isoforms that lack exon 3 or exon 13 has been reported as well (Stephan et al., 2009).

1.2.3. The Ca^{2+}-activated Cl^- channel Ano1

Ano1 mediates anion-selective currents upon heterologous expression with biophysical properties similar to the physiologically described “classical” CaCCs (Yang et al., 2008; Schroeder et al., 2008; Hartzell et al., 2009; Romanenko et al., 2010). This includes the characteristic Ca^{2+}-dependent rectification and activation by submicromolar concentrations of Ca^{2+}. At non-maximal Ca^{2+} concentrations of around 0.2 µM Ano1 is slowly activating and shows outward rectification while at high intracellular Ca^{2+} concentrations of >1 µM the current-voltage relationship is linear. Also, blockers commonly used to inhibit Cl^- channels like NFA and NPPB inhibit Ano1. Expression analysis and functional studies with *Ano1*$^{-/-}$ mice have identified Ano1 unambiguously as the CaCC of epithelial cells and smooth muscle cells.

Epithelial cell types that express Ano1 include surface epithelia of the airway and the gastrointestinal tract (Rock et al., 2009; Ousingsawat et al., 2009; Huang et al., 2009) as well as acinar cells from different glands (Ousingsawat et al., 2009; Huang et al., 2009; Romanenko et al., 2010). While expression in airway and gastrointestinal epithelia might be rather low, Ano1 shows prominent expression in apical membranes of acinar cells from submandibular gland, pancreas and submucosal glands of trachea (Ousingsawat et al., 2009; Huang et al., 2009; Romanenko et al., 2010). In these tissues Ano1 can be readily detected in knock-out–controlled immunostainings.

In epithelia of the airway and the gastrointestinal tract Ca^{2+}-activated Cl^{-} currents are thought to be involved in surface liquid homeostasis (Rock et al., 2009; Ousingsawat et al., 2009; Huang et al., 2009). Rock et al. (2009) found that, although Ano1 represents more than 60% of the purinoreceptor-regulated CaCC activity in tracheal epithelium, it contributes little to unstimulated Cl^{-} currents. In agreement with this, Ano1 was found to represent only a minor fraction of total Ca^{2+}-activated Cl^{-} currents in airway and intestinal epithelia in pharmacological studies (Namkung et al., 2011). In contrast, in glandular cells, Ano1 represents the major part of Ca^{2+}-activated Cl^{-} currents. Salivary gland acinar cells from *Ano1*$^{-/-}$ mice lack Ca^{2+}-activated Cl^{-} currents (Romanenko et al., 2010) and specific inhibitors for Ano1 largely abolish Ca^{2+}-activated Cl^{-} currents in wild-type salivary gland (Namkung et al., 2011).

Expression of Ano1 is also well established in smooth muscle and its pacemaker cells. In the gastrointestinal tract Ano1 is specifically expressed in interstitial cells of Cajal (Gomez-Pinilla et al., 2009), the pacemaker cells that control smooth muscle cell contraction, and is essential for slow wave activity (Huang et al., 2009). *Ano1*$^{-/-}$ mice show diminished contraction of gastric smooth muscle. Prominent expression of Ano1 is also found in smooth muscle cells of the airways in knock-out–controlled immunostainings and in smooth muscle cells of the reproductive tract (Huang et al., 2009). In oviduct, Dixon et al. (2011) showed that Ano1 is involved in the generation of electrical slow waves. Additional expression sites reported for Ano1 are bile duct (Dutta et al., 2011), mammary gland (Schroeder et al., 2008), and smooth muscle cells of blood vessels (Davis et al., 2010), as well as retina, dorsal root ganglia (Yang et al., 2008) and cochlea (Jeon et al., 2011).

1.2.4. The Ca^{2+}-activated Cl^{-} channel Ano2

Ano2 is the closest homolog of Ano1 and up to date the only other member of the Anoctamin gene family that has reliably been reported to mediate Ca^{2+}-activated Cl^{-} currents. Its CaCC activity was first shown by Schroeder et al. (2008) in two-electrode voltage-clamp recordings of *Axolotl* oocytes expressing mouse Ano2. More detailed electrophysiological characterization of heterologously expressed mouse and human Ano2 has confirmed its function as CaCC and revealed biophysical properties similar to “classical” CaCCs (Stöhr et al., 2009; Stephan et al., 2009; Pifferi et al., 2009a; Sagheddu et al., 2010). Its functional activity together with its prominent expression in OSNs have established Ano2 as a promising candidate for the molecular identity of the olfactory CaCC (Stephan et al., 2009; Pifferi et al., 2009a; Rasche et al., 2010).

1.2.4.1. Biophysical properties of Ano2

Patch-clamp measurements of HEK cells overexpressing mouse or human Ano2 in the whole-cell (Stöhr et al., 2009; Pifferi et al., 2009a; Rasche et al., 2010; Sagheddu et al., 2010) and in the inside-out configuration (Stephan et al., 2009; Pifferi et al., 2009a) consistently show anion-selective currents that are activated by elevating intracellular Ca^{2+} concentrations – either by stimulating signaling pathways that raise intracellular Ca^{2+}, by adding Ca^{2+} ionophores or by directly adding Ca^{2+} to the cytoplasmic side. The direct activation by Ca^{2+} in the bath solution of inside-out patches and the fast answer after flash photolysis of caged Ca^{2+} indicate direct gating by Ca^{2+}. Yet, there seem to be additional regulators since in inside-out patches Ano2 consistently shows run-down of the CaCC activity after excision. These regulatory factors presumably do not include membrane-bound kinases, phosphatases or CaM since neither addition of inhibitors or activators of these factors nor direct addition of CaM did affect the observed run-down (Pifferi et al., 2009a).

Analysis of current-voltage relationships of Ano2 currents in whole-cell measurements revealed the typical Ca^{2+}-dependent outward rectification known from “classical” native CaCCs. The outward rectification observed at low Ca^{2+} concentrations is gradually lost when intracellular Ca^{2+} increases, and the current-voltage relationship becomes linear. In inside-out patches the rectification characteristics change to inward with high Ca^{2+} concentrations. The underlying mechanism is unknown. The Ca^{2+} sensitivity was estimated from inside-out patch clamp measurements with half-maximal activations of 1.83 µM free Ca^{2+} at -40 mV and 1.18 µM at +40 mV by Stephan et al. (2009) and 4.9 µM at -50 mV and 3.3 µM at +50 mV by Pifferi et al. (2009a). It should be noted that both studies used different isoforms of Ano2. This indicates more effective binding of Ca^{2+} at inside-positive membrane potentials. The Hill coefficient in these measurements was found to be ≥ 2 pointing to at least two binding sites for Ca^{2+} in the channel protein. Ano2 is anion-selective with a characteristic permeability sequence of $I^- > Br^- > Cl^- > F^-$ (Stephan et al., 2009; Pifferi et al., 2009a). The single-channel conductance of Ano2 channels is very low. Values of 0.8 or 1.22 pS (Stephan et al., 2009) and 1.2 pS (Pifferi et al., 2009a) were estimated by noise analysis from inside-out patch clamp measurements. The pharmacological profile was assessed using different compounds commonly used to inhibit CaCC. Ano2 is effectively (~80%) and reversibly blocked by low concentrations of NFA (300 µM) when applied intra- or extracellularly (Stephan et al., 2009; Pifferi et al., 2009a; Sagheddu et al., 2010) while other fenamates (300 µM) block the current much less effectively (Pifferi et al., 2009a).

NPPB (100 µM), DIDS (1 mM) and SITS (5 mM) block moderately when applied from outside but do not block from inside (Pifferi et al., 2009a; Sagheddu et al., 2010).

1.2.4.2. Expression of Ano2

Studies on expression of Ano2 suggest a restricted expression profile for Ano2 with main expression sites in the olfactory system, the retina and possibly the nervous system (Stöhr et al., 2009; Rasche et al., 2010). Expression of Ano2 has been characterized most thoroughly in the rodent olfactory system. Its first description as a transcript highly enriched in OSNs was by Yu et al. (2005) who compared transcripts of FACS-enriched mouse OSNs with OSN-depleted cells of the MOE and identified Ano2 (in that study N64J) as the most highly enriched transcript out of 54 differentially expressed transcripts. Later Ano2 was found as a prominent protein in several proteomic screens of olfactory cilia and olfactory membranes from rat and mouse (Mayer et al., 2009; Stephan et al., 2009; Rasche et al., 2010). Expression in OSNs could be verified by immunohistochemistry using several antibodies for Ano2 which consistently indicated localization in the ciliary layer of the MOE (Rasche et al., 2010; Hengl et al., 2010; Sagheddu et al., 2010). Analogous to the ciliary expression in the MOE Ano2 was found to localize to sensory microvilli of vomeronasal sensory neurons (Rasche et al., 2010). Its expression in the olfactory system suggests that Ano2 might represent the CaCC of the olfactory transduction cascade (Stephan et al., 2009; Pifferi et al., 2009a; Rasche et al., 2010) described in detail in chapter 1.3.1.3.

A second prominent expression site of Ano2 is the retina where it has been originally identified in an EST database screen for retina-specific human transcripts (Stöhr et al., 2000). In immunohistochemistry Ano2 localizes to the sensory endings of photoreceptors in the outer plexiform layer (OPL) of the retina. Here Ano2 interacts via its PDZ binding motif with the scaffolding protein PSD-95 and constitutes part of a larger presynaptic complex (Stöhr et al., 2009). This complex includes two more scaffolding proteins of the membrane associated guanylate kinase (MAGUK) protein family, Veli3 and membrane palmitoylated protein-4 (MPP4), as well as the plasma membrane Ca^{2+}-ATPase (PMCA) that mediates ATP-dependent Ca^{2+} extrusion. When the scaffolding protein MPP4 is deleted in mice, the whole complex including Ano2 is lost from the OPL (Aartsen et al., 2006; Yang et al., 2007; Stöhr et al., 2009). The function of Ano2 at the presynaptic site is unknown.

Data from *in silico* expression analyses, RT-PCR studies on human and mouse tissue as well as immunoblot analysis of mouse brain indicate Ano2 expression additionally in the central nervous system (Stöhr et al., 2009; Rasche et al., 2010). In immunoblots Rasche et al. (2010) did not detect Ano2 in the peripheral nervous system, such the trigeminal nerve and DRGs, even though Ano2 was found in RT-PCR of DRGs from adult tissue (Boudes et al., 2009) and in *in situ* hybridizations of DRGs during mouse embryonic development (Rock and Harfe, 2008). During development expression was also found in the neural tube and in epidermis (Rock and Harfe, 2008). Although publicly available expression data sets and some broader expression studies on *Anoctamin* genes (Schreiber et al., 2010) indicate additional expression sites, particularly in the reproductive and the gastrointestinal system, the presence of Ano2 in these tissues is questionable and has not been confirmed yet.

1.3. The mammalian olfactory system

The sense of smell enables animals to detect and interpret myriads of different odors with great sensitivity and discriminatory power. Olfaction is needed to identify food, to avoid toxic substances and to warn of predators. Moreover, odors convey crucial information on reproductive status, gender and genetic identity of conspecifics and drive innate and learned behaviors important for survival.

In vertebrates, most odors are detected by the main olfactory system. Odorants bind to odorant receptors (ORs) that are expressed on cilia of OSNs in the main olfactory epithelium (MOE) of the nose (Figure 3). In canonical olfactory signal transduction the binding triggers a cAMP-dependent G protein–coupled signal transduction cascade that transduces the chemical signal into a receptor potential (see chapter 1.3.1.3 and Figure 5). The summation of receptor potentials at the soma triggers action potentials that are transmitted via the axons of the OSNs to the main olfactory bulb. Here the odor information is processed and conveyed to higher brain centers, ultimately leading to the perception of smell. In most vertebrates, the nose contains additional olfactory subsystems that are anatomically segregated within the nasal cavity, such the vomeronasal organ (VNO), the only recently discovered Grüneberg Ganglion (GG) and septal organ of Masera (SOM), and additional types of specialized sensory neurons (Figure 3). These subsystems differ in the receptors and signal transduction pathways they use and in the areas of the olfactory bulb they target (reviewed in Su et al., 2009). Even though there is some functional overlap between the olfactory organs, the anatomical and molecular differences reflect functional differences. They are thought to respond to distinct stimuli and to drive specific behavior, yet their exact contributions still need to be dissected.

The VNO and its projections form the accessory olfactory system which has an essential role in chemical communication and regulation of social behaviors. While originally the accessory olfactory system was postulated to detect only non-volatile pheromones and the main olfactory system only volatile, environmental odorants it is now clear that both systems have considerable overlap in the stimuli they detect and the effects they mediate. Canonical signaling in the MOE is necessary for several sexual and social behaviors that likely depend on pheromones, and certain pheromones are able to activate canonical OSNs (Lin et al., 2004; Mandiyan et al., 2005; Xu et al., 2005; Wang et al., 2006; Spehr et al., 2006). Likewise, general odorants not known to act as pheromones can activate vomeronasal sensory neurons (VSNs) and modulate behavior (Baker et al., 1999; Sam et al., 2001; Trinh and Storm, 2003; Xu et al., 2005).

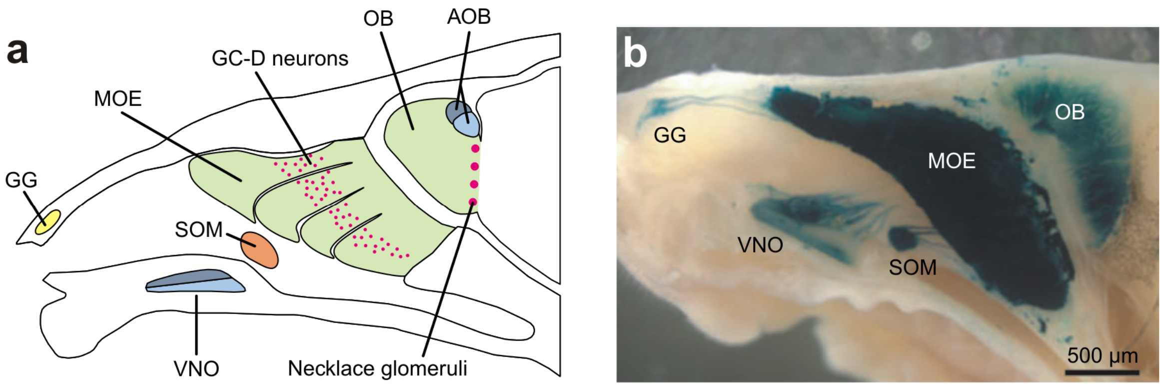

Figure 3 | Anatomical and functional organization of the mouse olfactory system.
(a) Schematic view of a sagittal cut through a mouse head. Most of the posterior part of the nasal cavity is occupied by the main olfactory epithelium (MOE) from where the axons of olfactory receptor cells project to the olfactory bulb (OB). MOE and olfactory bulb together form the main olfactory system. The accessory olfactory system comprises the vomeronasal organ (VNO), a specialized tubular structure in the basal part of the septum, and the accessory olfactory bulb to which the axons of vomeronasal neurons project. Additional olfactory subsystems are the Grueneberg ganglion (GG) located near the tip of the nose and the septal organ of Masera (SOM) which is an isolated patch of sensory epithelium residing on the nasal septum. In the MOE olfactory neurons that express guanylate cyclase D (GC-D) are dispersed in a specific zone from where their axons project to specialized glomeruli of the olfactory bulb known as necklace glomeruli. Modified from Zufall and Munger, 2001. **(b)** X-Gal staining of a sagittal cut through the nose of an *Omp-IRES-tau:LacZ* mouse, which co-expresses olfactory marker protein with LacZ, visualizes all sensory neurons of the olfactory system including their axonal projections to the olfactory bulb. Modified from Storan and Key, 2006.

1.3.1. The main olfactory system

1.3.1.1. Anatomical organization and morphology

In mice, the MOE occupies most of the posterior part of the nasal cavity where it is in direct contact with the inhaled air. The rest of the nasal cavity is lined by respiratory epithelium (RE). The MOE is covered with mucus which is produced by Bowman glands that underlie the MOE and by different nasal glands (Adams, 1992). It is organized as a pseudostratified epithelium made up of three main cell types (Zippel, 1993): OSNs, supporting cells and basal cells.

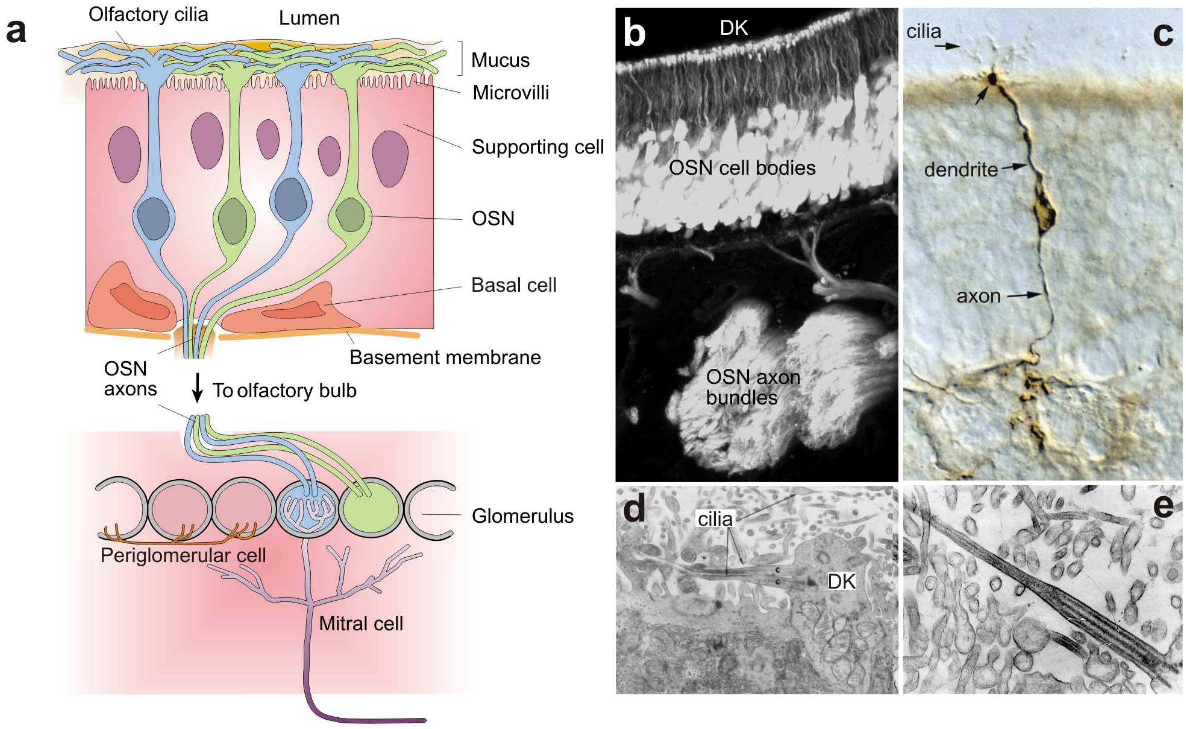

Figure 4 | Morphology and fine structure of the main olfactory system.
(a) Schematic depiction of the main olfactory epithelium (MOE) and its projections to the olfactory bulb. Olfactory sensory neurons (OSN) are bipolar neurons with short dendrites that end in a dendritic knob from which sensory cilia protrude into the mucus layer. OSNs are surrounded by microvillar supporting cells. At the base of the epithelium basal cells continuously regenerate the tissue. OSNs project a long unmyelinated axon to the olfactory bulb, where they synapse in olfactory glomeruli with their second-order neurons, the mitral cells. Inhibitory periglomerular cells connect different glomeruli and regulate olfactory transmission. Each OSN expresses only one type of odorant receptor and OSNs expressing the same receptor project to the same glomerulus as indicated by the blue and green colored OSNs in the scheme. **(b)** Maximum intensity projection of microscopic images from the MOE of an *OMP-tauGFP* mouse that co-expresses OMP and GFP. GFP fluorescence labels the dendrites, the dendritic knobs (DK), the axons and the axon bundles underlying the MOE. **(c)** Peroxidase staining for GFP in the MOE of a transgenic mouse expressing GFP under the OR37A promoter reveals the morphology of a single OSN. **(d,e)** Fine structure of the MOE in electron microscopy. **(d)** The dendritic knob (DK) of an OSN with cilia and neighboring microvillar supporting cells. **(e)** An olfactory cilium with proximal and distal segment. Images are modified from: a, Firestein, 2001; b, Elsaesser and Paysan, 2007; c, Paysan and Breer, 2001; d, Frisch, 1967; e, Seifert and Ule, 1966.

Supporting cells bear microvilli, surround the dendrites of OSNs and may serve a glia-like role. Basal cells are located at the base of the epithelium and represent stem cells from which the tissue is continuously regenerated (Figure 4a). OSNs are bipolar neurons with a long unmyelinated and unbranched axon that projects to the olfactory bulb in the brain, where it synapses with second-order neurons. On their apical side a short dendrite projects to the surface of the MOE where it ends in a terminal enlargement, the dendritic knob. From here numerous sensory cilia protrude into the mucus layer building up an intertwined mat that provides a large interaction surface for odorants (Figure 4a–d). Electron microscopic studies in mice (Seifert and Ule, 1966; Frisch, 1967; Menco, 1997) show that olfactory sensory cilia are 50-60 µm long tapering down from a short and thick proximal segment to a long and thinner distal segment (Figure 4d,e). The ciliary structure not only increases the surface area and the probability of odorant binding, it also establishes a high surface to volume ratio allowing large concentration changes with a limited variation in the number of molecules. Although, in mammals, olfactory cilia are non-motile they have the (9+2) microtubuli configuration in the proximal axoneme that is characteristic for motile cilia (Figure 4d). It is in the ciliary membrane that all the components of the olfactory signal transduction are structurally organized and strongly enriched. Here, the initial events of transduction take place.

1.3.1.2. Canonical olfactory signal transduction

The canonical signaling pathway of OSNs converts the chemical signal of an odorant into electrical activity (Firestein and Werblin, 1989). Olfactory signaling is triggered when odors partition from the air into the olfactory mucus and bind to ORs in the membrane of olfactory cilia. Each canonical OSN expresses one out of hundreds of distinct ORs that in vertebrates form the largest family of G protein-coupled receptors (GPCRs) and comprise ~250–1200 functional OR genes (Niimura and Nei, 2007). One can distinguish class I and II ORs which are tuned toward water-soluble and hydrophobic odors, respectively. Binding of an odorant to an OR is transduced into an electrical signal via the sequential activation of three major signaling proteins. ORs trigger activation of the olfactory G-protein (G-olf), an olfactory isoform of the stimulatory G_s protein (Jones and Reed, 1989), which in turn activates the MOE-specific (Bakalyar and Reed, 1990) adenylate cyclase type III (ACIII) leading to the production of cAMP. The intracellular rise in cAMP then opens cyclic nucleotide-gated (CNG) cation channels that allow for influx of Na^+ and Ca^{2+} from the mucus into the ciliary lumen thereby depolarizing the ciliary membrane. In the classical model of olfactory signal transduction an additional crucial amplification step follows the initial depolarization by CNG channels: the influx of Ca^{2+} activates CaCCs that mediate a secondary depolarizing Cl^- efflux which accounts for the majority of the receptor current (see chapter 1.3.1.3). The transduction current carried by these olfactory ion channels induces slow and graded receptor potentials which summate at the soma and, upon reaching the threshold level, eventually trigger action potentials and neuronal activity.

Canonical olfactory signal transduction has been intensively studied and its importance for olfaction has been clearly established by knock-outs of its major genes. In OSNs from mice lacking G-olf (Belluscio et al., 1998), ACIII (Wong et al., 2000; Wang et al.,

2006) or the α-subunit of the CNG channel Cnga2 (Brunet et al., 1996; Mandiyan et al., 2005), receptor potentials in response to odorants are virtually abolished in electro-olfactogram measurements. These knock-out mice show major deficits in olfactory behavioral tasks and different odor-guided behaviors are impaired. This includes the lack of suckling behavior, which manifests in high postnatal death rates due to the inability to feed, and deficits in sexual and aggressive behavior that have been reported for *Cnga2* and *AC3* knock-out mice (Mandiyan et al., 2005; Wang et al., 2006). The lack of olfactory input in these mice is also reflected in reduced expression of activity-dependent markers in the olfactory bulb (Baker et al., 1999; Trinh and Storm, 2003). While in *AC3*$^{-/-}$ mice axonal projection patterns of OSNs to the olfactory bulb (Zou et al., 2007) are disturbed, they are normal or almost normal in *G-olf* (Belluscio et al., 1998) and *Cnga2*$^{-/-}$ mice (Lin et al., 2000; Zheng et al., 2000).

The olfactory CNG channel is assembled from three different subunits: the major subunit CNGA2 and the auxiliary subunits CNGA4 and CNGB1β (Bönigk et al., 1999; Bradley et al., 2001; Zheng and Zagotta, 2004) with the latter two being important for cAMP sensitivity, CaM-mediated desensitization and for proper ciliary localization (Liman and Buck, 1994; Bönigk et al., 1999; Bradley et al., 2001; Munger et al., 2001; Zheng and Zagotta, 2004; Michalakis et al., 2006; Song et al., 2008).

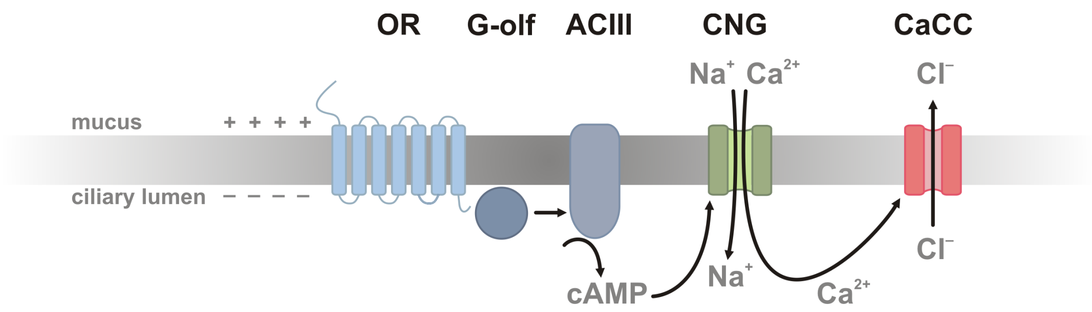

Figure 5 | Canonical olfactory signal transduction.
Binding of odorants to the olfactory receptor (OR) results in activation of G-olf, the stimulatory α-subunit of the olfactory G protein. Activated G-olf binds to adenylate cyclase III (ACIII) and triggers cAMP production. The increase in intracellular cAMP leads to opening of cyclic nucleotide-gated (CNG) channels allowing for the influx of Na^+ and Ca^{2+} into the ciliary lumen and resulting in depolarization. The concomitant rise in intracellular free Ca^{2+} is postulated to activate Ca^{2+}-activated Cl^- channels (CaCC). Due to the inside-out directed gradient of Cl^- these channels mediate Cl^- efflux thereby further adding to the depolarization of the ciliary membrane. The olfactory CaCC is thought to massively amplify the initial CNG-mediated current.

1.3.1.3. Ca^{2+}-activated Cl^- currents in olfaction

The concept that, in vertebrates, Ca^{2+}-activated Cl^- currents constitute a major part of the odor-induced membrane current and are crucial for amplification of the initial receptor response has been broadly accepted in the scientific literature (reviewed in Kleene, 2008; Pifferi et al., 2009c; Demaria and Ngai, 2010). A ciliary Cl^- conductance that activates with increasing cytoplasmic Ca^{2+} concentrations was first described in 1991 by Kleene and Gesteland in isolated frog OSNs. This Ca^{2+}-activated Cl^- current was then found to be part of the odorant-induced current in amphibian (Kurahashi and Yau, 1993; Kleene, 1993) and mammalian (Lowe and Gold, 1993) OSNs. It soon emerged that intracellular Cl^- is unusually high in OSNs and opening of olfactory CaCC would mediate inward currents and be excitatory under physiological conditions (Kurahashi and Yau, 1993; Zhainazarov and Ache, 1995). Thus, generation of the receptor response of OSNs is thought to involve the sequential activation of two currents: a primary cationic inward current through CNG channels, which is activated by cAMP and is mainly carried by Na^+ and Ca^{2+}, and a secondary Cl^- inward current through CaCCs that is triggered by the influx of Ca^{2+}. Estimates on the current fraction contributed by CaCC range from 50-65% (Kurahashi and Yau, 1993; Zhainazarov and Ache, 1995) up to 90% (Kleene, 1993) in amphibians, 85% in rat (Lowe and Gold, 1993), and 80% (Reisert et al., 2005) to 90% (Boccaccio and Menini, 2007) in mice, where Cl^- currents might even be 30 times higher than CNG currents (Reisert et al., 2003), depending on the electrophysiological settings and the Ca^{2+} buffering conditions. CaCCs have also been reported in fish (Sato and Suzuki, 2000).

The initial discovery of olfactory CaCCs in amphibians has suggested that CaCCs are important to confer resistance to variations in the extracellular ionic environment (Kurahashi and Yau, 1993; Kleene and Pun, 1996) that these freshwater animals encounter. In freshwater the concentration gradients for monovalent cations across the ciliary membrane do not suffice depolarization during odor transduction and instead would rather favor hyperpolarization. However, even low extracellular Ca^{2+} concentrations would provide enough driving force to allow for Ca^{2+} influx through CNG channels. This would trigger CaCC-mediated depolarization by Cl^- and would thus render the odorant response independent of most extracellular cations. Accordingly, studies show that removal of most mucosal cations does not diminish the amplitude of the OSN response (Kleene and Pun, 1996). However, the discovery that the olfactory Ca^{2+}-activated Cl^- current is also present in mammals (Lowe and Gold, 1993) and that also here it makes up for the major fraction of the receptor current has led to a different hypothesis: CaCCs might mediate strong amplification of the initial odor-induced currents carried by CNG channels (Kleene, 1993; Lowe and Gold, 1993). The CaCC current amplifies this primary current, but introduces little additional noise thereby providing a high-gain, low-noise amplification system (Kleene, 1997). Furthermore, the relatively low Ca^{2+} sensitivity of the Cl^- channels with half-maximal activation at 2–5 µM free Ca^{2+} (see below) may introduce an additional excitation threshold. Large receptor currents would only be elicited when the Ca^{2+} concentration reaches a certain threshold level that triggers CaCC activity. This would improve noise suppression in OSNs.

The biophysical properties of the olfactory CaCC have been well established (reviewed in Kleene, 2008; Pifferi et al., 2009c). The dose-response relation for Ca^{2+} has revealed half-maximal activation of 2.2–4.7 µM in rodents (Reisert et al., 2003; Pifferi et al., 2006, 2009b) and 5 µM in frog (Kleene and Gesteland, 1991a) at negative holding potentials. The Hill coefficient is between 2 to 3 suggesting at least two Ca^{2+} binding sites in the CaCC (Kleene and Gesteland, 1991b; Reisert et al., 2003, 2005; Pifferi et al., 2009b). The single-channel conductance has been estimated by noise analysis of macroscopic currents to be very small, ranging from 0.5–1.7 pS [1.6 (Pifferi et al., 2009b), 0.5 pS (Reisert et al., 2003) 1.7 pS (Larsson et al., 1997)] with a maximum open probability of the channel of 0.97. These properties fit well the proposed low-noise high-gain concept of signal amplification.

Some pharmacological blockers have been shown to block the olfactory CaCC efficiently with the most commonly used and best described one being NFA (Kleene, 1993; Reisert et al., 2005; Pifferi et al., 2006; Sagheddu et al., 2010). Also DCDPC (Kleene and Gesteland, 1991a), flufenamic acid (Kleene, 1993), SITS, (Pifferi et al., 2006), NPPB and DIDS (Sagheddu et al., 2010) have been shown to inhibit the olfactory CaCC, however specific blockers with high binding affinity are not available (reviewed in Frings et al., 2000). A continuous run-down of the current in excised patch measurements has been observed by several groups (Kleene and Gesteland, 1991a; Reisert et al., 2003, 2005; Pifferi et al., 2006, 2009b) and might indicate the presence of intracellular modulators important for proper functioning of olfactory CaCCs. Yet, a direct regulation by CaM and dNTPs or negative feedback by prolonged exposure to Ca^{2+} has been excluded (Kleene and Gesteland, 1991a; Reisert et al., 2003).

1.3.1.4. Ion gradients and Cl^- homeostasis in OSNs

Ion fluxes through the olfactory transduction channels — CNG channel and CaCC — and their contribution to the receptor response are determined by the electrochemical driving force for each ion across the ciliary membrane and can be estimated from the resting membrane potential and the concentration gradient across the ciliary membrane. The resting membrane potential of an OSN is between −80 and −60 mV (see discussion in Lagostena and Menini, 2003). However, ion concentrations in the olfactory system are not well established since the cilia’s morphology and small fluid volume and the viscosity of the mucus impede the application of many methods for ion measurements. The different ionic environments an OSN contacts (mucus and interstitial fluid) cannot be preserved during isolation procedures and estimates of physiological ion concentrations are most reliably inferred from intact tissue. Only few and, in part, divergent data on ion concentrations in the olfactory system are available so far. Values for the physiologically relevant ions Ca^{2+}, Na^{+}, K^{+} and Cl^{-}, obtained with different methods and in different species as indicated, are summarized in Table 2.

Measurements of intracellular Cl^{-} concentrations ($[Cl^{-}]_i$) have established unusually high $[Cl^{-}]_i$ in OSNs (Table 2). Using energy-disperse X-ray (EDX) microanalysis in ultrathin cryosections of the intact MOE from rat, Reuter et al. (1998) found total $[Cl^{-}]_i$ of 69 mM in dendritic knobs. Kaneko et al. (2004) investigated $[Cl^{-}]_i$ in intact tissue with the Cl^{-}-sensitive dye MQAE and measured $[Cl^{-}]_i$ of 54 ± 4 mM in rat and 37 ± 6 mM in mice when extracellular Cl^{-} was set to 50 mM. This value is close to 55 mM Cl^{-} in mucus ($[Cl^{-}]_o$) measured by EDX analysis (Reuter et al., 1998). Taking the values obtained from rat the calculated Cl^{-} equilibrium potential across the ciliary membrane is 0 mV ($[Cl^{-}]_i$ = 54 mM, $[Cl^{-}]_o$ = 55 mM) and +5 mV ($[Cl^{-}]_i$ = 69mM, $[Cl^{-}]_o$ = 55 mM), when using the values from MQAE or EDX analysis respectively (see Table 2). Thus, the driving force for efflux of Cl^{-} is high and opening of CaCCs in OSNs results in depolarization.

Keeping this high intracellular $[Cl^{-}]$ requires accumulation against an electrochemical gradient, a process thought to be mediated by the $Na^{+}K^{+}2Cl^{-}$ co-transporter Nkcc1. Expression of Nkcc1 in OSNs has been reported by several groups, yet its subcellular localization is unclear. In knock-out–controlled immunohistochemistry, Reisert et al. (2005) found Nkcc1 protein at the soma and dendrites of OSNs akin to its basolateral localization in secretory cells in which Nkcc1 has a crucial role in Cl^{-} accumulation. Also, Nkcc1 was efficiently blocked in frog OSNs when a pharmacological inhibitor was applied specifically to the soma again supporting basolateral localization of the transporter (Jaén et al., 2011). In contrast, Kaneko et al. (2004) postulated expression in cilia and the dendritic knob since two-photon imaging experiments indicated Cl^{-} replenishment from the apical membrane. This ciliary localization was also reported in recent immunolabeling studies where Nkcc1 was found to co-localize with different Nkcc1-modulating kinases, the $Cl^{-}HCO_3^{-}$ exchanger AE1, ACIII, and Ano2 to the ciliary layer of the MOE (Hengl et al., 2010). A functional role of Nkcc1 in Cl^{-} accumulation has been deduced from pharmacological block or genetic removal of Nkcc1. Both interventions virtually abolished odor-induced Cl^{-} currents in isolated mouse OSNs (Reisert et al., 2005). However, when looking at OSN function *in situ* with EOG measurements, the potential evoked by odorant application was reduced by only ~30–50% when $Nkcc1^{-/-}$ was deleted or pharmacologically blocked (Nickell et al., 2006, 2007).

Table 2 | Ion gradients across the ciliary membrane of OSNs.

	Olfactory mucus	Intra-cellular	$[Cl^-]_o$	Species	Method	Reference
$[Cl^-]$	**55 ± 11***	69 ± 19*	x	Rat	EDX analysis on DK of intact epithelium	Reuter et al., 1998
	93 ± 9	x	x	Toad	Ion-selective microelectrode	Chiu et al., 1988
	x	**54 ± 4**	50	Rat	2P-FLIM of MQAE on DK of intact epithelium	Kaneko et al., 2004
	x	62 ± 6	150	Rat	2P-FLIM of MQAE on DK of intact epithelium	Kaneko et al., 2004
	x	37 ± 6	50	Mouse	2P-FLIM of MQAE on DK of intact epithelium	Kaneko et al., 2004
	x	30 ± 8	150	Rat	MQAE imaging on DK of isolated neurons	Kaneko et al., 2004
	x	~40	100	Newt	MQAE imaging on DK of isolated neurons	Nakamura et al., 1997
	x	119	100	Frog	Perforated-patch on soma of isolated OSNs	Zhainazarov and Ache, 1995
	x	23.3 ± 2.5	140	Mud puppy	Cell-attached patch on DK of isolated OSNs	Dubin and Dionne, 1994
$[Na^+]$	**55 ± 10***	**53 ± 31***	x	Rat	EDX analysis on DK of intact epithelium	Reuter et al., 1998
	85 ± 16	x	x	Toad	Ion-selective microelectrode	Chiu et al., 1988
	52.7 ± 4.1*	x	x	Frog	Atomic-absorption spectroscopy	Joshi et al., 1987
	105*	x	x	Frog	Atomic-absorption spectroscopy	Bronshtein and Leont'ev, 1972
	76*	x	x	Guinea pig	Atomic-absorption spectroscopy	Bronshtein and Leont'ev, 1972
$[K^+]$	**69 ± 10***	**172 ± 23***	x	Rat	EDX analysis on DK of intact epithelium	Reuter et al., 1998
	11 ± 5	x	x	Toad	Ion-selective microelectrode	Chiu et al., 1988
	10.6 ± 1.9*	x	x	Frog	Atomic-absorption spectroscopy	Joshi et al., 1987
	70*	x	x	Frog	Atomic-absorption spectroscopy	Bronshtein and Leont'ev, 1972
	77*	x	x	Guinea pig	Atomic-absorption spectroscopy	Bronshtein and Leont'ev, 1972
$[Ca^{2+}]$	**2.76–7.1**	x	x	Rat	Ion-selective microelectrode	Crumling and Gold, 1998
	x	**68 ± 6 nM#**	x	Mouse	Fura-2 Ca^{2+} imaging on soma of isolated OSNs	Bozza and Kauer, 1998
	x	40 ± 9 nM#	x	Sala-mander	Fluo-3 Ca^{2+} imaging of cilia of isolated OSNs	Leinders-Zufall et al., 1997
	x	57 nM#	x	Sala-mander	Fluo-3 Ca^{2+} imaging on DK of isolated OSNs	Leinders-Zufall et al., 1997
	0.32 ± 0.16	x	x	Toad	Ion-selective microelectrodes	Chiu et al., 1988
	5.3 ± 0.9*	x	x	Frog	Atomic-absorption spectroscopy	Joshi et al., 1987

Concentrations are given in mM if not otherwise stated. Since direct measurements of ion concentrations in cilia are not possible with most methods, the ionic content at the dendritic knob is taken as an approximation since it is expected to equilibrate with the ciliary ion content in the resting state. Values assumed to match best the physiological conditions are marked in bold.
2P-FLIM, two-photon fluorescence lifetime imaging; EDX analysis, energy-disperse X-ray microanalysis, DK, dendritic knob; * mean element concentrations; # free Ca; $[Cl^-]_o$, chloride concentration of extracellular solution

In behaving animals no effect could be observed and *Nkcc1*$^{-/-}$ mice show normal olfactory sensitivity in olfactometric tests (Smith et al., 2008). The lack of strong effects on the EOG and at the behavioral level has been attributed to the presence of multiple Cl^- transporter systems in the mouse olfactory epithelium that partly compensate for Nkcc1 (Nickell et al., 2007). At present, the mechanisms regulating Cl^- homeostasis in OSNs and its cilia are still unclear.

1.3.1.5. Signal termination and adaptation in olfactory signaling

Olfactory signal termination and adaptation ensures high olfactory sensitivity and acuity during continuous or repetitive odor stimulation and allows for odor detection in the presence of background odors. Studies on the underlying molecular mechanisms at the level of signal transduction in the cilia have revealed a major role of Ca^{2+}. Ca^{2+} entering through CNG channels acts on different elements of the odor transduction cascade. First, the CNG channels themselves are subject to feed-back inhibition by CaM (reviewed in Bradley et al., 2005), a mechanism that primarily functions to terminate OSN responses (Song et al., 2008). Second, Ca^{2+} leads to activation of CaM-dependent protein kinase II (CaMKII), which is thought to shape activation kinetics since its inhibition results in changes of the latter. Yet, the underlying molecular mechanism is unknown and ACIII has recently been excluded as a main target of CaMKII (Leinders-Zufall et al., 1999; Reisert and Zhao, 2011). Third, Ca^{2+} extrusion mechanisms play a crucial role in signal termination and adaptation. The activity of sodium-dependent Ca^{2+} exchangers (NCX) (Reisert and Matthews, 1998; Pyrski et al., 2007), ATP-dependent Ca^{2+} pumps (Kleene, 2009; Antolin et al., 2010), and the potassium-dependent Na^{+}/Ca^{2+} exchanger NCKX4 (Reisert and Zhao, 2011) have been implicated in the process.

The olfactory response is also shaped by cAMP removal by phosphodiesterases (PDE). PDE1C and PDE4A have been detected in OSNs and when both enzymes are lacking response termination is slowed (Cygnar and Zhao, 2009). Other factors involved in adaptation might act upstream of ACIII such as desensitization of ORs by phosphorylation (Dawson et al., 1993; Peppel et al., 1997) and β-arrestin binding (Dawson et al., 1993), yet the physiological significance of these processes is thought to be minor. Activation of G-olf by guanine nucleotide exchange factors (Von Dannecker et al., 2005) could also be involved in response regulation. The olfactory marker protein (OMP) is involved in shaping the response time course (Buiakova et al., 1996), but the underlying molecular mechanism is unknown.

1.3.2. The accessory olfactory system

The VNO is a subdivision of the olfactory system that has a key role in mediating the social and defensive responses to species- and sex-specific chemosignals. It is present in most amphibians, reptiles and non-primate mammals, but is absent or vestigial in birds, monkeys and humans. Its major function in guiding social, defensive and innate behaviors has been shown in early experiments with rodents, in which aggression, mating, urine marking and ultrasonic vocalizations were massively reduced after surgical removal of the VNO (Wysocki and Lepri, 1991). Since then, the major chemosensory pathways in the VNO have been identified (reviewed in Tirindelli et al., 2009): VSNs express chemosensory receptors of the V1R and V2R family of GPCRs and couple to signaling pathways distinct from the MOE that involve activation of transient receptor potential canonical 2 (TRPC2) cation channel and phospholipase C (PLC). The VSNs project to the accessory olfactory bulb, which is situated caudal to the main olfactory bulb and innervates the limbic system (see Figure 3).

1.3.2.1. Anatomical organization and morphology of the VNO

The VNO is a paired, tubular structure situated in the basal part of the rostral nasal septum. It is enclosed in a cartilaginous capsule and opens through a duct into the base of the nasal cavity. The medial sides of the two crescent-shaped tubes of the VNO are covered with the vomeronasal sensory epithelium which is bathed with fluid secreted from the vomeronasal glands. To promote stimulus access to this fluid, the VNO is endued with a vascular pumping mechanism. Similar to the MOE, the vomeronasal epithelium is a pseudostratified epithelium composed of apically located supporting cells, several rows of VSNs and basal cells (Figure 6a). It can be subdivided into two non-overlapping zones that are molecularly and functionally distinct (Figure 6a,b). Whereas VSNs of the apical layer express chemosensory receptors of the V1R family and the inhibitory G_i isoform of G proteins, VSNs in the basal layer express V2R receptors and couple to the inhibitory G protein G_o. This spatial segregation is maintained at the level of the accessory olfactory bulb in which projecting axons from apical VSNs synapse in the anterior part and basal VSNs in the posterior part.

1.3.2.2. Signal transduction in VSNs

The two types of vomeronasal receptors, V1R and V2R, constitute large non-homologous gene families that belong to the GPCRs. They do not show any homology to the ORs and differ structurally from each other in that V2R receptors carry a long extracellular N-terminus. The mouse genome contains 191 functional V1R and 123 functional V2R genes (Zhang et al., 2010) while in humans that lack a VNO only two V1R genes are predicted to be functional (Nozawa et al., 2007).

V1Rs and V2Rs and their different subfamilies are tuned for specific recognition of certain animal groups or chemical structures (Isogai et al., 2011). In mice, sex-specific cues that can be present in urine (Leinders-Zufall et al., 2000, 2004; He et al., 2008), tear and saliva (Kimoto et al., 2005; Haga et al., 2010) can be detected by several vomeronasal receptors from both classes. A larger number of vomeronasal receptors from different clades are tuned for the detection of heterospecific cues (Isogai et al., 2011). The importance of V1Rs in behavioral responses to pheromones has been shown in mice deleted for a cluster of 16 *V1r* genes. These mice lack VSN responses to specific pheromonal cues and show alterations in social behaviors such as maternal aggression and male sexual behavior (Del Punta et al., 2002). The role of the G protein subunit α_o ($G\alpha_o$) as a major signaling molecule for the detection of peptide and protein pheromones in the VNO has been established by a knock-out mouse model (Chamero et al., 2011). Pheromone-induced sensory responses from V2R-positive VSNs deleted for $G\alpha_o$ are strongly reduced as are pheromone-guided behaviors, such as male-male and maternal aggression.

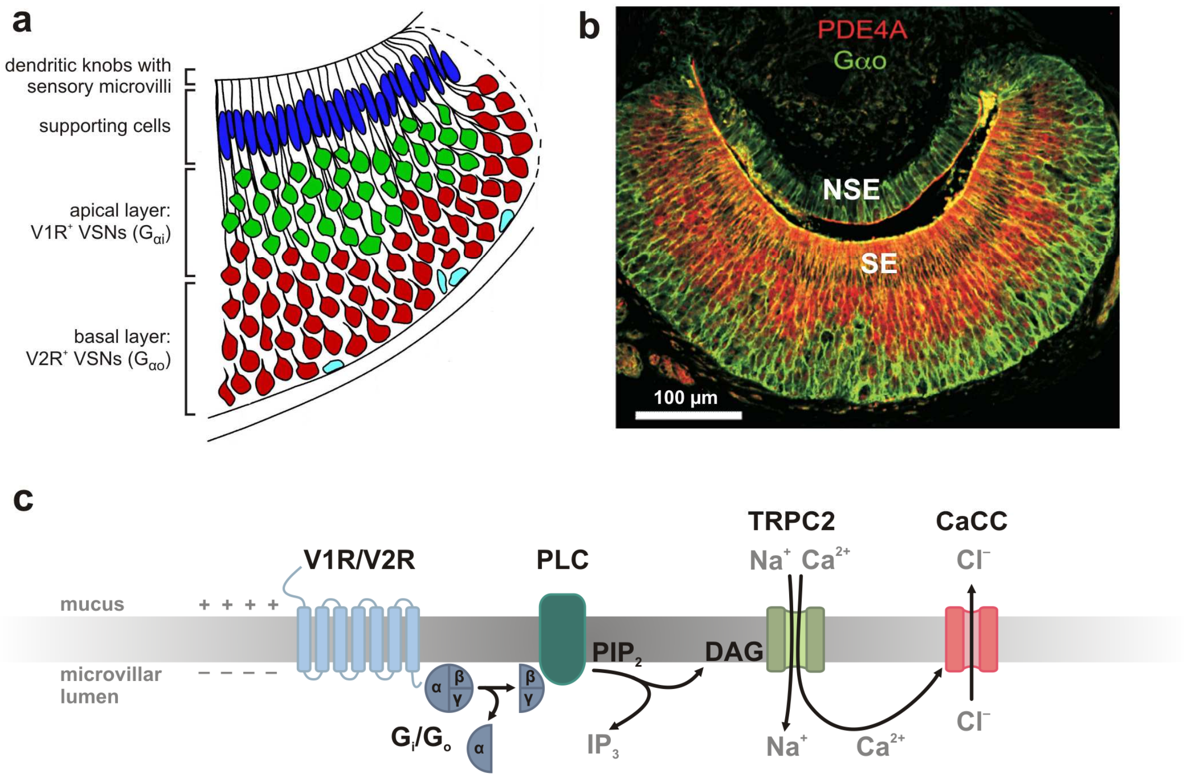

Figure 6 | Structure and signaling mechanisms of the vomeronasal organ.
(a) Schematic representation of the layered structure of the VNO in the mouse. Vomeronasal neurons in the apical layer express V1Rs and $G_{\alpha o}$ unlike neurons from the basal layer that express V2Rs and $G_{\alpha i}$. Vomeronasal sensory neurons bear sensory microvilli at their dendritic endings and their dendrites are embedded in a layer of supporting cells. Modified from de la Rosa-Prieto et al., 2010. **(b)** Immunostaining of a section from the vomeronasal organ reveals the two-layered structure of the sensory epithelium (SE). Phosphodiesterase 4A (PDE4A) is expressed in the basal layer, while $G_{\alpha o}$ expression marks the apical layer. NSE, non-sensory epithelium. Modified from Leinders-Zufall et al., 2004. **(c)** Possible model of the vomeronasal signal transduction pathway. Binding of chemicals to vomeronasal receptors (V1R/V2R) activates G protein (G_o/G_i) that via its β/γ-subunit triggers phospholipase C (PLC) activation and production of inositol trisphosphate (IP_3) and diacylglycerol (DAG) from phosphatidylinositol 4,5-bisphosphate (PIP_2). DAG activates TRPC2 channels and Na^+ and Ca^{2+} flows into the microvillar lumen resulting in depolarization. A Ca^{2+}-activated Cl^- channel (CaCC) might contribute to further depolarization.

There is good evidence that the major ion channel underlying chemoelectrical signal transduction in VSNs is the TRPC2 cation channel that localizes to the sensory microvilli (Liman et al., 1999). It is essential for VSN activation by semiochemicals as well as for the regulation of a variety of social behaviors (Stowers et al., 2002; Leypold et al., 2002; Kimchi et al., 2007; Isogai et al., 2011). A diacylglycerol-gated cation channel in VSN dendrites is strongly impaired in *TRPC2*-deleted mice suggesting PLC-dependent generation of diacylglycerol as a major pathway of vomeronasal receptor-mediated signal transduction in the VNO (Lucas et al., 2003). CaCCs in the VNO have been described only recently and a function in amplifying the olfactory response similar to the postulated role of CaCCs in the MOE has been suggested (Yang and Delay, 2010; Kim et al., 2011). Such a secondary amplification mechanism has been discussed to account for some of the social behaviors preserved in *TRPC2*$^{-/-}$ mice. A model of the vomeronasal signal transduction pathway and its possible components is given in Figure 6c.

1.3.3. Additional olfactory subsystems and non-canonical olfactory signaling

Besides the MOE and the VNO additional olfactory subsystems exist. This includes the septal organ of Masera (SOM), the Grüneberg ganglion (GG) and guanylate cyclase D (GC-D)–expressing neurons. The SOM is an isolated patch of olfactory epithelium located on the base of the nasal septum at the entrances to the nasopalatine ducts (Rodolfo-Masera, 1943; Figure 3). In its morphological and physiological properties it resembles the MOE. Likewise the MOE, OSNs in the SOM express all elements of the canonical olfactory signal transduction cascade, are responsive to odorants and project to the main olfactory bulb (Ma et al., 2003). GC-D–positive OSNs have also been described in the SOM (Ma et al., 2003). By virtue of its location, a role for the SOM in sensing odorants of low volatility that cannot reach the MOE has been postulated. Also, the SOM might serve an alerting function by sensing odors during quiet respiration, when the air stream may not reach the MOE (Giannetti et al., 1995).

The GG was first described by Hans Grüneberg in 1973 (Grüneberg, 1973) as a neuronal structure at the anterior end of the nasal cavity of mice. Its neurons form small grape-like clusters underlying the keratinized epithelium of the nasal vestibule on both sides of the septum. Even though these neurons do not have direct excess to the nasal lumen, the discovery that they express OMP (Fuss et al., 2005), bear cilia (Liu et al., 2009) and project to the necklace glomeruli of the olfactory bulb (Roppolo et al., 2006) suggests a chemosensory function. Accordingly, a function of the GG in the detection of alarm pheromones (Brechbühl et al., 2008) and as cold sensor in neonatal mice (Mamasuew et al., 2008; Schmid et al., 2010) has been described. Also, the GG can be activated by some odorants (Mamasuew et al., 2011). The underlying signal transduction cascades are not known, but the GG expresses elements of a cGMP signal transduction pathway (Fleischer et al., 2009; Liu et al., 2009). The very rostral position of the organ fits a functional specialization in early detection of biologically relevant cues.

Sensory neurons expressing GC-D are considered to represent a distinct olfactory subsystem as their axons project to necklace glomeruli (Fülle et al., 1995; Juilfs et al., 1997; Zufall and Munger, 2010), a morphologically distinct region of olfactory glomeruli situated anterior to the accessory olfactory bulb (Figure 3). GC-D is thought to be activated by natriuretic peptides (Leinders-Zufall et al., 2007) and CO_2 (Hu et al., 2007).

Additional types of receptors for olfactory cues have recently been discovered and the presence of neurons expressing trace amine-associated receptors, formyl peptide receptors and some TRP channels has been established in the olfactory system. Their functional roles are currently being explored. Trace amine-associated receptors respond to volatile amines from urine and thus might be involved in the detection of social cues (Liberles and Buck, 2006; Fleischer et al., 2007). Formyl peptide receptors have been found in the VNO and might respond to molecules related to disease and inflammation (Rivière et al., 2009; Liberles et al., 2009). In addition to being sensitive to odors a subset of OSNs from both the SOM and the MOE may also respond to mechanical pressure and thus sense changes in air pressure during sniffing (Grosmaitre et al., 2007).

1.3.4. Olfactory map formation and odor coding

The first relay station for olfactory information is in glomeruli of the olfactory bulb. Glomeruli are morphological distinct areas of neuropil that compose the glomerular layer at the surface of the olfactory bulb. Here, the axons of OSNs synapse with dendrites of the mitral and tufted cells, the second-order projection neurons of the olfactory system. Olfactory processing and neuronal transmission in the olfactory bulb is shaped by different types of inhibitory interneurons, such as periglomerular cells that synapse within and between glomeruli and granule cells. From the bulb the olfactory information is conveyed by the axons of the mitral and tufted cells to the lateral olfactory tract and the olfactory cortex. Here, odor information is further processed resulting in odor perception and triggering odor-driven behaviors.

Each glomerulus is innervated by many OSNs that all express the same type of OR. This organization is established by two principles. First, according to the concept of the “one neuron–one receptor rule” each OSN expresses in a monoallelic manner only one OR out of the large OR receptor repertoire (reviewed in Serizawa et al., 2004). Second, even though OSNs expressing the same type of OR are scattered, with some zonal expression, over a large area of the MOE, their axons converge on few defined glomeruli, usually two per bulb for each OR (Figure 4a). Since each glomerulus contains only neurons expressing the same type of OR, since each OR typically responds to many odorants and each odorant stimulates — in a concentration-dependent manner — multiple ORs, an odor received in the MOE is converted into a topographic map of multiple differentially activated olfactory glomeruli (reviewed in Mori and Sakano, 2011). Such combinatorial coding together with the dimension and diversity of the receptor repertoire allows for the detection and discrimination of a vast number of odors.

Our knowledge on how the complex axonal wiring pattern that is needed to form this olfactory map is established is still limited (reviewed in Mombaerts, 2006; Zou et al., 2009; Mori and Sakano, 2011). Several factors have been shown to play major roles in axonal convergence of OSNs from their scattered location in the MOE to specific glomeruli in the bulb. This includes OR-derived cAMP signaling, electrical activity and axonal guidance factors. It seems that much of the dorsal-ventral and anterior-posterior positioning, as well as glomerular segregation, occurs autonomously and does not involve target-derived cues. Even though positional information of OSNs in the MOE is preserved in the dorsal-ventral projections this is not the case for positioning along the anterior-posterior axis. Recent work has established a major role of OR-derived cAMP signals in anterior-posterior positioning of glomeruli. During development further refinement of the glomerular map needs to occur through fasciculation and segregation of axon termini in an activity-dependent manner.

The instructive role of ORs or OR-derived activity for axon guidance is apparent from different receptor swap experiments in which changing parts of an OR sequence (Wang et al., 1998), changing its expression level , replacing it with a different OR (Mombaerts et al., 1996; Bozza et al., 2002) or even swapping it for a functionally unrelated GPCR (Feinstein et al., 2004; Feinstein and Mombaerts, 2004) affects the spatial pattern of axonal projections. Likewise, neuronal activity is required for proper development of the glomerular map: Even though knock-out of *Cnga2* (Lin et al., 2000; Zheng et al., 2000) and G-olf (Belluscio et al., 1998) does not or only slightly affect glomerular map formation, activity of ACIII (Zou et al., 2007) and exposure to odorants (Zou et al., 2004) is essential for this process. Since in G-olf null mice G_s activity during neuronal development might compensate for the loss of G-olf (Chesler et al., 2007) it has been concluded that it is the lack of cAMP signaling that causes disturbances of the axonal wiring process. The role of cAMP signaling for proper axonal convergence has been supported by studies that show disorganized glomerular map formation when expression levels or activity of G protein and ACIII are changed (Imai et al., 2006; Chesler et al., 2007). Thus, signaling activity by cAMP is crucial for olfactory map formation. Electrical activity, in contrast, rather is important for OSN survival in a competitive environment as shown for *Cnga2*$^{-/-}$ mice (Zhao and Reed, 2001).

1.3.5. Olfactory disorders in human

Humans vary in their ability to detect odors and the same odor might be perceived in differing qualities. This is mainly due to the widespread genetic variation among the human OR repertoire that has been evolved by single-nucleotide polymorphisms, copy number variations and differential pseudogenization (Hasin-Brumshtein et al., 2009). In the medical conditions of anosmia and dysosmia the sense of smell is completely lost or impaired, respectively. Impairment of smell is common in the general population and the frequency increases with age. Most olfactory dysfunctions are acquired conditions that have developed due to physical damage to the olfactory mucosa or the processing brain areas, mainly by head trauma, upper respiratory tract infections and inhalation of noxious chemicals.

In the infrequent cases of congenital olfactory disorders (~0.05%), anosmia can occur isolated or as part of a syndromic condition. Congenital isolated anosmia (OMIM %107200) is rare and the etiology has not been identified yet (Gásdal Karstensen and Tommerup, 2011). A genetic screening did not find any underlying mutations in the main olfactory signaling proteins and the authors concluded that mutations in these genes are not a major cause for congenital anosmia (Feldmesser et al., 2007). In various pleiotropic diseases, such as Kallmann syndrome, various ciliopathies and congenital insensitivity to pain, anosmia is one manifestation of the clinical spectrum (Gásdal Karstensen and Tommerup, 2011). Also, impaired olfaction is among the first clinical signs of neurodegenerative diseases including Alzheimer's disease and sporadic Parkinson's disease (Doty, 2009). Since olfactory dysfunction frequently goes unreported its prevalence, whether isolated or syndromic, might be underestimated (Nguyen-Khoa et al., 2007).

2. AIM OF THE WORK

Ca^{2+}-activated Cl^{-} currents have been described in a plethora of physiological processes including sensory transduction. In olfaction, Ca^{2+}-activated Cl^{-} channels (CaCCs) are thought to play a crucial role as amplifiers of the initial odor-induced current carried by CNG channels. However, the unknown molecular identity of the underlying channel has precluded direct functional testing. Recently, Ano1 has been cloned as the first *bona fide* CaCC with physiological functions in fluid secretion and smooth muscle contraction. Ano2 is its closest homolog and likewise gives rise to Ca^{2+}-activated Cl^{-} currents. A physiological role of Ano2, though, has not been explored yet. First studies on expression and biophysical properties have established Ano2 as a likely candidate for the molecular identity of the CaCC of olfaction.

In my doctoral thesis I sought to analyze expression and function of Ano2 by generating and characterizing a knock-out mouse model for *Ano2*. In order to reveal which physiological Ca^{2+}-activated Cl^{-} currents are mediated by Ano2 I aimed to investigate the general expression pattern of Ano2 and its subcellular localization in native tissues. This should be done using self-made Ano2 antibodies and *Ano2*$^{-/-}$ tissue as control. Parallel analysis of Ano1 expression should elucidate a possible interplay between these close homologs.

My major goal was to explore if Ano2 constitutes the molecular correlate of the CaCC described in OSNs. In particular, I wanted to address the question if the postulated crucial function of CaCCs in olfactory signal transduction can be confirmed in the physiological context of a mouse model. To this aim, in collaboration with an electrophysiologist in our lab, Ca^{2+}-activated Cl^{-} currents and chemoelectrical signaling in the olfactory system of *Ano2*$^{-/-}$ mice should be electrophysiologically characterized. I also intended to investigate the morphological and biochemical consequences of the lack of Ano2 and how disruption of Ano2 affects olfaction in the behaving animal.

3. RESULTS

3.1. Generation and characterization of Ano2 antibodies

Specific antibodies are crucial for immunohistochemical and biochemical characterization of Ano2. We raised polyclonal antibodies targeted against two different C-terminal peptides and an N-terminal peptide of Ano2 in rabbits and guinea pigs. Three rabbits each were immunized with peptide N3, C2 and C1 (Figure 7). The C1 peptide was additionally used for immunization of three guinea pigs.

```
mAno2  MAAPGLRDIPLLPGSPRRLSSRTVARGSQGPKHGQQYLKVPGHRAPGQRDNSSLHPSQVSRRESSRDRSVINNYL 75
hANO2  --MP--EDIPLLPGSPRRLSPQAGSRGGQGPKHGQQCLKMPGPRAPGLQGGSNRDPGQPCGGESTRSSSVINNYL 71
          *  .*************.:: :**.******** **:** **** :..*. .*.* .**:*.**********

                                                                   peptide N3
mAno2  DANEPPSSEARLSRMHFHDNQRKVDYVLAYHYRKRGAHLGHGSPGHSLAVISNGETGKERHGGGPGDVELGPLDA 150
hANO2  DANEPVSLEARLSRMHFHDSQRKVDYVLAYHYRKRGVHLAQGFPGHSLAIVSNGETGKEPHAGGPGDIELGPLDA 146
       ***** * ***********.****************.**.:* ******::******** *.*****:*******

mAno2  LEEERREQRDEFEHNLMAAGLELEKDLESKSQGSVFVRIHAPWQVLAREAEFLKIKVPTKKMYEIKAGGSIAKKF 225
hANO2  LEEERKEQREEFEHNLMEAGLELEKDLENKSQGSIFVRIHAPWQVLAREAEFLKIKVPTKKMYEIKAGGSIAKKF 221
       *****:***:******* **********.*****:****************************************

mAno2  SAILQTLSSPLQPRVPEHSNNRMKNLSYPFSREKMYLYNIQEKDTFFDNATRSRIVHEILKRTACSRANNTMGIN 300
hANO2  SAALQKLSSHLQPRVPEHSNNKMKNLSYPFSREKMYLYNIQEKDTFFDNATRSRIVHEILKRTACSRANNTMGIN 356
       ** **.*** ***********:*****************************************************

mAno2  SLIANNIYEAAYPLHDGEYDSPGDDMNDRKLLYQEWARYGVFYKFQPIDLIRKYFGEKIGLYFAWLGLYTSFLIP 375
hANO2  SLIANNIYEAAYPLHDGEYDSPEDDMNDRKLLYQEWARYGVFYKFQPIDLIRKYFGEKIGLYFAWLGLYTSFLIP 371
       ********************** ************************************TM1

mAno2  SSVIGVIVFLYGCATIEEDIPS~~~~~~~  ~~~~~~~YEFSKQYWSVLSARLAFVIIFQNLVMFLSVLVDWMIP 827
hANO2  SSVIGVIVFLYGCATIEEDIPS~~~~~~~  ~~~~~~~YEFSKQYWSILSARLAFVIIFQNLVMFLSVLVDWMIP 823
                                                                        TM8****

                            peptide C2           peptide C1
mAno2  DIPTDISDQIKKEKSLLVDFFLKEEHEKVKLADEPTQRSQGGGDRSRRSRAASSAPSGRSQPGSIASSGSQHTNV 1002
hANO2  DIPTDISDQIKKEKSLLVDFFLKEEHEKLKLMDEPALRSPGGGDRSR-SRAASSAPSGQSQLGSMMSSGSQHTNV 998
       ***************************:** ***: ** ******* **********:** **: *********
```

Figure 7 | Antigens for Ano2 antibody generation.
Alignment (ClustalW 2.0.10) of the cytoplasmic parts of mouse (NP_705817.2) and human Ano2 (NP_065106.2) with the peptide sequences used for antibody generation shown in bold letters and highlighted in grey. The regions predicted to form transmembrane segment 1 (TM1) and 8 (TM8) are underlined. The middle part between TM1 and TM8 has been omitted. Amino acid exchanges between human and mouse Ano2 are indicated below (* conserved; : conservative).

Antibodies affinity-purified from final bleeds were first tested on cells overexpressing murine Ano2. All antibodies detected heterologously expressed murine Ano2 in western blots and immunocytochemistry (data not shown). Subsequent testing in immunoblotting on Ano2 expressing tissues using *Ano2*$^{-/-}$ samples as control confirmed signal specificity (Figure 10, Figure 11). For each epitope the antibody from the animal with comparably highest sensitivity combined with low unspecific signals was chosen for further use in our studies.

An overview of Ano2 antibody properties as far as tested is given in Table 3. Notably, in western blots, antibodies targeted against the C-terminal peptide C1 detect the Ano2 isoform of the MOE less efficiently, when compared to signal in eye tissue, than antibodies raised against peptide C2 or N3 (Table 3, compare Figure 10a). In immunohistochemistry, some of the peptide C1 antibodies did not give any Ano2 signal in the MOE whereas they efficiently recognized Ano2 in the VNO and the retina (see Table 3, compare Figure 9f).

The antibody rbAno2_N3-3 does not recognize the Ano2 protein in the R1 ES cell background (see Figure 9). Antibodies rbAno2_N3-3 and rbAno2_C1-2 were additionally tested for recognition of the human form of ANO2 and for cross-reactivity with human ANO1. In immunoblots with extracts of heterologously expressing cells these antibodies recognized human ANO2 and did not cross-react with human ANO1 (data not shown).

Table 3 | Properties of selected Ano2 antibodies.

Database entry	Antibody name		Eye		MOE		VNO	
			WB	IHC	WB	IHC	WB	IHC
#1005	rbAno2_N3-3	sensitivity	+++*	+++*	+++*	+++*	+++*	+++*
		unspecific binding	prominent unspecific band at ~ 55 kDa	strong unspecific labeling of cornea	low	low	low	unspecific punctate labeling of VSN somata
#977	rbAno2_N3-1	sensitivity	++	++	++	+	++	++
		unspecific binding	some	some	some	some	some	some
#975	rbAno2_C2-2	sensitivity	+++	+++	+++	+++	+++	+++
		unspecific binding	some	some	some	some	some	some
#972	rbAno2_C1-2	sensitivity	+++	+++	++	–	+++	+++
		unspecific binding	low	low	low	x	low	low
#973	rbAno2_C1-4	sensitivity	++	++	+	+	++	++
		unspecific binding	some	low	some	low	x	x
#1032	gpAno2_C1-3	sensitivity	++	++	+	–	++	++
		unspecific binding	some	low	some	x	some	low

+++, high; ++, good; +, moderate; –, no signal; x, not tested; WB, western blot; IHC, immunohistochemistry

* does not detect the Ano2^{lox} allele

3.2. Generation of conditional and constitutive *Ano2* knock-out mice

3.2.1. Targeting of *Ano2*

We generated conditional and constitutive *Ano2* knock-out mice by targeting exon 12 for excision with the Cre-loxP system (Figure 8a). Deletion of exon 12, which codes for part of the first extracellular loop and the second transmembrane segment, results in a frame shift and a premature stop codon. The *Ano2* gene deleted for exon 12 is predicted to be non-functional and to have an open reading frame of 345 amino acids.

We constructed the targeting vector (for the vector map see Figure 27) by PCR cloning from genomic DNA of R1 embryonic stem (ES) cells and introduced a neomycin resistance cassette for positive and a diphtheria toxin A cassette for negative selection. Correctly targeted ES cells were identified by Southern blotting (Figure 8). From the four positive clones that we obtained out of the 300 clones picked, ES cell clone C7 and F2 were chosen for injection of blastocysts. Chimeras generated from both clones produced progeny heterozygous for the targeted *Ano2*$^{\mathrm{Neo}}$ allele (Figure 8a). Breeding to FLPe recombinase-expressing deleter mice (Farley et al., 2000) deleted the neomycin resistance cassette and generated the *Ano2*$^{\mathrm{lox}}$ allele, while breeding to Cre deleter mice (Schwenk et al., 1995) resulted in an *Ano2*$^{-}$ null allele (Figure 8a). Heterozygous mice were mated to obtain homozygous progeny. The genotypes of the first litters were confirmed by Southern blotting (Figure 8b). Routine genotyping for the *Ano2*$^{-}$ and the *Ano2*$^{\mathrm{lox}}$ allele was carried out by PCR using the primer pairs represented by arrows in Figure 8a.

►

Figure 8 | Generation of *Ano2*$^{\mathrm{lox/lox}}$ and *Ano2*$^{-/-}$ mice.

(a) Targeting strategy for conditional and constitutive inactivation of the mouse *Ano2* gene. *Top*, part of the wild-type allele *Ano2*$^{+}$ that encompasses exons 11 through 13 (boxes 11, 12, 13). The ~11 kb genomic region shadowed in grey was used to construct the targeting vector. *Below*, in the targeted *Ano2*$^{\mathrm{Neo}}$ allele exon 12 is flanked by two loxP sites (filled triangles) and a flippase-excisable neomycin selection cassette (*Neo*^{R}) with FRT sites (open triangles). The lengths of the short arm (SA), floxed arm (FA) and long arm (LA) of the targeting vector are indicated above. Crossing with FLPeR deleter mice (Farley et al., 2000) removes the *Neo*^{R} cassette resulting in an *Ano2*$^{\mathrm{lox}}$ allele. Excision of exon 12 by crossing *Ano2*$^{\mathrm{Neo}}$ or *Ano2*$^{\mathrm{lox}}$ mice with Cre deleter mice (Schwenk et al., 1995) results in an *Ano2*$^{-}$ allele. The bottom depicts the expected *Eco*RV fragments for the different alleles when using an external probe (solid black bar) for detection in Southern blotting. Arrows mark position of primers used for genotyping: white, primer 7780; grey, primer 7781; black, primer 8133. **(b)** Southern blot analysis using *Eco*RV-digested DNA from tail biopsies of *Ano2*$^{+/+}$, *Ano2*$^{+/-}$ and *Ano2*$^{-/-}$ mice (left) and *Ano2*$^{+/+}$, *Ano2*$^{\mathrm{lox/lox}}$ and *Ano2*$^{+/-}$ mice (right) confirms successful disruption and modification of *Ano2*. Asterisks mark unspecific bands.

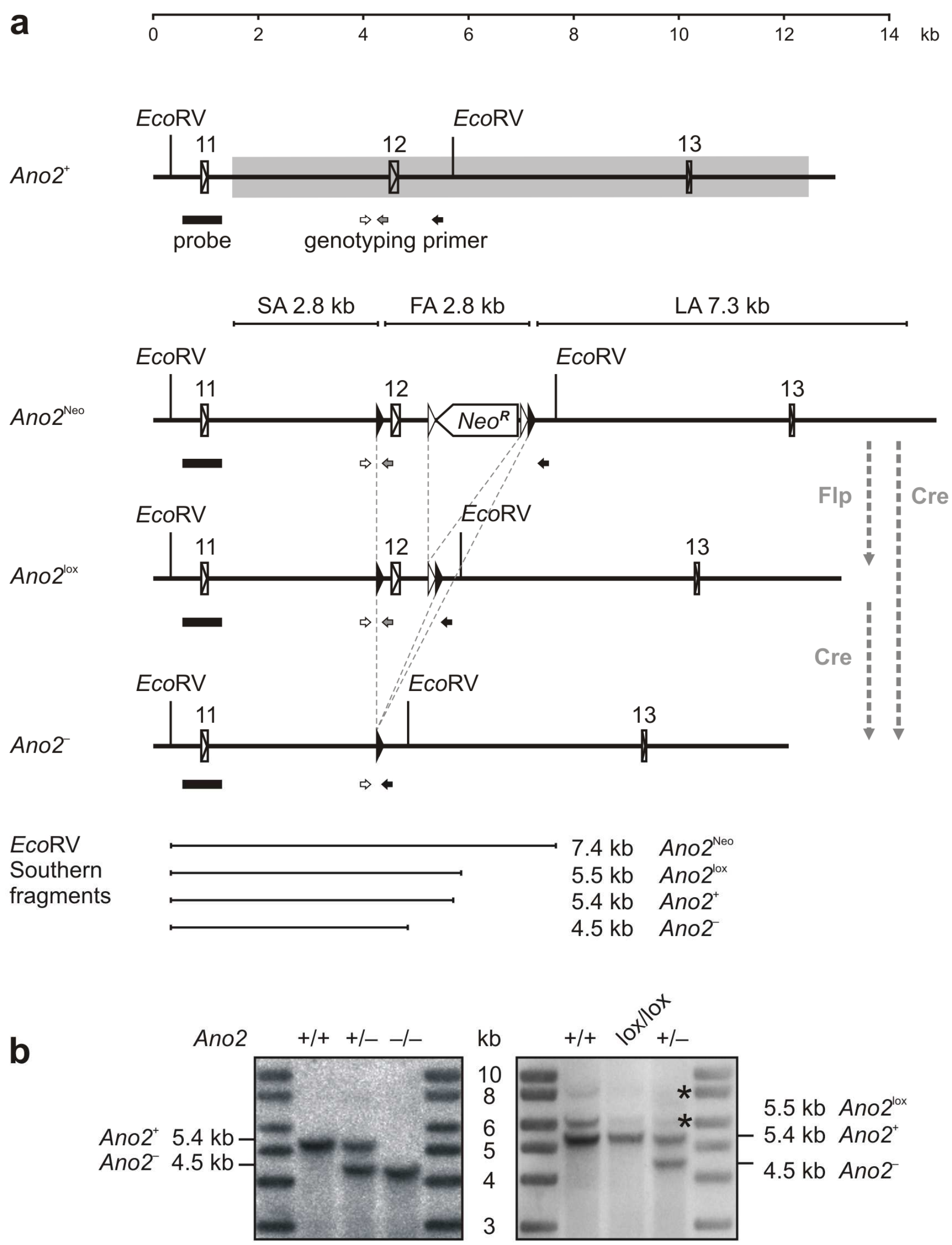

a
0
2
4
6
8
10
12
14
kb
EcoRV
11
12
EcoRV
13
Ano2+
probe
genotyping primer
SA 2.8 kb
FA 2.8 kb
LA 7.3 kb
Ano2Neo
NeoR
Flp
Cre
Ano2lox
Ano2–
EcoRV
Southern
fragments
7.4 kb Ano2Neo
5.5 kb Ano2lox
5.4 kb Ano2+
4.5 kb Ano2–
b
Ano2
+/+
+/–
–/–
kb
10
8
6
5
4
3
Ano2+ 5.4 kb
Ano2– 4.5 kb
lox/lox
*
5.5 kb Ano2lox
5.4 kb Ano2+
4.5 kb Ano2–

3.2.2. Characterization of Ano2 expressed from the *Ano2*^{lox} allele

The floxed *Ano2* mouse is suitable for conditional gene disruption. This requires that expression and function of Ano2 is not affected by the genomic modification that introduced the loxP sites. In western blots we found unchanged banding patterns and normal expression levels of Ano2 protein from *Ano2*$^{lox/lox}$ mice (Figure 9a, left). Likewise, Ano2 protein coded by the floxed *Ano2*^{lox} allele showed normal subcellular localization in the outer plexiform layer (OPL) of the retina (Figure 9d), in sensory microvilli of the vomeronasal epithelium (Figure 9e) and in olfactory cilia of the MOE (Figure 9f).

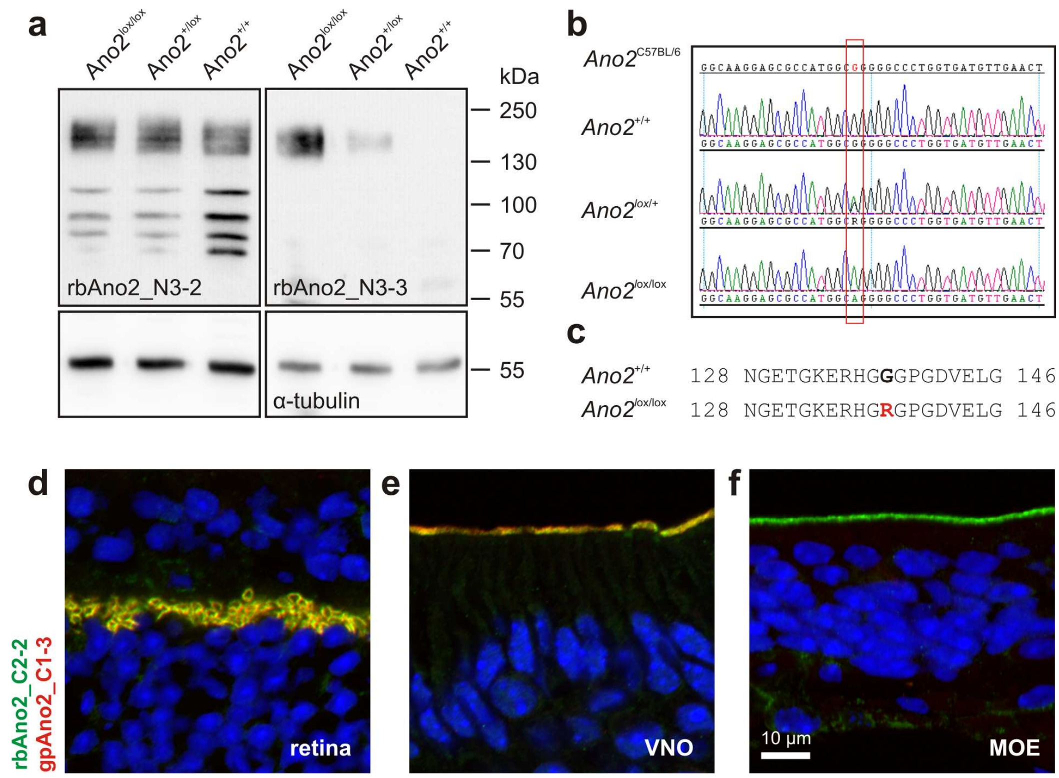

Figure 9 | Characterization of Ano2 expressed from the *Ano2*^{lox} allele.
(a) Immunoblotting with antibody rbAno2_N3-2 (left) shows unchanged expression level and protein size of Ano2 expressed from the *Ano2*^{lox} allele. Antibody rbAno2_N3-3 does not detect the Ano2 isoform expressed from the *Ano2*^{lox} allele (right). **(b)** Sequencing of genomic DNA from *Ano2*$^{lox/lox}$, *Ano2*$^{lox/+}$ and *Ano2*$^{+/+}$ mice reveals a G to A mutation in the floxed allele. The NCBI Reference Sequence for Ano2 from the C57BL/6 background is shown above. **(c)** The nucleotide mutation translates into a G to R amino acid exchange in the peptide N3 target epitope at position 138 of Ano2 (NP_705817.2). **(d–f)** Ano2 protein coded by the floxed *Ano2* allele shows normal subcellular localization in the outer plexiform layer (OPL) of the retina (d), in sensory microvilli of the vomeronasal epithelium (e) and in olfactory cilia of the MOE (f). Labeling was done with antibody rbAno2_C2-2 and gpAno2_C1-3. The antibody gpAno2_C1-3 does not recognize Ano2 in the MOE.

The protein was readily detected by antibodies rbAno2_C2-2, gpAno2_C1-3 and two antibodies recognizing the N-terminal epitope N3 (rbAno2_N3-1, rbAno2-N3-2). Surprisingly, the floxed allele could not be recognized by antibody rbAno2_N3-3, neither in western blotting (Figure 9a, right, and Figure 10) nor in immunohistochemistry. Sequencing of genomic DNA from floxed mice and from the R1 ES cell line, from which these mice were generated, revealed a homozygous single amino acid mutation in the target epitope of rbAno2_N3-3 in the underlying 129X1/SvJx129S1F1 background (Figure 9b). The mutation results in substitution of glycine by arginine (Figure 9c) apparently abolishing the binding to the antibody. We did not test if this mutation affects the CaCC activity of Ano2. The mutated amino acid is conserved among human, rat and mice and no common single nucleotide polymorphisms underlying this mutation were found in database searches.

3.2.3. Constitutive knock-out of *Ano2*

We confirmed successful ablation of Ano2 in *Ano2*$^{-/-}$ mice by western blot analysis using antibodies for different C-terminal epitopes (gpAno2_C1-3, rbAno2_C1-2, rbAno2_C2-2). The ~160-kDa band of Ano2 found in wild-type MOE (Figure 10a,b) and VNO (Figure 10b) was missing from tissue of *Ano2*$^{-/-}$ mice. Likewise, the ~120-kDa band that represents the Ano2 protein in lysates from eye was absent from lysates of *Ano2*$^{-/-}$ eye (Figure 10a,b).

Since the N-terminal rbAno2_N3-3 antibody used for initial characterization was later found not to bind to Ano2 in the R1 ES cell background (compare Figure 9a–c), the lack of signal in *Ano2*$^{-/-}$ tissue does not exclude the presence of a C-terminally truncated protein. However, qRT-PCR consistently revealed a reduction of *Ano2* mRNA to 20% of wild-type level in *Ano2*$^{-/-}$ MOE (see Figure 18e) indicative of non-sense mediated RNA decay of the disrupted *Ano2* mRNA. *Ano2*$^{-/-}$ tissue controls confirm the specificity of the used Ano2 antibodies in western blots and reveal only few unspecific bands (Figure 10a-c). The protein level in heterozygous *Ano2*$^{+/-}$ mice is comparable to the expression level in wild-type mice (Figure 10c).

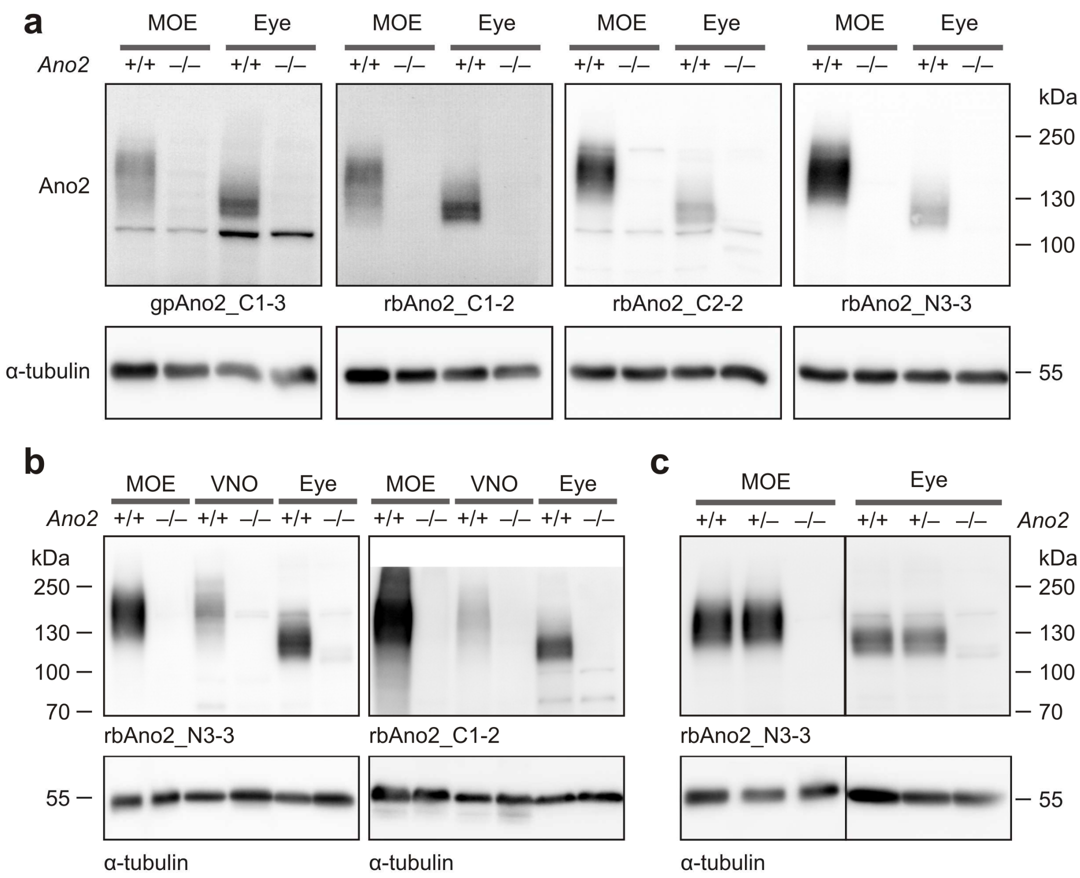

Figure 10 | Lack of Ano2 protein in *Ano2*$^{-/-}$ mice.
Immunoblotting for Ano2 in olfactory tissue and eye with different Ano2 antibodies. **(a)** Immunoblotting for Ano2 in tissue from MOE and eye using antibodies that recognize different epitopes of Ano2. All antibodies show specific Ano2 bands that are lacking from Ano2$^{-/-}$ tissue. Western blots were done in parallel and on the same protein samples allowing for a rough comparison of specificity and sensitivity between the antibodies used. Note the comparably less efficient recognition of the MOE isoform of Ano2 by C1 peptide antibodies (gpAno2_C1-3, rbAno2_C1-2). **(b)** Western blots for Ano2 in the VNO reveal a specific Ano2 band that runs at a similar size as Ano2 from the MOE. **(c)** Western blots for Ano2 in MOE and eye tissue from heterozygous Ano2$^{+/-}$ and wild-type animals indicate comparable expression level of Ano2 in both genotypes. α-tubulin detection serves as loading control and indicates equal protein load of samples from the different genotypes. Protein load: MOE, 16 µg; eye, 100 µg, VNO, 50 µg. The MOE preparation is enriched in α-tubulin since tubulin is a major structural component of cilia.

3.3. Expression pattern of Ano2

Immunoblot analysis using different Ano2 antibodies and knock-out tissue as control revealed a highly restricted expression pattern for Ano2. Ano2 protein expression was found exclusively in neuronal tissues with highest expression in the two sensory systems of smell and vision (Figure 11), consistent with data previously published (Stöhr et al., 2009; Rasche et al., 2010). Ano2 antibodies gave strong signals in western blots from MOE, VNO and eye tissue (Figure 11a, compare Figure 10b). With our antibodies we also found Ano2 in the brain where it was difficult to detect in samples from whole-brain but could be detected in protein lysates from separate parts of the brain (Figure 11a). In the olfactory bulb an Ano2 band with a size corresponding to the olfactory isoform in MOE and VNO was found (Figure 11a, upper arrowhead), while in cortex, midbrain and brain stem we detected an Ano2 band similar to the retinal isoform (Figure 11a, lower arrowhead). Expression levels in these latter tissues were close to the detection limit. No Ano2 expression could be detected in samples from cerebellum and trigeminal nerve (Figure 11a), and spinal cord (data not shown).

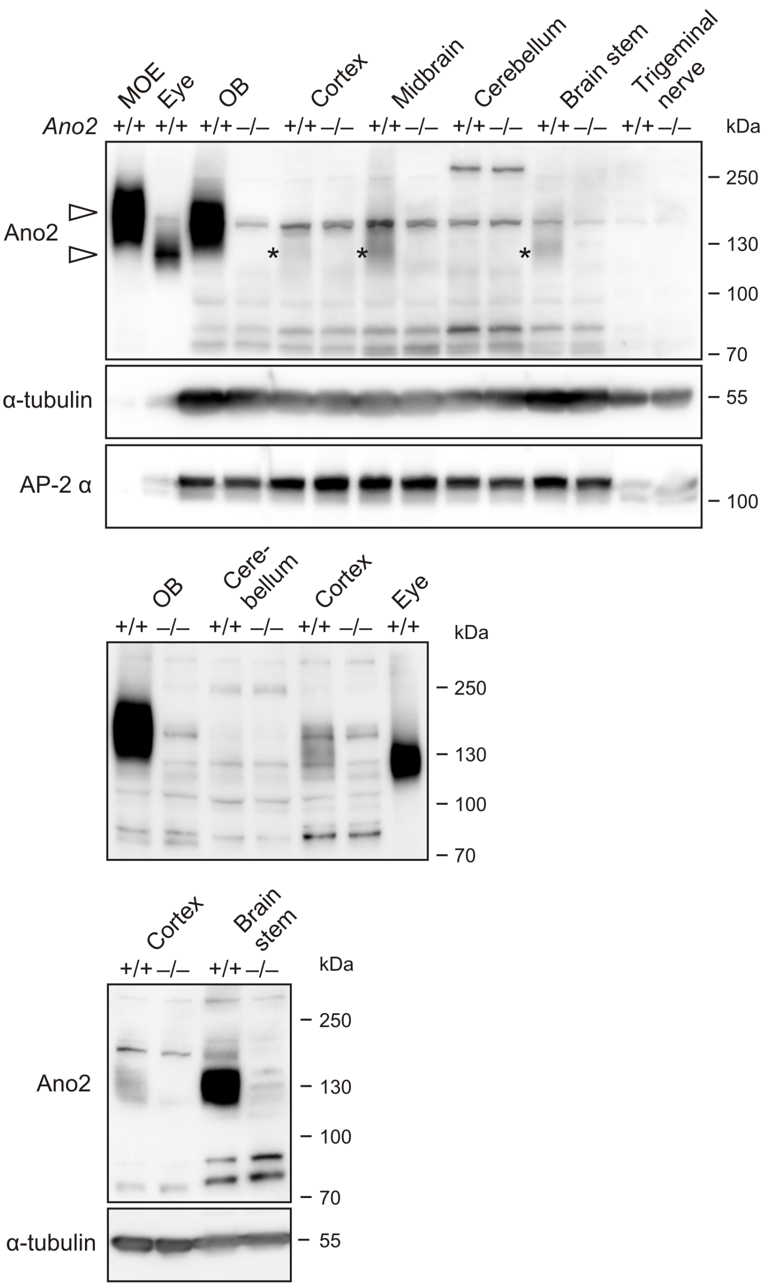

Figure 11 | Immunoblot analysis of Ano2 expression.
Ano2 protein is strongly enriched in the MOE and the eye. It is present in the olfactory bulb, and in lower amounts in the midbrain and brain stem. Expression in the cortex is close to the detection limit (lower panel). No expression is found in cerebellum and trigeminal nerve. Asterisks (*) in the upper panel mark Ano2 in cortex, midbrain and brainstem in which it runs at a similar size as in eye. Protein load: MOE, 1.6 µg; eye, 16 µg; other, 50 µg. α-tubulin and AP-2α detection serves as loading control.

We also tested for Ano2 expression in other sensory systems apart from the nose and the eye. In protein lysates and sections from DRGs we were not able to detect Ano2, even though mRNA expression in axotomized DRG neurons has been reported (Boudes et al., 2009). Immunohistochemistry on the inner ear did not reveal any Ano2 signals. As *in silico* data consistently indicated expression of Ano2 in reproductive organs and sometimes in the digestive system we performed western blot analysis on these tissues but were unable to detect Ano2. Also, all other tissues tested for Ano2 protein expression, namely lung, skin, spleen, kidney, liver, skeletal muscle, salivary gland and heart, were negative.

Additionally, we analyzed Ano2 expression at postnatal day null. Consistent with a fully functional olfactory system at this developmental stage Ano2 expression in the MOE was detected by western blot analysis and immunohistochemistry. In contrast, in the retina that is not fully developed at birth, Ano2 was not detectable in immunoblot analysis or immunohistochemistry (data not shown).

3.4. Ano2 isoforms

The Ano2 protein runs at higher apparent molecular weights in olfactory tissues than in other Ano2-positive tissues. In the olfactory tissues of the MOE, the VNO and the olfactory bulb, Ano2 yields a broad ~160-kDa band, while in eye and in the different brain regions the protein runs at ~120 kDa and gives a more condensed band (Figure 12a, compare Figure 10a,b and Figure 11a). The higher apparent molecular weight of olfactory Ano2 is due to extensive N-linked glycosylation, as indicated by the uniform triplet band of Ano2 at ~110–120 kDa that we detected after deglycosylation of tissue from MOE, VNO and eye with N-glycosidase F (Figure 12). This size fits well with the calculated molecular weight of 114 kDa for the 1002 amino acid full-length form of mouse Ano2. Heterologously expression of a shorter murine Ano2 isoform of 913 amino acids and N-glycosidase F deglycosylation results in a similar triplet pattern at a distinctively lower size of ~100–110 kDa conformant with its calculated size of 104 kDa (Figure 12b). The different bands of the triplet found after deglycosylation could be due to unknown posttranslational modifications.

In western blots, antibodies raised against peptide C1 detect the Ano2 protein in the MOE less efficiently than other Ano2 antibodies when normalized to the signal of the retinal Ano2 (Table 3, compare Figure 10a). This is reflected in immunostainings where the peptide C1 antibody rbAno2_C1-2 does not give any signal in the MOE but detects the vomeronasal and retina protein efficiently (Figure 9d-f). The tissue-specific differences in binding affinity of C1 peptide antibodies might be due to differing posttranslational modifications.

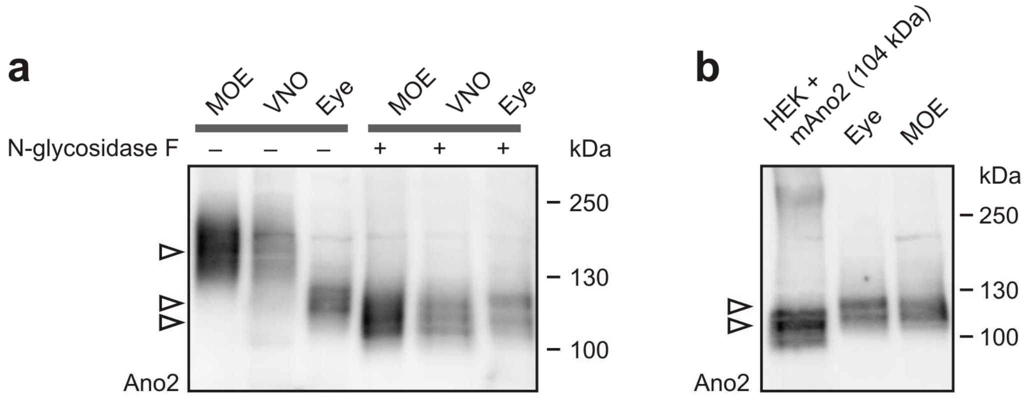

Figure 12 | Glycosylation isoforms of Ano2.
Immunoblots of Ano2 (rbAno2_N3-3) from different tissues after deglycosylation with N-glycosidase F. **(a)** Ano2 protein runs at higher apparent molecular weights in olfactory tissues than in eye but yields a uniform triplet running at ~110 to ~120 kDa after deglycosylation with N-glycosidase F. Different bands of the triplet may represent additional posttranslational modifications. **(b)** Deglycosylated Ano2 protein from the eye and MOE runs at higher apparent molecular weights than a deglycosylated 104 kDa-isoform of mouse Ano2 expressed in HEK cells (HEK + mAno2). The 104 kDa-isoform gives a triplet pattern similar to the native Ano2.

3.5. Functional characterization of Ano2 in the olfactory system

3.5.1. Expression of Ano2 and its homolog Ano1 in the olfactory system

3.5.1.1. Ano2 is highly enriched in sensory cilia of OSNs

The restricted expression pattern of Ano2 with most prominent expression in tissue from the olfactory system (compare Figure 11) points to a functional role of Ano2 in olfaction where it has been suggested to represent the CaCC of olfactory signal transduction (Stephan et al., 2009; Pifferi et al., 2009a; Rasche et al., 2010). We investigated the subcellular localization of Ano2 in the nose by immunohistochemistry and found Ano2 signals restricted to the apical surface of the MOE and the VNO (Figure 13a). In the MOE, Ano2 co-localized with the α-subunit Cnga2 of the olfactory CNG channel that is specifically expressed in sensory cilia and represents a major component of the olfactory signal transduction cascade (Figure 13d). We observed no signal in *Ano2*$^{-/-}$ MOE confirming the specificity of the Ano2 antibody in the MOE (Figure 13d).

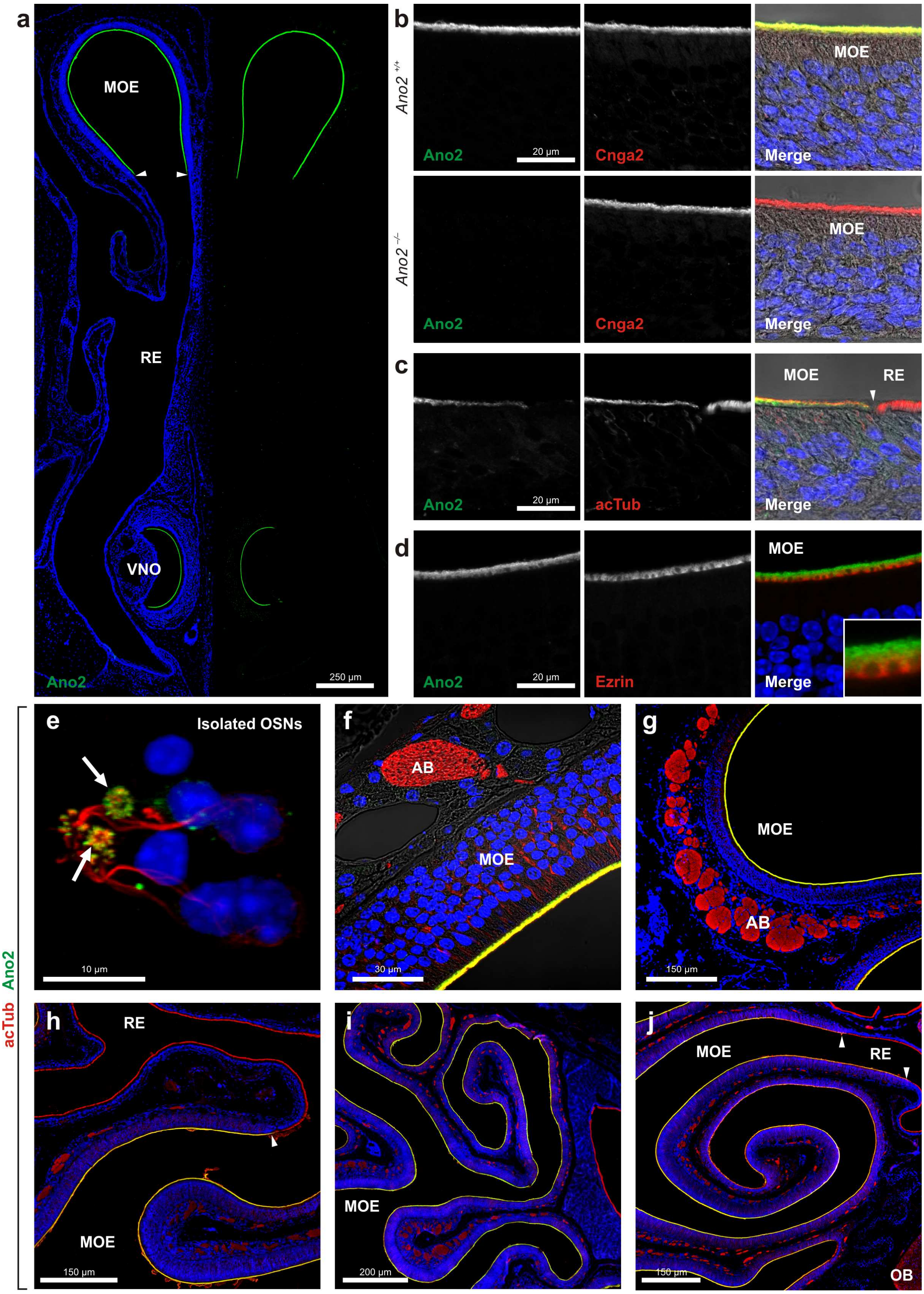

a
MOE
RE
VNO
Ano2
250 µm
b
Ano2 +/+
Ano2 −/−
Ano2
Cnga2
Merge
MOE
20 µm
c
MOE
RE
Ano2
acTub
Merge
20 µm
d
MOE
Ano2
Ezrin
Merge
20 µm
e
Isolated OSNs
10 µm
f
AB
MOE
30 µm
g
MOE
AB
150 µm
h
RE
MOE
150 µm
i
MOE
200 µm
j
MOE
RE
OB
150 µm
Ano2
acTub

Figure 13 | Ano2 localizes to sensory cilia of the main olfactory epithelium.
Confocal microscopy images of histological sections from the nasal cavity labeled for Ano2 and different markers. **(a)** Coronal view of the anterior part of the nasal cavity stained for Ano2. Ano2 localizes to the surface of the MOE and the VNO, but not to the respiratory epithelium (RE). **(b)** Co-localization of Ano2 and Cnga2 in olfactory cilia of the MOE. Ano2 signal is lacking from *Ano2*$^{-/-}$ control tissue. MOE from *Ano2*$^{-/-}$ mice is morphologically indistinguishable from wild-type. **(c)** High resolution image from the transition region from MOE to RE shows Ano2 expression exclusively in OSNs, where it co-localizes with acetylated tubulin (acTub). **(d)** Ano2 does not co-localize with ezrin found in microvilli of supporting cells but is expressed in the layer of intertwined olfactory cilia that covers the microvillar cells. **(e)** Labeling of isolated OSNs with Ano2 and acTub shows Ano2 signals highly enriched in the cilia emanating from the dendritic knobs (arrows). AcTub also stains the dendrites of OSNs. The merged picture is a maximum intensity projection from a stack of confocal images. **(f)** High resolution image of the MOE stained for Ano2 and acetylated tubulin. Ano2 and acTub co-localize in the ciliary layer. acTub also labels the dendrites and axons of OSNs and marks the OSN axon bundles (AB) underlying the MOE. **(g-j)** Merged images of coronal sections from more anterior (g) to more and more posterior (h-j) parts of the MOE labeled for Ano2 and acTub reveal Ano2 expression in all zones of the MOE. In (j) part of the olfactory bulb (OB) is included in the section. All stainings used Ano2 antibody rbAno2_N3-3. In the merged pictures nuclei are represented in blue and in (b,c,f) antibody signals are superimposed on transmission light pictures. Arrowheads mark transition from MOE to RE.

◄

Localization of Ano2 to the olfactory cilia was also confirmed by its co-localization with acetylated tubulin (Figure 13c, e–j). Acetylated tubulin is a stabilized form of tubulin that is highly enriched in cilia and is additionally found in dendrites and axons of neurons. In our stainings the acetylated tubulin antibody labeled the olfactory cilia and the morphologically distinct motile cilia of the neighboring OSN as well as the dendrites and axons of OSNs (Figure 13c, e–j). Co-expression with Ano2 was restricted to olfactory cilia and the Ano2 signal was abruptly lost at the transition from MOE to RE (Figure 13c,h,j). Ano2 was not found in microvilli of the olfactory supporting cells (Figure 13d) that are marked by ezrin (Figure 13d). Expression of Ano2 did not show any zonal variance. Ano2 was detected evenly throughout the MOE, in sections from the anterior part (Figure 13a) to more and more posterior parts (Figure 13g-j). Labeling of isolated OSNs for Ano2 and acetylated tubulin confirmed that expression of Ano2 is highly enriched in cilia (Figure 13e). This restricted localization to sensory cilia of OSNs is consistent with a putative role as CaCC of olfactory signal transduction and conforms to previously published data (Rasche et al., 2010; Hengl et al., 2010; Sagheddu et al., 2010).

3.5.1.2. Ano2 localizes to sensory cilia of the septal organ of Masera

OSNs of the SOM express all components of the canonical olfactory signal transduction cascade and resemble neurons from the MOE. Similar to the MOE, we found Ano2 expression in the sensory epithelium of the SOM (Figure 14a). Ano2 was highly enriched in the ciliary layer, where it co-localized with the cilia marker acetylated tubulin (Figure 14b). The SOM also stained positive for Cnga2 and ACIII (data not shown). In the Grueneberg ganglion we were not able to detect Ano2 in immunohistochemistry (data not shown).

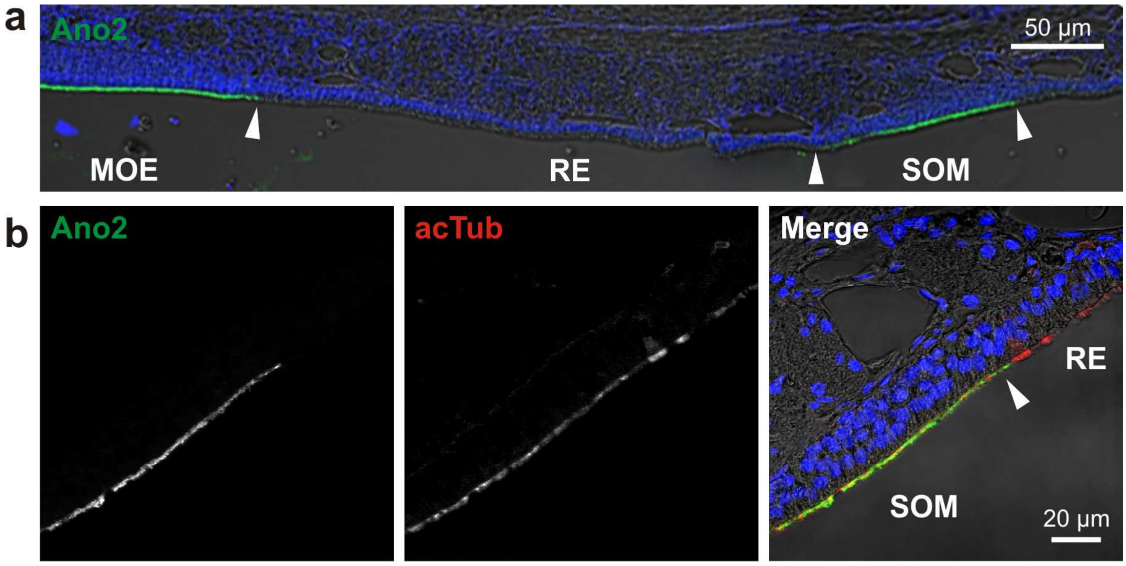

Figure 14 | Ano2 localizes to sensory cilia of the septal organ of Masera.
(a) Coronal section of the nasal septum with the SOM labeled for Ano2. Ano2 is expressed in the apical layer of the SOM. **(b)** Ano2 in the SOM co-localizes with the ciliary marker acetylated tubulin (acTub). Ano2 was detected using antibody rbAno2_N3-3. Arrowheads mark the transition between sensory and respiratory epithelium (RE). In the merged pictures nuclei are represented in blue and antibody signals are superimposed on transmission light pictures.

3.5.1.3. Ano2 and Ano1 co-localize in sensory microvilli of the VNO

In the VNO we found expression of Ano2 restricted to sensory microvilli of VSNs, analogously to its expression in sensory cilia of OSNs (Figure 15). Since microvilli do not express high levels of acetylated tubulin, the cilia marker acetylated tubulin only labeled dendrites and axons of VSNs but not the apical layer of the sensory epithelium (Figure 15a). In contrast to the MOE where we did not find Ano1 expression in sensory epithelium (compare Figure 16a,d), Ano2 co-localized with its closest homolog Ano1 in the sensory epithelium of the VNO (Figure 15c).

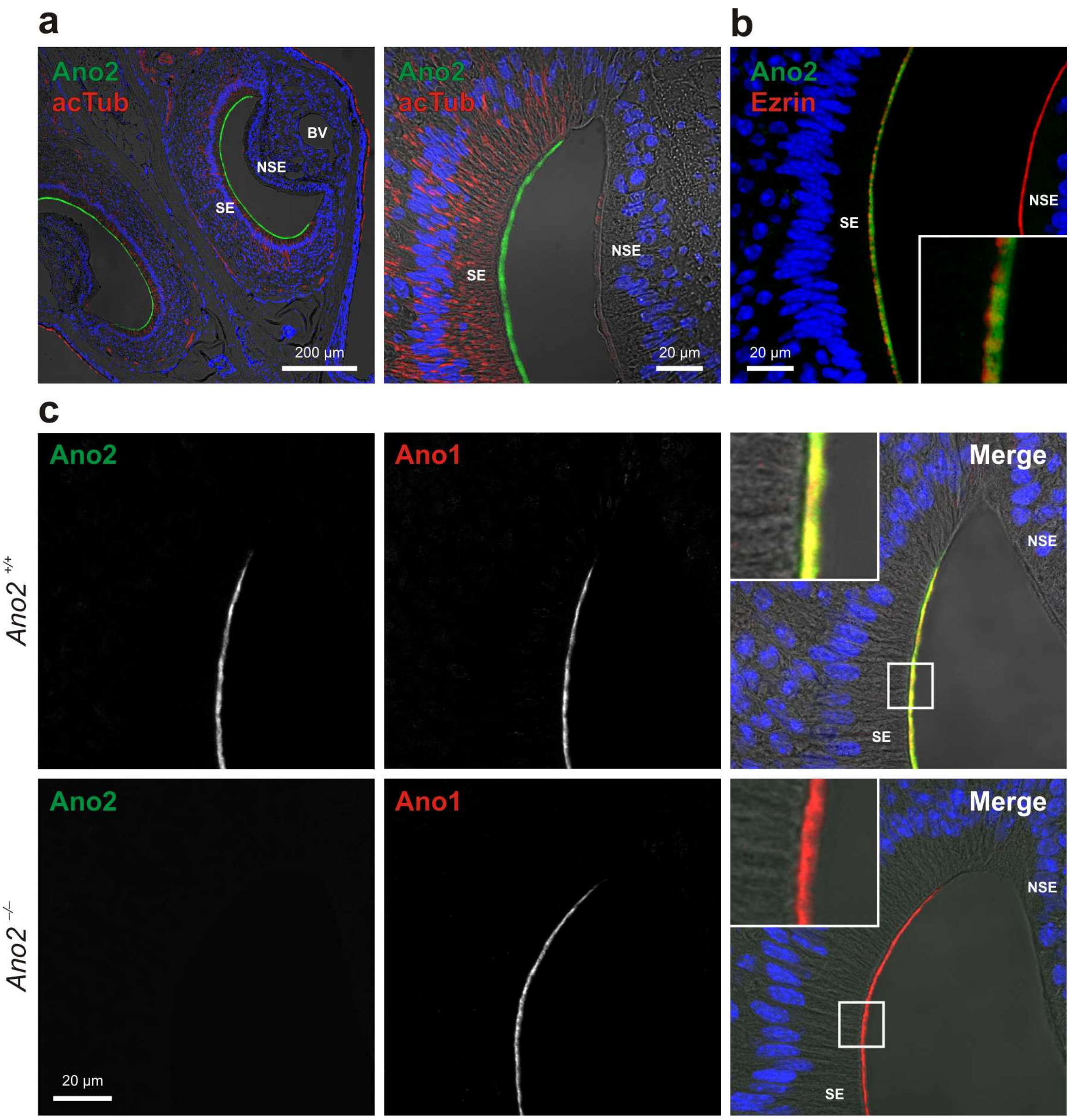

Figure 15 | Ano2 and Ano1 co-localize in sensory microvilli of the VNO.
Confocal microscopy images of histological sections from the VNO co-stained for Ano2 and acetylated tubulin (a), ezrin (b) or Ano1 (c). **(a)** Ano2 (antibody rbAno2_N3-3) is expressed in the apical layer of the vomeronasal sensory epithelium. Acetylated tubulin (acTub) marks VSN dendrites and axons but not the sensory microvilli of VSNs. **(b)** Ano2 (antibody rbAno2_N3-3) does not co-localize with ezrin, a marker for microvilli of supporting cells in the MOE. Ezrin stains the apical layer of the non-sensory epithelium (NSE) and the microvilli of a subset of cells in the sensory epithelium of the VNO (SE) that likely represent supporting cells. **(c)** A section from the VNO co-labeled for Ano2 (antibody gpAno2_C1-3) and Ano1 shows that both proteins are expressed in the sensory protrusions of VSNs. Staining of *Ano2*$^{-/-}$ VNO confirms antibody specificity and reveals normal expression and localization of Ano1 in the absence of Ano2. In the merged pictures nuclei are represented in blue (a–c) and antibody signals are superimposed on transmission light pictures (a,c). SE, sensory epithelium; NSE, non-sensory epithelium; BV, blood vessel.

The sensory layer of the VNO is made of microvilli that stem from two distinct VSN populations expressing different types of vomeronasal receptors and signaling molecules. Since the microscopic resolution of our images does not allow discrimination between single microvilli, we cannot distinguish if Ano1 and Ano2 are co-expressed in the same microvilli or if they reside in microvilli of different VSN populations. Since localization and expression of Ano1 were not affected by the loss of Ano2 in *Ano2*$^{-/-}$ mice (Figure 15c) a direct functional interaction between both proteins may not occur. We also co-stained the VNO for Ano2 and ezrin, a marker known to label microvilli of supporting cells in the MOE. We found no co-localization of both proteins indicating that Ano2, and analogously also Ano1, are not expressed in the ezrin-positive cells of the VNO that probably represent supporting cells (Figure 15b).

3.5.1.4. Ano1 localizes to apical membranes of secretory cells in the nose

Besides Ano2, expression of the closely related Ano1 has been reported in the MOE. Ano1 was detected by RT-PCR (Stephan et al., 2009; Rasche et al., 2010) and in mass spectrometric analysis of olfactory tissue preparations (Mayer et al., 2009; Rasche et al., 2010). We analyzed expression and subcellular localization of Ano1 in the nose by immuno-labeling with an Ano1 antibody. This antibody has previously been reported to give specific signals for Ano1 in the mouse colon (Gomez-Pinilla et al., 2009).

►

Figure 16 | Ano1 localizes to apical membranes of secretory cells in the nose.
Confocal images of histological sections from the nasal cavity labeled for Ano1 and different markers. **(a)** Coronal view of the anterior part of the nasal cavity stained for Ano1 after harsh antigen retrieval (pH9.0, 100℃, 20 min). Ano1 localizes to the apical membrane of a subset of cells from the respiratory epithelium (RE, insets 1–5) and the different nasal glands (1, 3–5). Ano1 is not expressed in the MOE (inset 1), but is found in the sensory epithelium of the VNO. Ano1 antibody also labels smooth muscle cells surrounding the blood vessels (BV) of the VNO (inset 5). Glandular structures are marked by asterisks. **(b)** Ano1 expression is found in apical membranes of glandular tissue cells in the nasal septum and in a subset of cells in the RE. Ano1 only labels non-ciliated cells of the RE that are not stained by acetylated tubulin (acTub). A higher magnification of the RE with neighboring ciliated and non-ciliated cells is shown in the inset. **(c)** Co-labeling for Ano1 and ezrin in nasal glands of the septum. Ano1 and ezrin co-localize in apical membranes of the glandular tissue as highlighted in the inset showing a magnification of an acinar cell duct. **(d)** Ano1 is not expressed in the MOE but in a subset of cells of the RE. Ano1 signal does not co-localize with acTub that marks ciliated structures. **(e)** Labeling of the MOE with Ano1 after harsh treatment for antigen retrieval (pH9.0, 100℃, 30 min) reveals Ano1 expression in Bowman glands and ducts (arrow) that underlie the MOE. These structures are co-labeled by ezrin which also stains the microvillar layer of the supporting cells on the surface of the MOE. **(f)** Expression of Ano1 in vomeronasal glands surrounding the blood vessels (BV) in the VNO and in cells of the RE. In the merged pictures nuclei are represented in blue and in (b–d) antibody signals are superimposed on transmission light pictures. Pictures in (c,e,f) are maximum-intensity projections of confocal images.

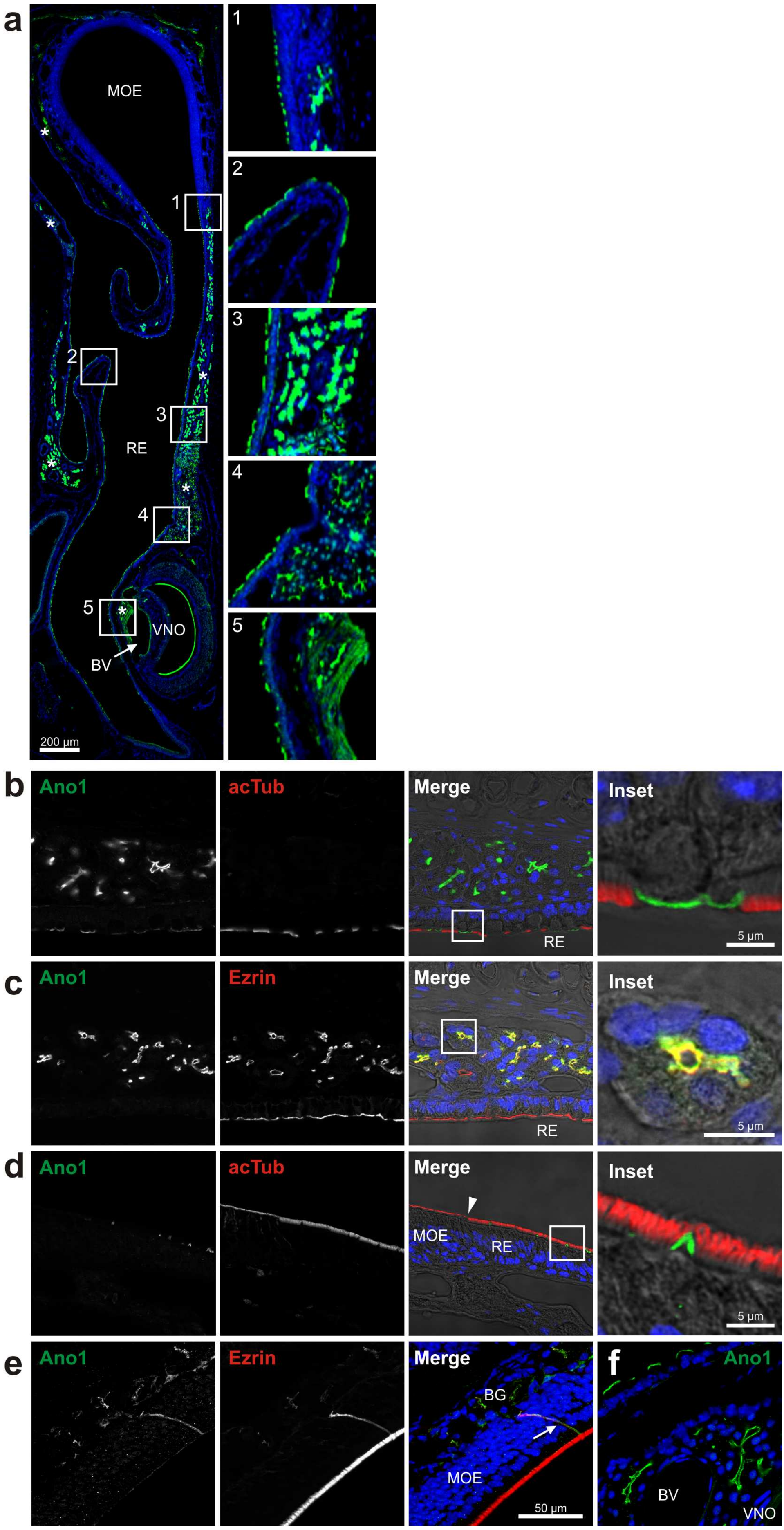
a
MOE
1
2
3
4
5
RE
VNO
BV
200 µm
b
Ano1
acTub
Merge
Inset
RE
5 µm
c
Ano1
Ezrin
Merge
Inset
RE
5 µm
d
Ano1
acTub
Merge
Inset
MOE
RE
5 µm
e
Ano1
Ezrin
Merge
BG
MOE
50 µm
f
Ano1
BV
VNO

We found Ano1 signals restricted to secretory cells of the RE and the underlying glandular tissues (Figure 16). Ano1 antibody labeled non-ciliated cells of the RE that were classified morphologically as mucus-secreting goblet cells (Figure 16a, inset b+d). Ano1 also localized to apical membranes of acinar and duct cells of different types of mucous and serous nasal glands that underlie the RE (Figure 16a,b,c). Likewise, Ano1 expression was found in mucosal glands of the sensory epithelia, such the vomeronasal glands (Figure 16a,f) and the mucus-secreting Bowman glands underlying the olfactory mucosa (Figure 16e). We did not detect Ano1 in sensory neurons of the MOE (Figure 16a,d,e). Expression of Ano1 in apical membranes of secretory cells is consistent with its postulated role in fluid secretion in other epithelia and glands. Using harsh conditions of antigen retrieval we also detected Ano1 signal in smooth muscle cells of the VNO blood vessels (Figure 16a). Expression in smooth muscle cells has been previously reported for Ano1 (Huang et al., 2009).

3.5.1.5. Ano2 in axons and synaptic endings of OSNs in the olfactory bulb

Since we detected Ano2 protein in western blots of the olfactory bulb we investigated its localization by immunohistochemistry. Ano2 protein was present on axons of OSNs that make up the olfactory nerve layer of the bulb and in the olfactory glomeruli they converge to (Figure 17). Ano2 signal was absent from the neighboring periglomerular cells that in our co-stainings were marked by strong expression of tyrosine hydroxylase (Figure 17b, inset). Periglomerular cells represent a main type of inhibitory interneurons in the bulb and shape synaptic transmission in the glomerular layer by synapsing with axons of OSNs and the dendrites of mitral and tufted cells that are the second-order projection neurons of the olfactory system.

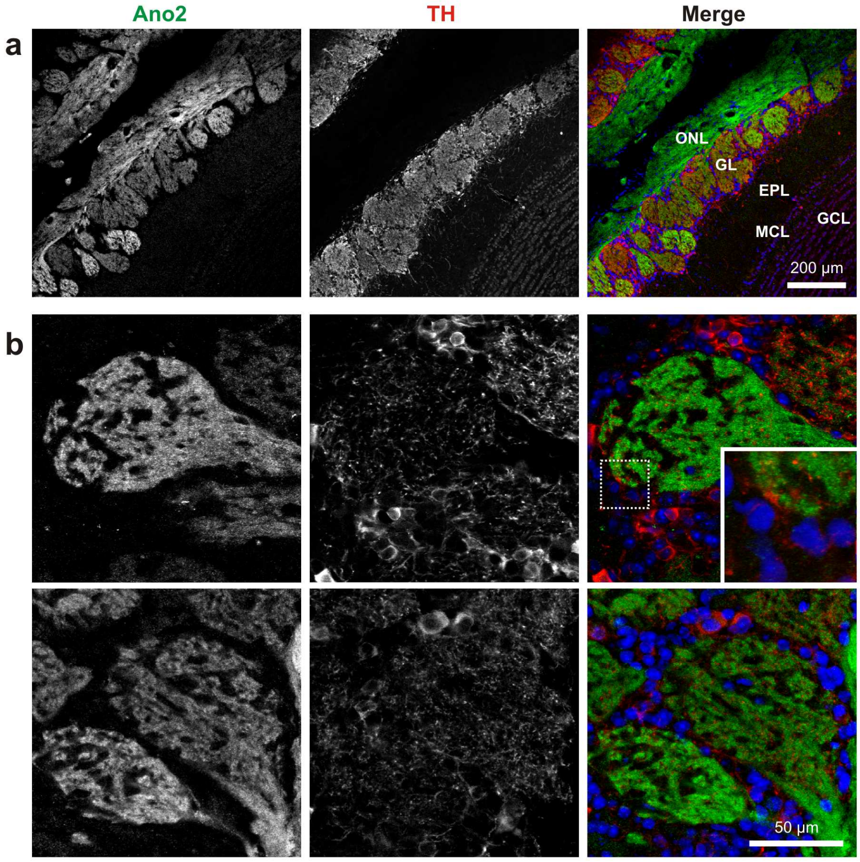

Figure 17 | Ano2 in axons and synaptic endings of OSNs in the olfactory bulb.
Confocal microscopy images of coronal sections from the olfactory bulb stained for Ano2 and tyrosine hydroxylase (TH). **(a)** Ano2 localizes to the axonal endings of OSNs in the olfactory nerve layer (ONL) and the glomeruli of the olfactory bulb where OSNs synapse to second-order M/T cells. TH is expressed in periglomerular cells that represent the inhibitory interneurons of the glomerular layer and synapse extensively with OSNs and M/T cells in and around the glomeruli. GL, glomerular layer; EPL, external plexiform layer; MCL, mitral cell layer; GCL, granule cell layer. **(b)** High resolution picture of Ano2-labeled olfactory glomeruli in the olfactory bulb co-stained with TH. In the merged images nuclei are labeled in blue.

3.5.2. No change of Anoctamins and key olfactory proteins in *Ano2*$^{-/-}$ mice

Immunohistochemistry of olfactory tissues from *Ano2*$^{-/-}$ mice did not reveal any obvious changes in tissue morphology (compare Figure 13b and Figure 15c). This was independent of age. We did not observe any neurodegenerative effects or morphological changes in aged animals (50–70 weeks–old, data not shown). Consistent with the normal morphology of the MOE and the VNO in adult *Ano2*$^{-/-}$ mice, levels of the olfactory marker protein (OMP) were unchanged in western blots of these organs (Figure 18a). OMP is expressed in all mature sensory neurons of the olfactory system and thus should indicate changes in number or condition of OSNs.

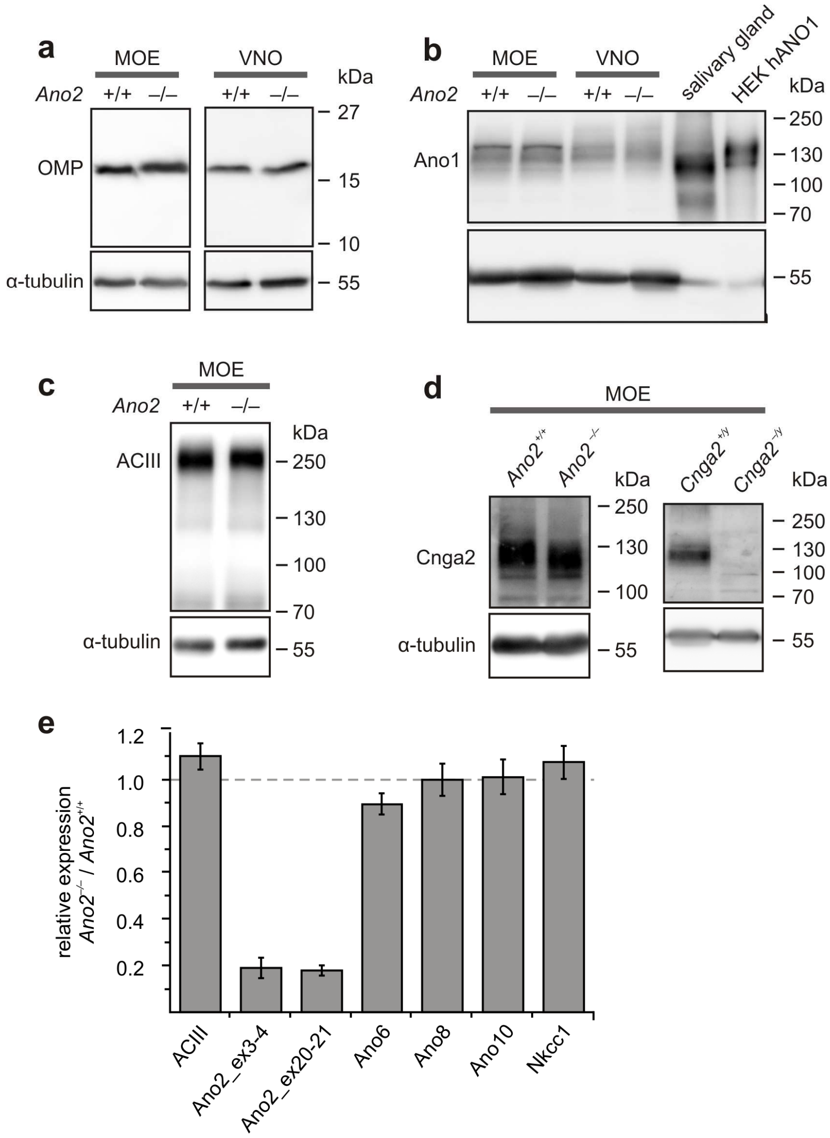

Figure 18 | Anoctamins and key olfactory proteins are unchanged in *Ano2*$^{–/–}$ mice.

(a–d) Immunoblots demonstrating unchanged expression of Ano1 and key olfactory signal transduction elements in *Ano2*$^{–/–}$ mice. **(a)** Levels of olfactory marker protein (OMP), a marker for mature OSNs, in MOE and VNO are unaffected by the loss of Ano2. **(b)** Ano1 immunoblot of extracts from Ano2+/+ and *Ano2*$^{–/–}$ MOE and VNO, using salivary gland and lysates form HEK cells transfected with human ANO1 (HEK hANO1) as positive controls. Ano1 protein levels are unchanged in *Ano2*$^{–/–}$ mice. Protein load: MOE and VNO, 100 µg, salivary gland 32 µg. **(c)** Unchanged levels of adenylate cyclase III (ACIII), a major component of the olfactory signal transduction cascade, in the MOE of *Ano2*$^{–/–}$ mice. **(d)** Unchanged expression levels of the CNG channel subunit Cnga2 in the MOE of *Ano2*$^{–/–}$ mice. Absence of bands in extracts from Cnga2$^{–/y}$ MOE confirms antibody specificity. **(e)** Quantitative real-time PCR on MOE of *Ano2*$^{+/+}$ and *Ano2*$^{–/–}$ mice reveals no changes in relative expression levels of *Ano6*, *Ano8* and *Ano10*, and the $Na^+K^+2Cl^–$ co-transporter Nkcc1. Ano2 is strongly downregulated in the MOE of *Ano2*$^{–/–}$ mice. Unchanged levels of ACIII confirm tissue identity and indicate comparable MOE content in whole turbinate preparations from *Ano2*$^{+/+}$ and *Ano2*$^{–/–}$ mice. Error bars represent s.e.m. Note that MOE and VNO preparations not only contain the olfactory epithelium but also the underlying structures including cartilage and glands.

We tested for compensatory upregulation of key proteins such as components of the olfactory signal transduction cascade or other Anoctamin family members. We found unaltered expression levels of the olfactory signaling molecules ACIII (Figure 18c) and Cnga2 (Figure 18b) in western blots from MOE tissue of *Ano2*$^{+/+}$ and *Ano2*$^{-/-}$ mice. This is consistent with the unchanged expression of Cnga2 observed in immunohistochemistry (see Figure 13b). Similarly, neither immunohistochemistry nor immunoblotting indicated an upregulation of Ano1 in the MOE or the VNO of *Ano2*$^{-/-}$ mice (Figure 18d, see also Figure 15c). Other Anoctamin members shown to be expressed in the olfactory system are Ano6, Ano8 and Ano10 (Stephan et al., 2009; Rasche et al., 2010). We compared their mRNA expression levels in *Ano2*$^{-/-}$ and wild-type MOE by qRT-PCR and did not find significant changes (Figure 18e). Yet, in the same experiment Ano2 RNA levels were reduced to ~20% of the wild-type level confirming the genotype and indicating instability of the disrupted RNA probably due to nonsense-mediated RNA decay. Comparable expression levels of ACIII had already been shown in immunoblot analysis (Figure 18c) and unchanged ACIII levels in qRT-PCR thus indicated correct tissue identity and comparable tissue preparation. Also, expression of Nkcc1, the $Na^+K^+2Cl^-$ co-transporter thought to mediate Cl^- accumulation in OSNs, was not affected by the loss of Ano2 (Figure 18e).

3.5.3. Olfactory Ca^{2+}-activated Cl^- currents are absent from *Ano2*$^{-/-}$ mice

Measurements in this section were performed by Balázs Pál and partly by Pawel Fidzinski (see preface).

3.5.3.1. Steady-state Ca^{2+}-activated Cl^- currents in OSNs

If Ano2 is the molecular identity of the olfactory CaCC, Ca^{2+}-activated Cl^- currents should be absent from olfactory neurons of *Ano2*$^{-/-}$ mice. We investigated Ca^{2+}-activated Cl^- currents by whole-cell patch-clamp analysis of OSNs in slices from the MOE under conditions that largely suppress cation currents (Figure 19). Ca^{2+}-activated Cl^- currents were observed under steady-state conditions when we applied Ca^{2+} with the patch pipette allowing for equilibration with the cytoplasm of the cell prior to recording. We detected Ca^{2+}-activated Cl^- currents with 1.5 µM and 13 µM intracellular free Ca^{2+} but not in the absence of intracellular Ca^{2+} (Figure 19a). Currents with 1.5 µM Ca^{2+} showed characteristic time dependence and outward rectification while at 13 µM free Ca^{2+} the current-voltage relationship became linear (Figure 19a,c) similar to the currents described for heterologously expressed Ano2 (Stephan et al., 2009; Pifferi et al., 2009a; Sagheddu et al., 2010). In *Ano2*$^{-/-}$ OSNs, no currents were detected with 1.5 µM or 13 µM intracellular free Ca^{2+} (Figure 19b,c) demonstrating that Ca^{2+}-activated Cl^- currents of OSNs elicited by sustained high intracellular Ca^{2+} are mediated by Ano2.

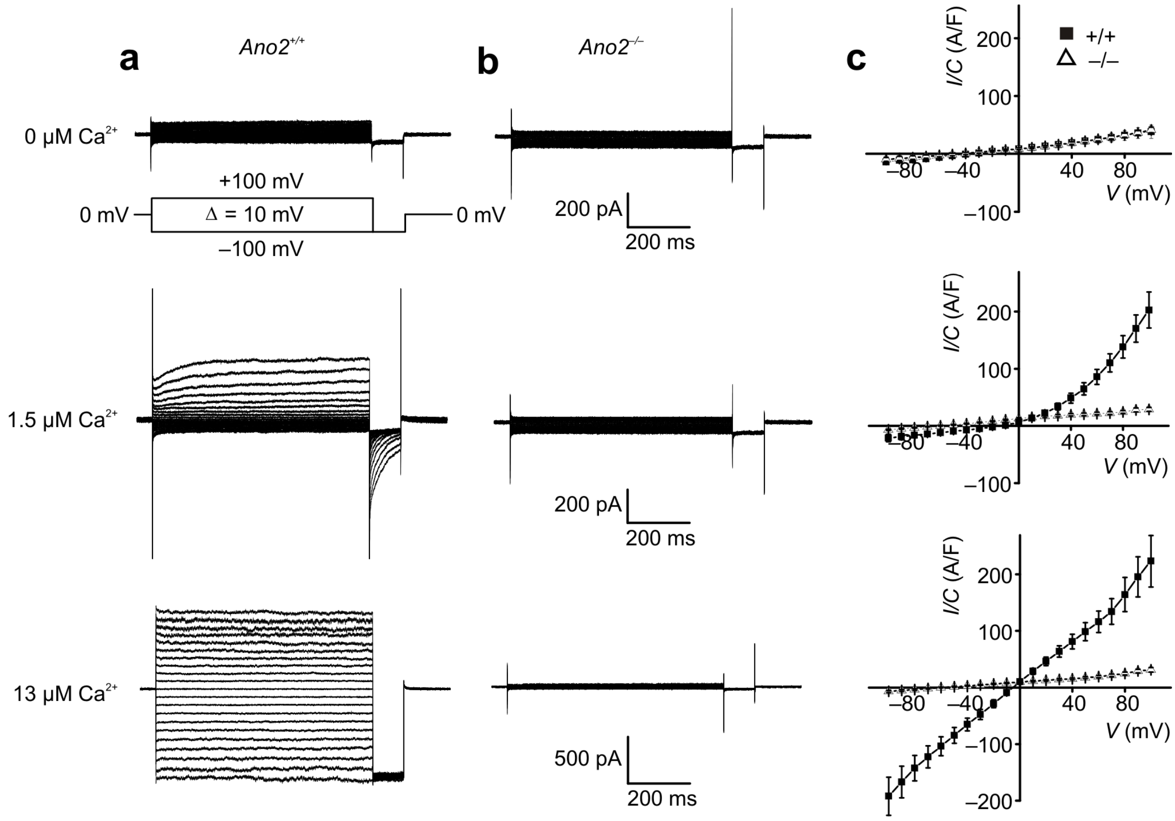

Figure 19 | Steady-state Ca^{2+}-activated Cl^- currents are absent from *Ano2$^{-/-}$* OSNs.
Patch-clamp recordings of Ca^{2+}-activated Cl^- currents in OSNs in slices from the MOE in the whole-cell configuration. Free intracellular Ca^{2+} concentrations are set by the solution in the patch pipette. The voltage-clamp protocol is shown in (a). **(a)** Typical current traces obtained from *Ano2$^{+/+}$* OSNs in the presence of 0 µM, 1.5 µM, or 13 µM free Ca^{2+} in the patch pipette. With 1.5 µM Ca^{2+} the currents show time-dependence and outward rectification (middle) that is lost with 13 µM free Ca^{2+} (bottom). **(b)** Recordings from *Ano2$^{-/-}$* OSNs under conditions as in (a) reveal no Ca^{2+}-activated Cl^- currents with intracellular free Ca^{2+} (middle, bottom). **(c)** Averaged relationship between current densities (*I*/*C*) of steady-state currents and holding voltage (*V*) with 0 µM, 1.5 µM or 13 µM Ca^{2+} in the pipette. Error bars, s.e.m. Number of cells measured: 0 µM Ca^{2+}, 7 *Ano2$^{+/+}$*, 7 *Ano2$^{-/-}$*; 1.5 µM Ca^{2+}, 15 *Ano2$^{+/+}$*, 11 *Ano2$^{-/-}$*; 13 µM Ca^{2+}, 14 *Ano2$^{+/+}$*, 10 *Ano2$^{-/-}$* from ≥3 mice per genotype.

3.5.3.2. Transient Ca^{2+}-activated Cl^- currents in OSNs

Since the previous measurements were performed under steady-state high intracellular Ca^{2+} levels, transient Ca^{2+}-activated Cl^- currents could still persist in *Ano2$^{-/-}$* OSNs. To exclude this possibility, we investigated currents induced by flash photolysis of caged Ca^{2+} and 8-Br-cAMP in isolated olfactory receptor neurons (Figure 20). Uncaging of Ca^{2+} from DMNP-EDTA in wild-type OSNs elicited large transient currents that activated rapidly and reversed close to the Cl^- equilibrium potential (Figure 20a). In *Ano2*$^{-/-}$ OSNs, these currents were reduced to ~10% of wild-type currents and reversed close to the K^+ equilibrium potential (Figure 20a,b). They were possibly mediated by the opening of Ca^{2+}-activated K^+ channels. Similar, flash release of 8-Br-cAMP from BCMCM-caged 8-Br-cAMP, which gates CNG channels and thereby indirectly activates CaCCs, gave rise to large currents in *Ano2*$^{+/+}$ OSNs but not in *Ano2*$^{-/-}$ OSNs (Figure 20c). The ~10% current that remained in measurements with *Ano2*$^{-/-}$ neurons probably represents cation currents through CNG channels. This is in good agreement with results from previous studies (Boccaccio and Menini, 2007; Pifferi et al., 2009b). Since both, steady-state and transient Ca^{2+}-activated Cl^- currents are completely abolished in *Ano2*$^{-/-}$ OSNs, we conclude that Ano2 is the olfactory CaCC. The lack of any detectable Ca^{2+}-activated Cl^- currents excludes the possibility of compensation by other CaCCs.

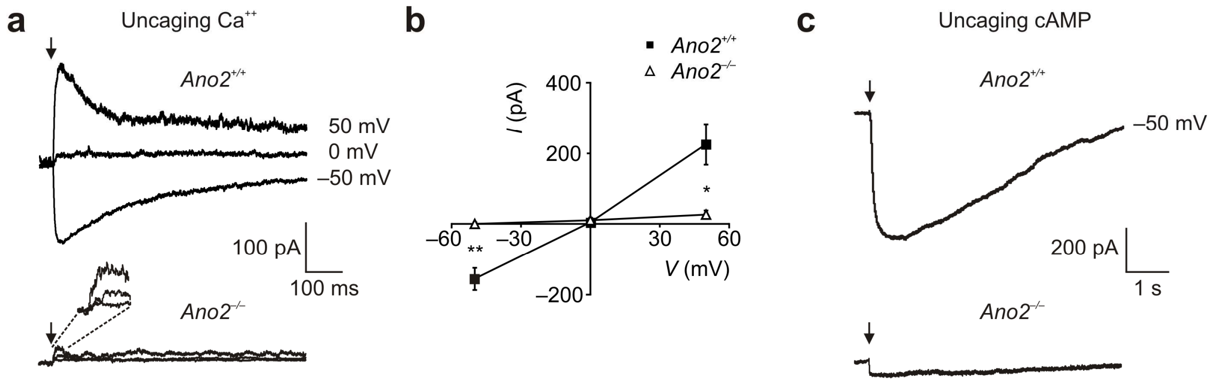

Figure 20 | Transient Ca^{2+}-activated Cl^- currents are absent from Ano2$^{-/-}$ OSNs.
Patch-clamp measurements of Ca^{2+}-activated Cl^- currents induced by flash photolysis of Ca^{2+} and 8-Br-cAMP in isolated OSNs under symmetrical Cl^- in the whole-cell configuration. **(a)** Typical current responses to a sudden increase of intracellular free Ca^{2+} in isolated OSNs from both genotypes. Arrows indicate flash that releases Ca^{2+} from DMNP-EDTA. Cells were clamped to –50 mV, 0 mV, and +50 mV. Inset, larger magnification to reveal currents remaining in *Ano2*$^{-/-}$ OSNs. **(b)** Peak currents (*I*) elicited by uncaging Ca^{2+} as function of holding voltage (*V*), averaged from 8 *Ano2*$^{+/+}$ and 7 *Ano2*$^{-/-}$ OSNs with ≥3 mice per genotype. Error bars, s.e.m. Significance levels (two sample t-test): *, $P < 0.05$; **, $P < 0.01$. **(c)** Typical currents elicited by flash release of 8-Br-cAMP (arrows) in isolated OSNs from *Ano2*$^{+/+}$ and *Ano2*$^{-/-}$ mice held at –50 mV. Mean amplitudes were –445 ± 111 pA for *Ano2*$^{+/+}$ and –43.2 ± 9.9 pA for *Ano2*$^{-/-}$ OSNs (±s.e.m., $P = 0.0016$).

3.5.3.3. Steady-state Ca^{2+}-activated Cl^- currents in VSNs

Ca^{2+}-activated Cl^- currents in VSNs have been investigated by only few groups (Yang and Delay, 2010; Kim et al., 2011). We tested if Ca^{2+}-activated Cl^- currents could be activated in sensory neurons of acutely isolated VNO slices in the whole-cell patch clamp configuration. In the absence of free Ca^{2+} we observed low background currents. Raising intracellular free Ca^{2+} to 1.5 µM elicited Ca^{2+}-activated Cl^- currents with outward rectification and time dependence (Figure 21a,c) similar to the currents described for heterologously expressed Ano2 (Stephan et al., 2009; Pifferi et al., 2009a; Sagheddu et al., 2010). In *Ano2*$^{-/-}$ VSNs Ca^{2+}-activated Cl^- currents were mostly absent (Figure 21b), even though a few cells showed currents that were up to twofold larger than background currents observed without Ca^{2+}. Yet, larger Ca^{2+}-activated Cl^- currents were dependent on Ano2 as revealed by averaged current-voltage curves (Figure 21c). Thus, CaCCs of VSNs predominantly depend on Ano2 and the contribution of the co-expressed CaCC Ano1 to VSN currents seems minor.

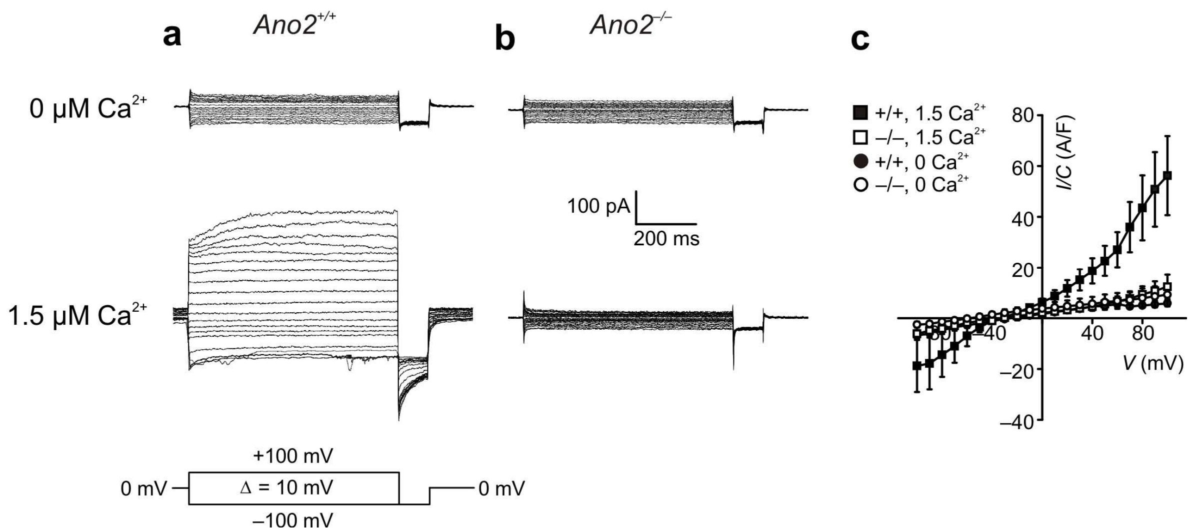

Figure 21 | Steady-state Ca^{2+}-activated Cl^- currents are absent from *Ano2*$^{-/-}$ VSNs.
Patch-clamp recordings of Ca^{2+}-activated Cl^- currents in VSNs in slices from the VNO in the whole-cell configuration. Free intracellular Ca^{2+} concentrations are set by the intracellular solution in the patch pipette. The voltage-clamp protocol is shown in (a). **(a)** Typical current traces obtained from *Ano2*$^{+/+}$ vomeronasal sensory neurons with 0 µM (top) and 1.5 µM (bottom) free Ca^{2+} in the patch pipette. Recordings with 1.5 µM Ca^{2+} reveal currents with characteristic time-dependence and outward rectification that are not detected with 0 µM Ca^{2+}. **(b)** Recordings from *Ano2*$^{-/-}$ OSNs under conditions as in (a) do not show Ca^{2+}-activated Cl^- currents in the presence of 1.5 µM Ca^{2+} (bottom). **(c)** Averaged relationship between current densities (*I/C*) of steady-state currents and holding voltage (*V*) with 0 µM and 1.5 µM free Ca^{2+} in the pipette for both genotypes. Number of cells measured: 1.5 µM Ca^{2+}, 7 *Ano2*$^{+/+}$, 7 *Ano2*$^{-/-}$; 0 µM Ca^{2+}, 5 *Ano2*$^{+/+}$, 5 *Ano2*$^{-/-}$ from ≥3 mice per genotype. Error bars, s.e.m.

3.5.4. No change of Cl^- in the olfactory mucus of *Ano2*$^{-/-}$ mice

Efflux of Cl^- upon activation of CaCCs could contribute to mucosal ion and fluid homeostasis akin to the role of Ano1 in secretory epithelia. However, in measurements with Cl^- sensitive microelectrodes at the surface of the MOE we detected no differences in mucosal Cl^- concentrations. We found mucosal Cl^- concentrations of 84.0 ± 22.8 mM (s.e.m., n = 6) in *Ano2*$^{+/+}$ and 84.4 ± 9.0 mM (s.e.m., n = 11) in *Ano2*$^{-/-}$ mice. These values are similar to those obtained with microelectrode measurements from toad (Chiu et al., 1988) but differ from values found by EDX analysis in rat (Reuter et al., 1998) [see Table 2]. These measurements were performed by Balázs Pál (see preface).

3.5.5. Loss of Ano2 moderately reduces EOGs

To investigate how the loss of Ano2 and consequently the lack of Ca^{2+}-activated Cl^- currents during olfactory signal transduction affects receptor potential generation we measured the electro-olfactogram (EOG) response to odorants (Figure 22). The EOG is a negative electrical potential than can be recorded at the surface of the olfactory epithelium upon stimulation with odorants. It primarily represents the summated receptor potential of a population of OSNs (Scott and Scott-Johnson, 2002) and is thought to be mainly established by Cl^- (Nickell et al., 2006). In mice lacking key components of the canonical olfactory signal transduction EOGs are abolished or strongly reduced (Brunet et al., 1996; Belluscio et al., 1998; Wong et al., 2000). The EOG measurements were performed by Balázs Pál (see preface). We measured EOGs in two different configurations. In air-phase EOGs the surface of the turbinates is exposed to water-saturated air and odors are applied by an air puff. Mucosal ion concentrations are not disturbed in this setting and should match physiological levels. In contrast, in fluid-phase EOG measurements the turbinates are continuously superfused with Ringer's solution and mucosal ion concentrations equilibrate with the superfusate.

In the air-phase configuration we measured EOGs evoked by two different odor mixtures or the single odorant geraniol (Figure 22e) and found comparable EOG amplitudes in *Ano2*$^{+/+}$ and *Ano2*$^{-/-}$ mice. Thus, given that external mucus and ion concentrations are not disturbed, receptor potential generation in *Ano2*$^{-/-}$ mice is apparently normal. We then investigated EOGs in the fluid-phase configuration in which EOG answers were elicited by short puffs of odorants diluted in Ringer's solution (Figure 22a–d). An odorant mixture, single odorants or artificial coyote urine evoked negative potential excursions in EOG recordings from *Ano2*$^{+/+}$ and *Ano2*$^{-/-}$ MOE (Figure 22a,c,d). However, the EOG amplitude in *Ano2*$^{-/-}$ mice was reduced by roughly 40% as compared to wild-type. This reduction was also evident when olfactory signaling was initiated by raising intracellular cAMP levels through forskolin-dependent activation of ACIII (Figure 22b,c) indicating that the effect is independent of the type of odorant applied. These data show that when external ion concentrations are controlled by superfusion with buffer the loss of Ano2 results in a measurable difference in receptor potential generation of OSNs.

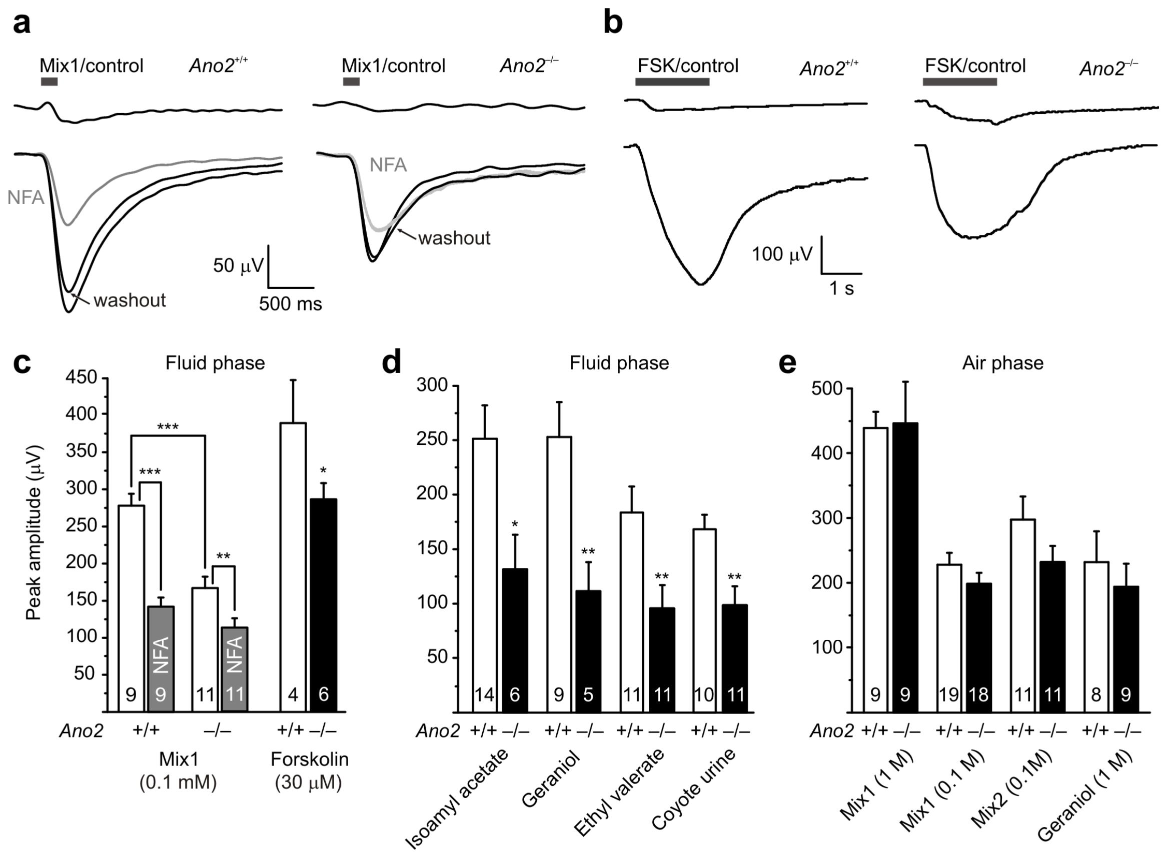

Figure 22 | Electro-olfactograms are only moderately changed in *Ano2*$^{-/-}$ mice.
(a) Typical fluid-phase EOGs from *Ano2*$^{+/+}$ (left) and *Ano2*$^{-/-}$ mice (right) with a mixture of 17 odorants (Mix1: isopentyl acetate, hexanal, eucalyptol, limonene, 2-heptanone, menthyl acetate, peppermint oil, eugenol, ethyl valerate, ethyl butyrate, ethyl tiglate, allyl tiglate, octanal, isobutyl propionate, acetal, hexanoic acid, 2-hexanene, 100 µM each). Bars above traces indicate application (200 ms) of odorant mixture (lower traces) or vehicle (upper trace). Grey traces were obtained with 300 µM NFA and black traces in normal Ringer's solution before and after exposure to NFA (washout). Traces were averaged from responses to 10 repeated stimuli. **(b)** Typical fluid-phase EOGs evoked by 2 s application of 30 µM forskolin (lower trace) or vehicle control (upper trace) to *Ano2*$^{+/+}$ (left) and *Ano2*$^{-/-}$ MOE (right). **(c)** Averaged EOG amplitudes from experiments in (a,b). **(d)** Averaged fluid-phase EOG amplitudes elicited by individual odorants at 1 mM concentration and with 1:20 diluted artificial coyote urine. FSK, forskolin. **(e)** Averaged air-phase EOG amplitudes from mice of both genotypes measured with different odors. "Mix1" is the same odorant mixture as in (a). "Mix2" contains 8 odorants (D-carvone, 1-heptanol, 2-methylbutyric acid, geraniol, isopentylamine, 2-hexanone, acetophenone, 1-octanal). Differences in responses between genotypes are not statistically significant. Numbers in columns represent number of measurements. Error bars, s.e.m. Significance levels (two sample t-test): *, $P < 0.05$; **, $P < 0.01$; ***, $P < 0.001$.

EOG responses are known to be efficiently inhibited by niflumic acid (NFA) which is assumed to specifically block olfactory CaCCs. When we added 300 µM NFA to the superfusate, EOG responses to an odorant mixture were reduced by ~50% (Figure 22a,c). However, addition of NFA to turbinates of *Ano2*$^{-/-}$ mice also inhibited EOG responses by ~30% thus revealing that only ~60% of the response to NFA is due to an inhibition of Ano2 (Figure 22a,c). Hence, previous studies on olfactory CaCCs based on NFA blockage may have overestimated the role of CaCCs in olfaction.

3.5.6. No change in tyrosine hydroxylase expression in the olfactory bulb of *Ano2*$^{-/-}$ mice

We next investigated if the lack of Ca^{2+}-activated Cl^{-} currents in *Ano2*$^{-/-}$ OSNs and the concomitant reduction in the receptor potential observed in fluid-phase EOG measurements of *Ano2*$^{-/-}$ mice affects input activity to the olfactory bulb. Expression of tyrosine hydroxylase in periglomerular cells of the olfactory bulb is indicative of neuronal input and its expression is severely reduced in mice that are anosmic (Baker et al., 1999) and when odorant stimulation is ablated by naris occlusion (Baker et al., 1993) or by inhibition of synaptic release with tetanus toxin (Yu et al., 2004).

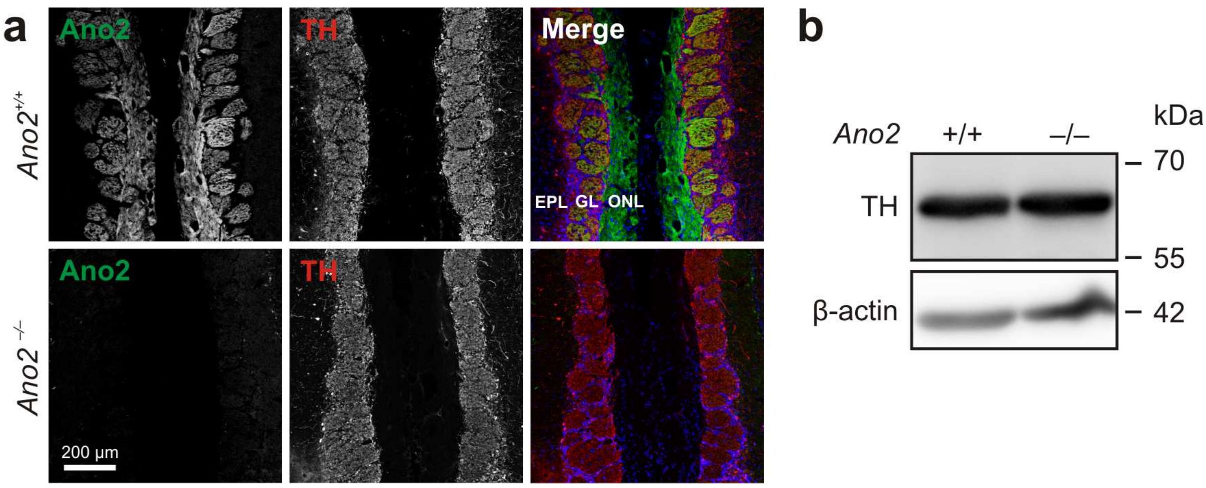

Figure 23 | No change in tyrosine hydroxylase expression in the olfactory bulb of *Ano2*$^{-/-}$ mice. **(a)** Confocal images of sections from the olfactory bulb of *Ano2*$^{-/-}$ mice and *Ano2*$^{+/+}$ mice labeled for Ano2 (rbAno2_N3-3) and tyrosine hydroxylase (TH). Section shows part of the olfactory bulb from both hemispheres, with cleft in center. Tyrosine hydroxylase expression is dependent on neuronal input and is not changed in *Ano2*$^{-/-}$ bulbs. EPL, external plexiform layer; GL, glomerular layer; ONL, olfactory nerve layer. **(b)** Immunoblot for tyrosine hydroxylase expression in extracts from *Ano2*$^{+/+}$ and *Ano2*$^{-/-}$ olfactory bulbs shows comparable levels in both genotypes. β-actin serves as loading control.

Tyrosine hydroxylase expression appeared normal in immunohistochemistry of the olfactory bulb from *Ano2*$^{-/-}$ mice (Figure 23a), and comparable tyrosine hydroxylase protein levels in olfactory bulbs of wild-type and *Ano2*$^{-/-}$ mice were found in immunoblot analysis (Figure 23b) indicating no gross changes in afferent input to the olfactory bulb.

3.5.7. Axonal convergence to the olfactory bulb is normal in *Ano2*$^{-/-}$ mice

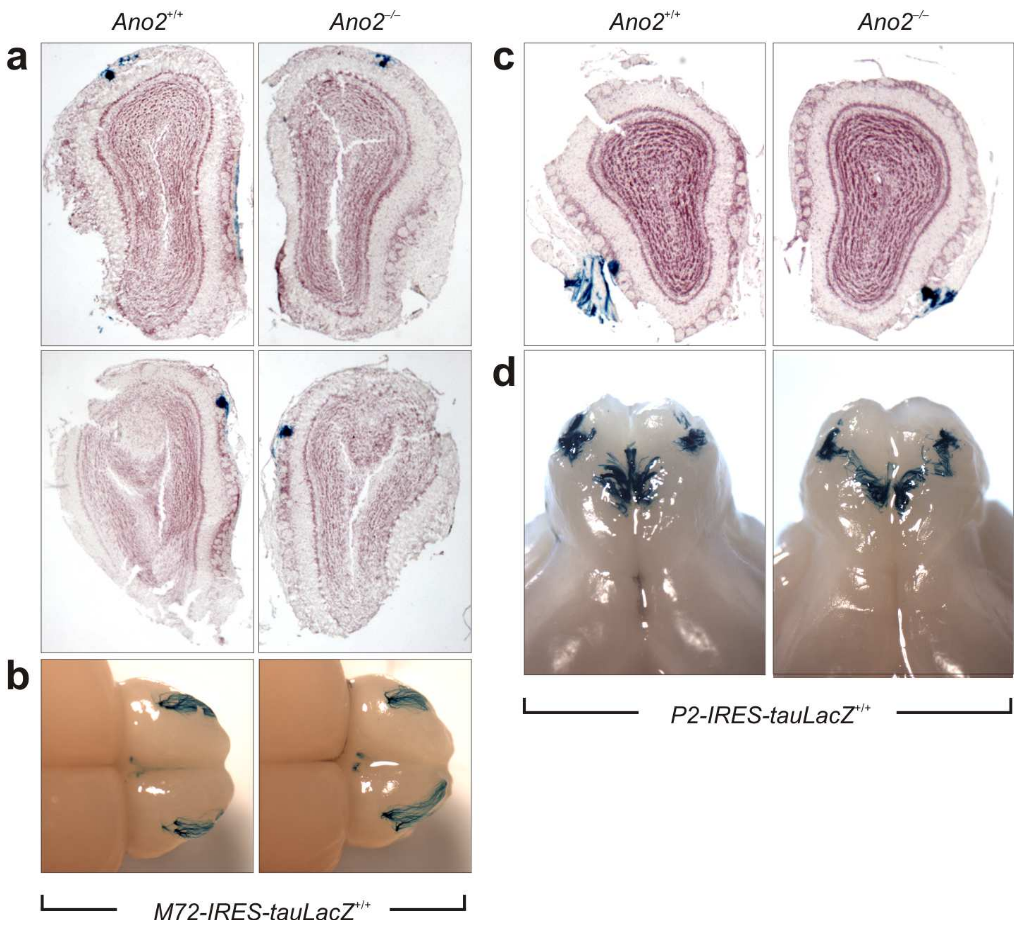

Figure 24 | No change in axonal convergence of M72^{+} and P2^{+} OSNs in *Ano2*$^{-/-}$ mice.
Axonal convergence of M72 or P2 expressing OSNs to glomeruli of the olfactory bulb visualized by β-galactosidase staining of bulbs from *Ano2*$^{-/-}$ and *Ano2*$^{+/+}$ mice homozygous for M72-IRES-tauLacZ or P2-IRES-tauLacZ. **(a)** Sections from *Ano2*$^{+/+}$ (left) and *Ano2*$^{-/-}$ (right) bulbs show similar locations of the dorsal (top) and medial (bottom) M72 glomeruli in both genotypes. **(b)** Image from the dorsal side of the intact olfactory bulb with unchanged patterns of M72 OSN convergence in *Ano2*$^{-/-}$ bulbs. **(c)** Sections from the bulb of *Ano2*$^{+/+}$ (left) and *Ano2*$^{-/-}$ (right) mice show comparable positions of the lateral P2 glomeruli. **(d)** The pattern of P2 OSN convergence imaged at the ventral side of the intact olfactory bulb is unchanged in *Ano2*$^{-/-}$ mice. Number of mouse pairs: P2, n = 12 (4–15 weeks old); M72, n = 7 (5–24 weeks old).

Neuronal activity has been shown to play a role in axonal convergence. When cAMP signaling (Imai et al., 2006; Chesler et al., 2007; Zou et al., 2007) or spontaneous neuronal activity (Yu et al., 2004) are disturbed by genetic mutations, when olfactory input is abolished by naris occlusion (Zou et al., 2004) or when olfactory signaling is missing in a competitive environment (Zhao and Reed, 2001), olfactory projections are perturbed and the olfactory map is not correctly established. To examine if Ano2 is involved in olfactory map formation we crossed our *Ano2*$^{-/-}$ mice to mice strains M72-IRES-tauLacZ and P2-IRES-tauLacZ that co-express the odorant receptor M72 and P2, respectively, together with an axon-targeted β-galactosidase (Mombaerts et al., 1996; Zheng et al., 2000). No obvious change in axonal convergence could be detected for OSNs expressing either the M72 or P2 receptor (Figure 24). These observations suggest that olfaction is not grossly impaired in *Ano2*$^{-/-}$ mice and that intrinsic OSN activity is not changed to a degree that affects axonal convergence and changes the olfactory map.

3.5.8. No olfactory deficits in the behaving *Ano2*$^{-/-}$ mouse

3.5.8.1. Olfaction-guided behaviors are normal

Many of innate and learned behaviors are guided by odors and are disturbed when olfaction is impaired. This includes maternal behaviors including nursing and aggression, male-male aggression and postnatal feeding. Mice lacking any of the olfactory transduction proteins G-olf, ACIII or Cnga2 have a high probability to die early after birth since they are not able to find the teats of their mothers and hence suffer from malnutrition (Brunet et al., 1996; Belluscio et al., 1998; Wong et al., 2000). They also show deficits in maternal behaviors and aggression (Mandiyan et al., 2005; Wang et al., 2006). In contrast to these described olfactory phenotypes, *Ano2*$^{-/-}$ mice survived normally and fed well. As their wild-type littermates, they were able to locate hidden food by olfactory cues and reacted with intensive sniffing to the presentation of unknown odors or urine of conspecifics. Matings of *Ano2*$^{-/-}$ mice to each other or to wild-type mice were productive and gave normally sized and well prospering litters. In daily routine work with these mice we observed apparently normal aggressive behavior and no obvious behavioral anomalies.

3.5.8.2. Normal olfactory discrimination and odor sensitivity

We tested if the lack of Ano2 affects olfactory function of mice in more subtle aspects such as discrimination between odors and complex mixtures of odors or odor sensitivity. Using an automated olfactometer, we tested *Ano2*$^{-/-}$ mice and wild-type littermates for their performance in an associative go no-go olfactory learning task (Figure 25). Mice were trained to sample two different stimuli, one of which was associated with a water reward, and to lick only in response to the rewarded odor.

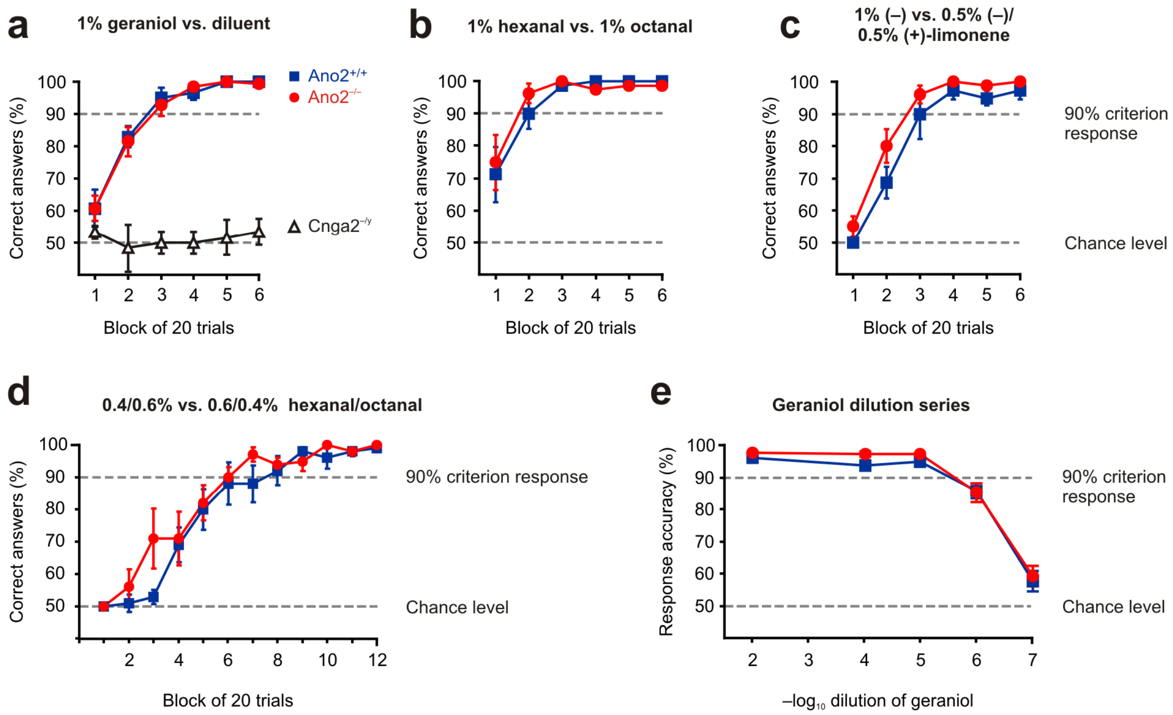

Figure 25 | Normal olfactory discrimination and sensitivity of *Ano2*$^{-/-}$ mice in olfactometry. **(a–d)** Learning curves representing discrimination ability between two olfactory cues during successive trials in automated olfactometry. **(a)** Like wild-type littermates, *Ano2*$^{-/-}$ mice learned to discriminate between 1% geraniol and the diluent mineral oil (n = 6 for each genotype). Anosmic *Cnga2*$^{-/y}$ mice (n = 3) could not detect 1% geraniol. **(b)** *Ano2*$^{-/-}$ mice and *Ano2*$^{+/+}$ littermates were able to discriminate between 1% hexanal and 1% octanal (n = 3 for each genotype), **(c)** between 1% (–)-limonene and an enantiomeric mixture of 0.5% (–)-limonene and 0.5% (+)-limonene (n = 4 for each genotype), and **(d)** between 0.4%hexanal/0.6%octanal and 0.6%hexanal/0.4%octanal (n = 5 for each genotype). **(e)** Odor detection threshold for geraniol as determined by olfactometry. Both *Ano2*$^{-/-}$ (n = 6) and *Ano2*$^{+/+}$ littermates (n = 6) detected geraniol and discriminated it from the diluent down to a dilution of 10^{-6}. The first data point with a geraniol dilution of 10^{-2} corresponds to (a). Error bars, s.e.m. There was no significant difference between *Ano2*$^{+/+}$ and *Ano2*$^{-/-}$ mice in any of these tests.

Disruption of Ano2 did not affect the performance of mice in olfactory discrimination of geraniol from the mineral oil solvent (Figure 25a). By contrast to *Ano2*$^{-/-}$ mice, *Cnga2*$^{-/y}$ mice showed a clear-cut impairment in the same task (Figure 25a), as reported (Brunet et al., 1996; Lin et al., 2004). Discrimination ability was neither reduced in more complex discrimination tasks such as distinguishing the two chemically similar aldehydes hexanal and octanal (Figure 25b), or differentiating between (–)-limonene and an enantiomeric mixture of equal parts of (+)- and (–)-limonene (Figure 25c). *Ano2*$^{-/-}$ mice also performed indistinguishable from their wild-type litter mates in a difficult discrimination task between two mixtures with differing parts of hexanal and octanal (0.4% hexanal/0.6% octanal versus 0.6% hexanal/0.4% octanal) that they were only able to complete successfully after a large number of trials (Figure 25d).

Using successive dilutions of geraniol we tested whether the loss of Ano2 affected odor sensitivity. With either genotype, odor detection dropped sharply when the dilution reached 10^{-7} (Fig. 8e). Thus, *Ano2*$^{-/-}$ mice show normal olfactory discrimination and odor sensitivity. We conclude that CaCCs are not essential for near-normal olfactory function.

3.6. Functional characterization of Ano2 in the retina

3.6.1. Ano2 co-localizes with Ano1 to synaptic endings of photoreceptors

A second major site of Ano2 expression is the eye where Ano2 can be readily detected in immunoblots (Figure 10, Figure 11). We investigated the subcellular localization of Ano2 in the retina by immunohistochemistry using *Ano2*$^{-/-}$ tissue as control (Figure 26). Ano2 localized to presynaptic structures of photoreceptors in the outer plexiform layer (Figure 26) confirming published data (Stöhr et al., 2009).

We also localized Ano1, the closest homolog of Ano2, to the Ano2-positive presynaptic structures in the outer plexiform layer (Figure 26a). Similar to the VNO (compare Figure 15), Ano1 was unchanged upon disruption of Ano2 (Figure 26a). Expression of Ano1 was also detected in some cells of the inner nuclear layer and of the ganglion cell layer. Our labeling used an Ano1 antibody that has been demonstrated to be specific in mouse colon using *Ano1*$^{-/-}$ tissue as control (Gomez-Pinilla et al., 2009) but has not been tested on retina.

3.6.2. Loss of Ano2 does not affect related proteins and vision

In the retina, Ano2 co-localized with the PSD-95 adaptor protein (Figure 26b), which is here found presynaptically, and with the plasma membrane Ca^{2+}-ATPase PMCA (Figure 26c). PSD-95 and PMCA together with Veli3 form a presynaptic complex organized at the scaffold protein MPP4 (Aartsen et al., 2006; Yang et al., 2007) that also includes Ano2 (Stöhr et al., 2009). PSD-95 directly interacts with the PDZ binding motif of Ano2, and in mice deleted for *Mpp4* Ano2 is lost from photoreceptors synaptic endings (Stöhr et al., 2009) as are PSD-95, Veli3 (Aartsen et al., 2006) and PMCA (Yang et al., 2007). Contrary, the loss of Ano2 affected neither PSD-95 nor PMCA expression (Figure 26b,c). Loss of *Mpp4* and accordingly Ano2 has been reported to impair synaptic transmission from rod photoreceptors to second-order neurons as found in electro-retinogram measurements (Yang et al., 2007) while another study did not find any differences in the electro-retinograph of *Mpp4*$^{-/-}$ mice (Aartsen et al., 2006). We looked at impairment of sight in *Ano2*$^{-/-}$ mice by measuring electro-retinograms and did not find any alteration in visual ability of *Ano2*$^{-/-}$ mice (data not shown).

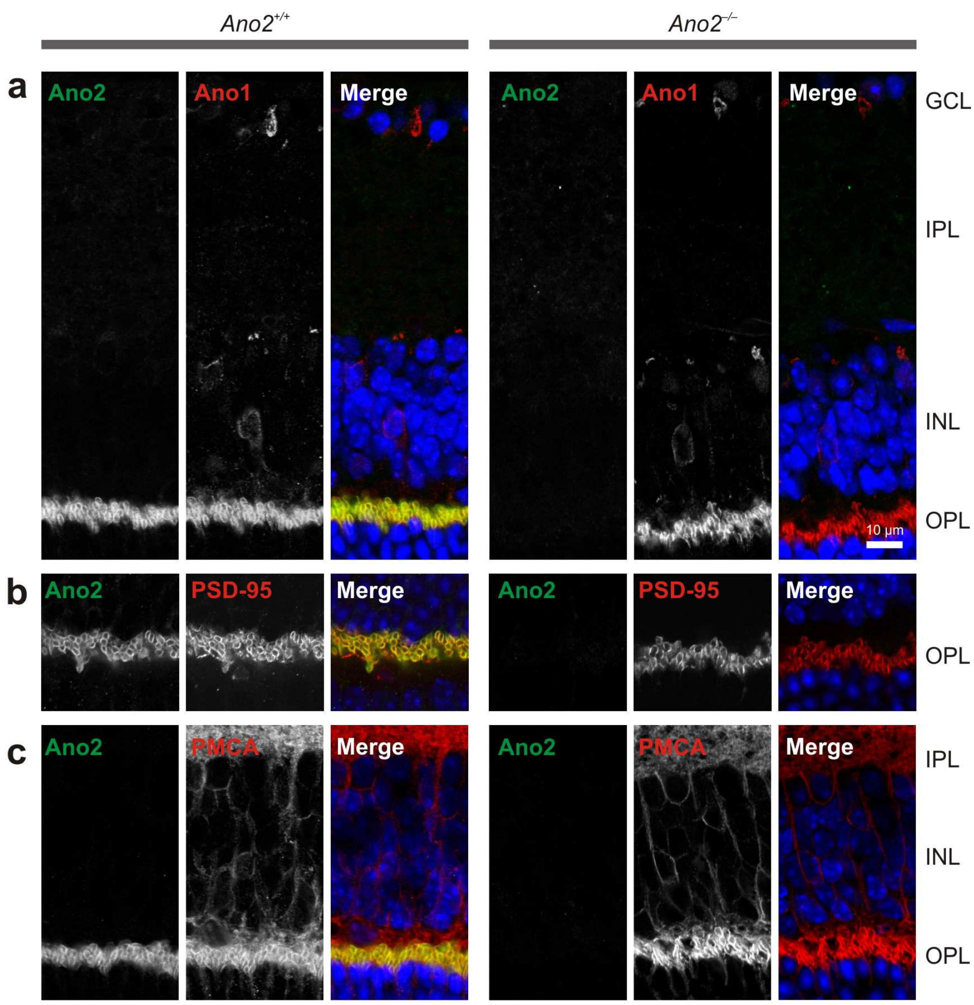

Figure 26 | Ano2 localizes to synaptic endings of photoreceptors in the retina.
Ano2 in the retina resides in the outer plexiform layer (OPL) where it co-localizes with Ano1, PSD-95 and PMCA. **(a)** Ano2 (antibody gpAno2_C1-3) co-localizes with Ano1 in synaptic endings of photoreceptors in the OPL. Ano1 expression is not changed when Ano2 is lacking (right). The Ano1 antibody additionally stains cells in the inner nuclear layer (INL) and the ganglion cell layer (GCL). **(b)** Immunostaining of *Ano2*$^{+/+}$ retina (left) shows localization of Ano2 (antibody rbAno2_N3-3) to the OPL and co-localization with PSD-95 which is unchanged in *Ano2*$^{-/-}$ retina (right). **(c)** Co-localization of Ano2 with PMCA (antibody rbAno2_N3-3) in the OPL (left). PMCA is not affected by the loss of Ano2 (right). Nuclei in the merged pictures are marked in blue. IPL, inner plexiform layer.

4. DISCUSSION

4.1. Ano2 is the olfactory CaCC

The concept that Ca^{2+}-activated Cl^{-} currents play a major role as amplifiers of the receptor current during olfactory signal transduction has been broadly accepted in the scientific literature (reviewed in Kleene, 2008; Pifferi et al., 2009c; Demaria and Ngai, 2010) and is included in many physiology text books. A ciliary Ca^{2+}-activated Cl^{-} conductance was first described in 1991 (Kleene and Gesteland) and was soon found to represent a major part of the odorant-induced current in OSNs of amphibians (Kurahashi and Yau, 1993; Kleene, 1993) and mammals (Lowe and Gold, 1993). The current fraction carried by CaCCs has been estimated from experiments with isolated OSNs to be 80–90% in rodents (Lowe and Gold, 1993; Reisert et al., 2003, 2005; Boccaccio and Menini, 2007) and is thought to provide strong amplification of the initial odorant-induced current carried by CNG channels (Kleene, 1993; Lowe and Gold, 1993). An important role for Cl^{-} in the generation of the receptor current has also been inferred from EOG measurements (Nickell et al., 2006). However, the unknown molecular identity of the olfactory CaCC has precluded direct functional testing.

In 2006 bestrophin-2 (Best2) was identified as a likely candidate for the molecular identity of the olfactory CaCC (Pifferi et al., 2006). Best2 shows ciliary localization and its biophysical properties — apart from ten times higher Ca^{2+} sensitivity — are very similar to those of the native olfactory CaCC. However, in OSNs of *Best2* knock-out mice Ca^{2+}-activated Cl^{-} currents are still present and olfactory physiology is undisturbed (Pifferi et al., 2009b). Thus, Best2 cannot account for the odor-induced Cl^{-} current. Instead it might have a role in neurogenesis of the olfactory system (Klimmeck et al., 2009). At the same time Ano2 emerged as a promising candidate for the olfactory CaCC (Stephan et al., 2009; Pifferi et al., 2009a). Ano2 is highly enriched in OSNs (Yu et al., 2005), localizes to cilia (Rasche et al., 2010) and recapitulates the main biophysical properties of the olfactory CaCC (Stephan et al., 2009; Pifferi et al., 2009a; Sagheddu et al., 2010).

The present work unambiguously identifies Ano2 as the long-sought CaCC of canonical olfactory signaling, or at least as an essential component thereof. We additionally identify Ano2 as the channel underlying the less characterized Ca^{2+}-activated Cl^{-} currents of sensory neurons in the VNO. Both currents are missing from *Ano2*$^{-/-}$ mice. Unexpectedly, the lack of Ano2 did not or only moderately affect receptor potential generation in two different configurations of EOG measurements. Neither the morphology of the olfactory organs nor a marker for neuronal input activity to the olfactory bulb or axonal convergence of olfactory neurons was affected in *Ano2*$^{-/-}$ mice. Also, in the behaving animal we did not find any impairment in olfactory discrimination ability or olfactory sensitivity. Our data show that, in contrast to the prevailing view, Ca^{2+}-activated Cl^{-} currents are not needed to achieve near-physiological levels of olfaction.

4.2. Ano2 is the sole CaCC of OSNs

We measured Ca^{2+}-activated Cl^{-} currents of OSNs under steady-state conditions and upon transient activation. In recordings under steady-state conditions we applied Ca^{2+} via the patch pipette while transient currents were elicited by photorelease of caged Ca^{2+} or caged 8-Br-cAMP. In all settings, CaCC activity was completely lost from *Ano2*$^{-/-}$ OSNs. We conclude that Ano2 represents the sole CaCC at the plasma membrane of OSNs and that Ano2 activity is not compensated by other CaCCs.

Studies on gene expression in the olfactory system support the notion that Ano2 represents the only Anoctamin at the plasma membrane of OSNs. Ano2 tops a list of genes highly enriched in OSNs over other cells of the MOE (Yu et al., 2005), and it is the only Anoctamin consistently identified in high amounts in mass spectrometric screens of olfactory membranes (Mayer et al., 2009; Stephan et al., 2009; Rasche et al., 2010). No such enrichment was shown for the other Anoctamins Ano1, Ano6, Ano8 and Ano10 known to be expressed in the MOE (Stephan et al., 2009; Rasche et al., 2010; Sagheddu et al., 2010). We have characterized the subcellular localization of the CaCC Ano1and found that it is expressed in apical membranes of glandular tissue, such as Bowman glands, goblet cells and nasal glands, consistent with its role in fluid secretion in other tissues. Presumably, the Ano1 signal found in RT-PCR and mass spectrometry of MOE preparations (Stephan et al., 2009; Rasche et al., 2010; Sagheddu et al., 2010) originates from such glandular tissue since these preparations not only contain OSNs but also supporting and basal cells as well as contaminations from tissue surrounding and underlying the MOE. Subcellular localization of Ano6, Ano8 and Ano10 has not been studied yet, but the loss of CaCC activity from *Ano2*$^{-/-}$ OSNs implicates that either these proteins are not expressed in OSNs, that they reside in distinct cellular compartments not accessible to our electrophysiology recordings or that they do not function as CaCCs. In case these Anoctamins are co-expressed with Ano2, a functional dependence, though, seems unlikely given that they are expressed at comparably lower amounts (Rasche et al., 2010), that in our experiments none of them is affected by the loss of Ano2 and that some of them are ubiquitously expressed (Schreiber et al., 2010).

4.3. Biophysical properties of the olfactory CaCC

Our recordings of steady-state Ca^{2+}-activated Cl^{-} currents were performed *in situ* in slices of the MOE. This experimental setting partly preserves the native environment and enabled us to measure steady-state currents of olfactory CaCCs at different voltages and Ca^{2+} concentrations. The biophysical properties we found comply with the characteristics described in whole-cell patch-clamp measurements of heterologously expressed Ano2 (Pifferi et al., 2009a). At 1.5 µM free intracellular Ca^{2+} the olfactory CaCC was incompletely activated with characteristic time-dependence and outward rectification while at 13 µM Ca^{2+} the channel showed ohmic behavior and higher currents. This is in agreement with voltage-dependent half-maximal Ca^{2+} concentrations of 1.2–4.9 µM described for Ano2 (Stephan et al., 2009; Pifferi et al., 2009a). The Ca^{2+}-dependent rectification also fits with data for the native olfactory CaCC that have been mainly obtained from inside-out patch-clamp measurements (Reisert et al., 2003; Pifferi et al., 2006, 2009b). In these measurements the Ca^{2+} concentrations needed for half-maximal activation are higher at negative holding potentials than at positive potentials reflecting indirectly the Ca^{2+}-dependent rectification known from classical CaCCs. Also, the values for half-maximal activation by Ca^{2+} of 2.2–4.7 µM in rodents are in good agreement with our data.

Our recordings of transient Ca^{2+}-activated Cl^- currents elicited by uncaging Ca^{2+} or 8-Br-cAMP agree with previous studies (Boccaccio and Menini, 2007; Pifferi et al., 2009b). As reported, the currents are promptly activated after photorelease of caged Ca^{2+} suggesting direct gating of Ano2 by Ca^{2+}. They are also rapidly activated by 8-Br-cAMP that indirectly activates Ano2 by triggering influx of Ca^{2+} through CNG channels.

4.4. Olfactory Ca^{2+}-activated Cl^- currents are dispensable for olfaction

4.4.1. The receptor potential is not mainly established by CaCCs

Confirming many previous studies we found that in isolated olfactory receptor neurons the major part of the cAMP-activated receptor current is carried by CaCCs (Kleene, 2008; Frings, 2009; Pifferi et al., 2009c). Upon activation by cAMP we observed approximately ten times higher total currents in wild-type OSNs than in *Ano2*$^{-/-}$ OSNs thus supporting estimates of ~90% of the receptor current being carried by Cl^-. For isolated OSNs, our data comply with a prominent role of the olfactory CaCC in signal amplification.

However, our Ano2 knock-out mouse model allowed us to analyze how the lack of Ano2 and thus the loss of olfactory Ca^{2+}-activated Cl^- currents affects generation of the receptor potential in OSNs *in situ*. EOGs provide a tool to measure the summated receptor potential over many OSNs in a setting in which the native environment of the OSNs is preserved (Scott and Scott-Johnson, 2002). It has been postulated to be mainly based on Cl^- currents since it is effectively blocked by NFA (Nickell et al., 2006). When CaCCs contribute substantially to the EOG, deletion of Ano2 should results in a drastic reduction in EOG amplitudes.

Surprisingly, in *Ano2*$^{-/-}$ mice we found only moderate or no reduction, respectively, using two different configurations of EOG measurements. The near-normal EOG in *Ano2*$^{-/-}$ mice was not due to a compensatory upregulation of the primary CNG transduction channel since Cnga2 expression was normal in both immunostainings and immunoblots. The two different settings we used for EOG measurements were the air-phase and fluid-phase configuration. In air-phase EOGs the turbinates are exposed to humidified air and an odorant is applied by an air puff, thus leaving physiological ion concentrations undisturbed and better reflecting native conditions. In contrast, in the fluid-phase configuration the surface of the turbinates is continuously superfused with Ringer's solution and mucosal ion concentrations equilibrate with the superfusate. In this configuration the odorants are applied in solution.

In the air-phase configuration of the EOG we did not find any difference in voltage amplitudes between both genotypes. However, in the fluid-phase configuration the EOG response to odorant stimulation was reduced by ~40% in *Ano2*$^{-/-}$ mice. EOG amplitudes were similarly reduced when we activated the EOG response by addition of the adenylate cyclase activator forskolin indicating a general change in olfactory physiology which is not dependent on the odor stimulus. The differences we observed between both configurations are likely due to the different extracellular ionic environment. In *Ano2*$^{-/-}$ mice the loss of CaCC activity might induce compensatory changes in the ionic composition of the mucus. Accordingly, in the air-phase configuration where mucosal ion concentrations are undisturbed the EOG is not affected, while in fluid-phase EOGs where the superfusate dictates extracellular ion concentrations changes in olfactory physiology become apparent. Nevertheless, we can exclude compensatory changes in external Cl^- concentrations since mucosal Cl^- was unaffected in our measurements with ion-selective microelectrodes. Also, superfusing the turbinates might change several aspects of olfactory transduction that could account for the differences observed. For example, accessibility of some water-soluble odorants to the cilia might be more effective in fluid-phase EOGs while at the same time odorant binding proteins and other main mucosal components might get washed out and hydrophobic odorants might be solubilized less efficiently.

In any case, the maximum reduction in receptor potential amplitude we detected in *Ano2*$^{-/-}$ mice was 40%. This differs substantially from measurements in mice deleted for the major olfactory signaling molecules. Air-phase EOGs of G-olf, ACIII, and CNG knock-out mice are virtually abolished or strongly reduced (Brunet et al., 1996; Belluscio et al., 1998; Wong et al., 2000). Our data do not agree with a crucial role of CaCCs in olfaction and suggest that Ca^{2+}-activated Cl^- currents contribute only marginally to the generation of the receptor potential. We conclude that olfactory CNG channels do not need a boost by

CaCCs. In contrast to what has been previously thought, the main fraction of the EOG is not established by the activity of CaCCs.

Previous studies have inferred a major contribution of Cl^- to the EOG from effective pharmacological inhibition by the anion channel blocker NFA (Nickell et al., 2006). However, NFA also modulates several other ion channels apart from CaCCs and is an activator of Ca^{2+}-activated K^+ channels (Greenwood and Leblanc, 2007). In our experiments the wild-type EOG was effectively blocked by NFA, yet we also found inhibition by NFA (~30%) in the absence of Ano2. Thus, only ~60% of the answer to NFA in EOGs can be attributed to inhibition of CaCCs while ~40% of the reduction must be mediated by the block of other channels. We showed, that in the olfactory system NFA does not specifically act on olfactory CaCCs and, hence, previous studies based on NFA might have overestimated the role of CaCCs in olfactory signaling.

4.4.2. Comparable olfactory physiology in *Ano2*$^{-/-}$ and *Nkcc1*$^{-/-}$ mice

The maximal reduction by ~40% that we observed in EOG amplitudes of *Ano2*$^{-/-}$ mice is inconsistent with data gained from isolated OSNs that suggest a major contribution of Ano2 to generation of the receptor potential. However, it fits well with data from mice deleted for the $Na^+K^+2Cl^-$ co-transporter Nkcc1. Nkcc1 is thought to be important for establishing the high intracellular Cl^- of OSNs that is a prerequisite for the depolarizing current carried by Cl^- channels. Hence deletion of Nkcc1 would abolish the inside-out gradient for Cl^- and CaCCs could no longer act excitatory. Consistent with this notion, Ca^{2+}-activated Cl^- currents are strongly reduced when Nkcc1 is deleted or pharmacologically blocked in isolated OSNs (Reisert et al., 2005). Yet, in the more physiological settings of EOG recordings the EOG amplitude in *Nkcc1*$^{-/-}$ mice is reduced by only ~40–60% (Nickell et al., 2006, 2007). In behavioral tests with olfactometry, olfactory sensitivity is not affected (Smith et al., 2008). Even though these data question the role of CaCCs in olfactory transduction they have mainly been interpreted as evidence for the existence of other mechanisms of Cl^- accumulation that persist or compensate in *Nkcc1*$^{-/-}$ OSNs. The discrepancy between the data of isolated cells and the data *in situ* and *in vivo* is not understood. We have a similar situation in *Ano2*$^{-/-}$ mice in which Ca^{2+}-activated Cl^- currents are absent from isolated OSNs, but EOGs are only moderately reduced and olfactory sensitivity is not affected. Thus, our data suggest a different explanation for the olfactory physiology observed in *Nkcc1*$^{-/-}$ mice. Nkcc1 could be the sole Cl^- accumulator of OSNs, and the low effect on EOGs and the normal olfactory sensitivity is owed to the minor contribution of CaCCs to generation of the receptor potential.

The ~57% reduction of fluid-phase EOGs in *Nkcc1*$^{-/-}$ mice (Nickell et al., 2007) is higher than the reduction by ~40% seen in fluid-phase EOGs of *Ano2*$^{-/-}$ mice. The difference is even more prominent in comparison to air-phase EOGs, in which we did not detect any changes in *Ano2*$^{-/-}$ mice. Upon deletion of *Nkcc1* the intraciliary Cl^- concentration is expected to be close to equilibrium and, in this case, opening of Ano2 channels would rather shunt than amplify the receptor current. Such a shunting inhibition might underlie the larger decrease of EOG amplitudes in *Nkcc1*$^{-/-}$ mice than in *Ano2*$^{-/-}$ mice.

Yet, a different interpretation of the changes in olfactory physiology of *Nkcc1*$^{-/-}$ mice cannot be excluded. The function of Nkcc1 as the basolateral Cl^- transporter important for Cl^- accumulation in secretory cells is well described and *Nkcc1*$^{-/-}$ mice produce less saliva (Evans et al., 2000). Considering that the olfactory mucus is in direct contact with cilia, mucosal changes might have direct impacts on olfactory signal transduction. Thus, impairment of function of nasal glands and Bowman glands in *Nkcc1*$^{-/-}$ mice might indirectly affect olfactory signal transduction and could also cause reduction in EOG amplitudes.

4.4.3. Normal olfactory morphology in the absence of CaCCs

Normal function of the olfactory system was also suggested by the lack of morphological and biochemical changes in any of the olfactory organs. Neither MOE, nor SOM, VNO or the olfactory bulb showed morphological anomalies and key olfactory proteins were unaffected. We also found apparently normal input activity to the olfactory bulb as indicated by the unchanged expression of the input activity marker tyrosine hydroxylase. By contrast, in mice that are anosmic (Baker et al., 1999; Trinh and Storm, 2003) or in which odorant stimulation is ablated by naris occlusion (Baker et al., 1993) tyrosine hydroxylase expression is severely reduced. Such reduction is also observed when synaptic transmission of OSNs is inhibited (Yu et al., 2004).

Normal olfactory physiology was also indicated by unchanged axonal convergence of two selected ORs on olfactory glomeruli. Assuming that the two chosen ORs, M72 and P2, are representative for the whole OR repertoire this suggests normal olfactory map formation in the absence of Ano2. Ano2 does not play a major role in the cAMP-dependent intrinsic signaling activity known to be crucial for correct olfactory map formation (Zou et al., 2007; Imai et al., 2006; Chesler et al., 2007). Given the normal morphology of the olfactory system and the unchanged olfactory map formation an essential function of Ano2 in development of the olfactory system can also be excluded.

4.4.4. Olfaction in the behaving animal is independent of olfactory CaCCs

In stark contrast to knock-out mice of the three major olfactory signaling molecules upstream of the CaCC, *Ano2*$^{-/-}$ mice did not show any of the typical features of anosmia. *Ano2*$^{-/-}$ mice thrived well and showed no obvious deficits in aggression or mating behavior, unlike reported for knock-out mice of G-olf (Belluscio et al., 1998), ACIII (Wong et al., 2000; Wang et al., 2006) and the CNG channel (Brunet et al., 1996; Mandiyan et al., 2005).

A non prominent contribution of Ano2 to generation of the receptor potential and olfaction was also supported on the behavioral level. Using quantitative olfactometry we found neither changes in olfactory discrimination nor in olfactory sensitivity in *Ano2*$^{-/-}$ mice. Yet, mice deleted for the olfactory transduction channel CNG have severely impaired olfaction (Brunet et al., 1996; Lin et al., 2004) and, in our tests, did not succeed in the simple task of discriminating geraniol from the diluent. In addition to such simple discrimination tasks, we conducted olfactometric discrimination tests of gradually increasing difficulties and with odorants of distinct chemical classes in order to reveal possible subtle changes in olfactory performance. Also on difficult tasks *Ano2*$^{-/-}$ mice performed indistinguishable from their littermates suggesting normal olfactory ability.

The main effect one might expect from the loss of signal amplification during olfactory transduction would be an impairment of olfactory sensitivity. We tested the olfactory sensitivity of *Ano2*$^{-/-}$ mice with the odorant geraniol. Since it is not detected by anosmic *Cnga2*$^{-/y}$ mice, we assume that geraniol stimulates exclusively classical OSNs in the MOE thus allowing us to reveal possible changes in this pathway. With geraniol we found comparable detection thresholds for *Ano2*$^{-/-}$ mice and their wild-type littermates. However, we cannot exclude that a subtle change in olfactory sensitivity might be present. We chose serial dilutions by a factor of ten and accordingly might have missed differences below this range. Also, we performed our experiments in mice of mixed background such that the inter-animal differences might be higher than the possibly small differences owed to the loss of Ano2. We conclude that Ano2 is neither needed to achieve near-physiological levels of olfactory sensitivity nor for olfactory discrimination.

4.4.5. The physiology of isolated OSNs is substantially disturbed

The large body of data that suggests strong amplification by olfactory CaCCs has been gained from electrophysiological studies with isolated OSNs (Kleene, 2008; Frings, 2009; Pifferi et al., 2009c). However, this concept is invalidated by our *Ano2*$^{-/-}$ mice. In a physiological context olfactory CaCCs do not contribute prominently to the receptor potential and olfaction in these mice is normal. The same inconsistency between measurements *in vitro* and measurements *in situ* and *in vivo*, respectively, has been observed in *Nkcc1*$^{-/-}$ mice (Reisert et al., 2005; Nickell et al., 2006; Smith et al., 2008).

What could be the cause for such discrepancy? A main reason might be the particularly sensible physiology of OSNs that is substantially damaged during isolation. In their native environment olfactory receptor neurons contact different extracellular surroundings: the cilia bath in the olfactory mucus, the soma and dendrites are enwrapped by supporting cells and contact interstitial fluid while the axons are organized in axon bundles and project into the olfactory bulb. This complex environment is disrupted during isolation procedures. Additionally, isolation results in axotonomy, a process that has been implicated in upregulation of CaCC activity (Sánchez-Vives and Gallego, 1994; André et al., 2003). Ion concentrations in the different extracellular environments of OSNs are uncertain and the few measurements available found differing values (see Table 2). Hence, it is not possible to faithfully recapitulate physiological conditions during measurements with isolated receptor cells. The changed properties of isolated OSNs are reflected in the change in intracellular Cl^- concentrations observed in a major fraction of neurons after isolation when compared to Cl^- concentrations of OSNs in intact epithelium (Kaneko et al., 2004). Additionally, contact points to neighboring cells such as gap junctions that might be involved in coupling OSN activity (Zhang, 2010) and tight junctions that control protein distribution between apical and basal membranes get disrupted and could result in disturbed ion homeostasis. Ano2 channels could get redistributed, and also, Ano2 might be generally expressed at low levels in the plasma membrane of OSNs (compare chapter 4.7.). At the soma, and also at the dendritic knob, the electrical accessibility of Ano2 would be much better than in cilia where due to the ciliary morphology distal channels might contribute little to voltage changes at the cell body (Lindemann, 2001). This could in part account for the discrepancy found between isolated OSNs and the situation *in situ* and *in vivo* reported in this work.

4.5. A role for Ano2 in olfactory signaling?

In contrast to what has been previously thought CaCCs are not crucial for olfactory function and mice lacking Ano2 show near-normal olfaction. However, Ano2 expression is highly specific for OSNs where it is strongly enriched in olfactory cilia, the place of chemoelectrical transduction. In rodents the olfactory CaCC is estimated to be present at eightfold excess over the primary olfactory transduction channel CNG in the ciliary membrane (Reisert et al., 2003). In the NCBI Reference Sequence database (Sayers et al., 2011) homologs of Ano2 are found among different animal kingdoms such as mammals, amphibians, fish and birds. The prominent expression in the olfactory system seems to be preserved among species. Even though to date expression studies of Ano2 are only available for mammals the presence of olfactory Ca^{2+}-activated Cl^- currents in amphibians and fish suggests a conserved function of Ano2 in olfactory signaling. Also, the UniGene EST profile (Sayers et al., 2011) for zebrafish indicates exclusive expression in olfactory rosettes. Hence, given that our data argue against a prominent function in signal amplification, what could be the rationale for such a prominent ciliary expression of Ano2? Or in other words, what is Ano2's function in olfaction?

The fact that olfactory CaCCs were initially identified in amphibians suggested that CaCCs confer resistance to variations in the extracellular ionic environment that these freshwater animals encounter (Kurahashi and Yau, 1993; Kleene and Pun, 1996). In freshwater the concentration gradients for monovalent cations across the ciliary membrane do not suffice for depolarization during odor transduction and instead Na^+ and possibly K^+ efflux would rather favor hyperpolarization. Yet, given the very low intracellular Ca^{2+} concentrations, the extracellular Ca^{2+} concentrations provide enough driving force for influx of Ca^{2+} through CNG channels and Ca^{2+} can contribute a large fraction of this current (Dzeja et al., 1999). The rise in intracellular Ca^{2+} in turn could then trigger CaCCs which mediate depolarization by Cl^- efflux thus strongly amplifying the initial Ca^{2+} current and reversing the hyperpolarization mediated by Na^+. Accordingly, the odorant response would be independent of most extracellular cations. This view is supported by studies by Kleene and Pun (1996) who found that removal of most mucosal cations did not diminish the amplitude of the OSN response. In amphibians and freshwater fish, resistance to variations in extracellular ions might be the main function of Ano2. In mammals, though, such a mechanism might only be effective under special conditions that escaped our analysis or, alternatively, Ano2 might just represent an evolutionary vestige. It could also be that the current carried by Ca^{2+} and Na^+ is the main transduction current and amplification is not needed (see chapter 4.6). Additionally, the mucus is a highly structured extracellular matrix (Menco and Farbman, 1992) and one could speculate that local ion concentrations are tightly controlled thus rendering the mucosal ion composition largely independent of the surrounding freshwater. The molecular identification of the olfactory CaCC now allows for verification of its physiological role in freshwater animals. Zebrafish, for instance, are a suitable model system in which gene knock-down is well established and olfaction tests are feasible.

The discovery that the olfactory Ca^{2+}-activated Cl^- current is also present in mammals (Lowe and Gold, 1993) and that it makes up for the major fraction of the receptor current in isolated OSNs has led to the well accepted hypothesis that CaCCs mediate strong amplification of the initial odor-induced currents carried by CNG channels (Kleene, 1993; Lowe and Gold, 1993). It is thought that CaCCs amplify the primary current, but introduce little additional noise thereby providing a high-gain, low-noise amplification system (Kleene, 1997). The near-normal receptor potential and the unchanged behavioral performance of our *Ano2*$^{-/-}$ mice do not support such a crucial role of CaCCs in olfaction. However, we cannot exclude that olfactory Ca^{2+}-activated Cl^- currents contribute a small amplification to the olfactory signal and thus provide an evolutionary advantage. This amplification step might only have a role in very specific situations that we did not cover in our characterization of olfactory physiology. Also, several compensatory changes might account for the lack of an obvious phenotype in *Ano2*$^{-/-}$ mice. For instance, other ion channels that we did not include in our controls could compensate for the function of Ano2. Contrary to the situation in mice deleted for any of the main olfactory signaling molecules, the CNG current persists in *Ano2*$^{-/-}$ OSNs, and thus plasticity of the processing brain circuits might easily adapt to the changes in OSN physiology and afford near-normal olfaction on the behavioral level.

One could also think of completely alternative functions of Ano2 in olfactory signaling. Ano2 might not be important for olfactory amplification but rather be involved in other aspects of the olfactory transduction cascade such as adaptation, desensitization or response termination thereby indirectly controlling spike frequency and synaptic transmission. In our characterization of the *Ano2*$^{-/-}$ mouse, we did not perform experiments to investigate these OSN properties. Yet, different paradigms to test for adaptation on the cellular and behavioral level are available. Such experiments could include measurements of the receptor current or of action potential firing in response to repetitive stimulation with odors or behavioral experiments with olfactometry in the presence of a background odor. We also might have missed differences in olfactory physiology that are mainly reflected in changes in synaptic transmission. Synaptic activity of OSNs can be measured by crossing *Ano2*$^{-/-}$ mice with mice expressing the pH-sensitive synaptic activity marker SynaptopHluorin under control of the OMP promoter (Bozza et al., 2004).

Ano2 might also have an important function in Cl^- secretion and control of the mucosal ion microenvironment, akin to the role of Ano1. However, in the unstimulated state, Ano2 does not play a major role in establishing mucosal Cl^- concentrations since we did not detect any changes in *Ano2*$^{-/-}$ mice. Alternative pathways for Ca^{2+} influx that could activate Ano2 independent of the CNG channel are not known.

A crucial role of Ano2 in development of the olfactory map has been excluded as discussed above (see chapter 4.4.3). Yet, Ano2 might play a role for survival of OSNs in a competitive environment. For instance, neurons that lack a functional CNG channel are slowly and specifically depleted from the olfactory epithelium and the bulb when adjacent neurons do express the CNG channel (Zheng et al., 2000; Zhao and Reed, 2001). Similarly, an effect of Ano2 deletion might become apparent in a competitive environment with neighboring Ano2-positive cells. Deletion of the floxed Ano2 specifically in one type of OSNs by expressing Cre under the promoter of a selected odorant receptor such the M71-IRES-Cre (Li et al., 2004) and crossing these mice with a reporter mouse line for visualization would allow such analyses.

When speculating on alternative functions of Ano2, reliable estimates on ionic concentrations in the cilia in the resting state and during transduction as well as on ionic composition of the mucus are crucial. Yet, direct measurements of ion concentrations in cilia are not feasible and only few estimates, mainly obtained at the dendritic knob, are available (see Table 2). Moreover, the geometry allows for large concentration changes and is predicted to result in fast Cl^- depletion and high intracellular Ca^{2+} levels during transduction (Lindemann, 2001). This suggests tightly controlled temporal and spatial dynamics of ciliary ion concentrations making predictions on ionic gradients extremely difficult. So far, estimates on the Cl^- equilibrium potential across the ciliary membrane are based on two different measurements with EDX analysis (Reuter et al., 1998) and Cl^- sensitive dyes (Kaneko et al., 2004) on OSNs in the resting state. Taking our own mucosal Cl^- measurements into account the predicted Cl^- equilibrium potential can vary from -20 mV in mice ($[Cl^-]_i$ = 37 mM, $[Cl^-]_o$ = 84 mM) to +5 mV in rat ($[Cl^-]_i$ = 69 mM, $[Cl^-]_o$ = 55 mM) [see Table 2]. In both cases efflux of Cl^- and depolarization is favored. However, provided that Cl^- is rapidly depleted during transduction the driving force for Cl^- efflux would dissipate fast and the high numbers of CaCCs in the ciliary membrane might provide a shunting inhibition. This scenario would only be reasonable if Cl^- replenishment is slow as it might be in the case when Nkcc1 is located basolaterally. Ciliary localization of Nkcc1 in contrast might, depending on the transport rate, rapidly replenish Cl^- and thus would not comply with such a model. Yet, the localization of Nkcc1 in OSNs is still a matter of debate (Reisert et al., 2005; Hengl et al., 2010). A shunting inhibition as described could introduce an additional Ca^{2+}-dependent adaptation mechanism into the olfactory signaling cascade.

Also, a temporal component could be involved in activation of CaCCs. Activation of Ano2 at negative potentials requires, at least locally, Ca^{2+} levels that rise above its half-maximally activating concentrations of 2–5 µM (Reisert et al., 2003; Pifferi et al., 2006, 2009b). Such Ca^{2+} levels are significantly higher than maximal Ca^{2+} levels reported for other neurons (Blaustein, 1988). Given the very small volume of the cilia such high Ca^{2+} concentrations might be readily achieved though. Nevertheless, Ca^{2+} buffering conditions in the cilia could profoundly affect the time course for Ano2 activation and the response kinetics of the overall receptor current. An important role for Ca^{2+} in regulating the olfactory response has been suggested by several studies (Reisert and Zhao, 2011). However, conclusive predictions on ion dynamics in cilia are difficult and mathematical modeling is needed to further elaborate rational hypotheses on ciliary ion dynamics and function of Ano2.

4.6. A need for signal amplification in olfactory transduction?

Our results question the need for signal amplification in the olfactory signal transduction cascade. Hence, is a signal amplification step in the olfactory transduction cascade a crucial concept for our understanding of odor perception and odor coding?

Odor detection and identification relies on a combinatorial system in which the differential activity of many OSNs is converted into a topographic map of multiple differentially activated olfactory glomeruli in the bulb. Such a coding principle in which each odor results in a unique spatial and temporal neuronal activity pattern relies on a large set of receptors operating at low selectivity. The requirement for low selectivity is met by the characteristics of the metabotropic transduction step. Dwell times on receptors are very short (Bhandawat et al., 2005) and the olfactory transduction operates with low efficiency and provides no amplification. Given the high sensitivity of olfaction, it has previously been postulated that amplification on the level of the olfactory transduction cascade is required and that olfactory CaCCs provide such an amplification mechanism (Frings, 2009). Yet, our data do not comply with such a function of olfactory CaCCs. Thus, it might be that the extremely high degree of convergence in the olfactory system, in which roughly 2,000 OSNs are connected with a single mitral cell in the olfactory bulb, suffices for accurate and sensitive olfaction. Temporal summation of multiple weak signals in a single glomerulus might cause excitation of a mitral cell even if each individual OSN is only slightly activated.

4.7. Localization of Ano2 in the olfactory system

Ano2 is strongly enriched in cilia of OSNs where it has been identified in several proteomic screens and in immunohistochemistry (Mayer et al., 2009; Stephan et al., 2009; Rasche et al., 2010; Hengl et al., 2010; Sagheddu et al., 2010). Our knock-out–controlled immunostainings confirmed this localization in the MOE. Analogous to the MOE, we found Ano2 in sensory cilia of the SOM, supporting the view that neurons of the SOM use the canonical olfactory signal transduction cascade (Ma et al., 2003). However, we were not able to detect Ano2 in the GG when trying different protocols and antibodies. Ano2 is also prominently expressed in the sensory epithelium of the VNO (see chapter 4.9). Additionally, we detected Ano2 in glomeruli and axons of OSNs in the olfactory bulb.

Compared to the MOE, Ano2 signal intensity in the bulb was much lower in both, immunoblots and immunohistochemistry. Our stainings suggest that Ano2 is exclusively expressed in axons and synaptic endings of OSNs in the olfactory bulb. This would be similar to what has been reported for odorant receptors (Barnea et al., 2004; Feinstein et al., 2004; Strotmann et al., 2004) and would comply with the localization of Ano2 in retina. However, an alternative interpretation of our immunostainings could be that Ano2 is expressed at low levels all over the cell membrane of the OSN. This would imply that we missed the low plasma membrane signal of Ano2 in sections from the nose, but were able to detect this Ano2 signal in the differentially processed olfactory bulb. Stainings of the bulb were done on cryosections, while tissue from nose was decalcified over several days and embedded in paraffin. Additionally, settings for microscopy of the MOE were adjusted to detect the predominant ciliary signal and thus would not allow for detection of a presumably very faint signal on the soma and axons. Such broad but rather low membrane expression together with very high enrichment of the channel in the ciliary membrane could be the consequence of a somehow “leaky” ciliary targeting mechanism possibly involving ciliary retention or localization signals.

4.8. Ano1 in the olfactory system

Consistent with its role in fluid secretion we found most prominent expression of Ano1 in apical membranes of glands of the olfactory system. This included acinar and duct cells from different types of mucous and serous nasal glands as well as glands important for mucus production of sensory epithelia, such as vomeronasal glands and Bowman glands of the MOE. Likewise, in the respiratory epithelium Ano1 localized exclusively to non-ciliated cells that — judged from their morphology — in many cases represented goblet cells, a type of unicellular gland.

Surprisingly, we additionally found Ano1 in the VNO where it co-localized with Ano2 to the apical sensory layer. Due to the inherent limit of microscopic resolution we cannot distinguish if Ano1 and Ano2 are expressed mutually exclusive or if they reside in the same microvilli. In analogy to the MOE, we assume that Ano2 is expressed in sensory microvilli of VSNs even though we did not perform co-stainings with respective markers. Co-staining with ezrin, which presumably marks microvilli of vomeronasal supporting cells, did not show any overlap with Ano2 thus supporting neuronal expression of Ano2. One could imagine that either both channels are co-expressed in all VSNs or that each channel is restricted to one of the two physiologically distinct layers of the VNO. *In situ* hybridization of the VNO or co-staining of isolated VSNs for Ano1 and Ano2 would be suitable approaches to resolve the expression of the two channels at the cellular level. Also, to date the specificity of our Ano1 antibody has been tested on *Ano1*$^{-/-}$ stomach only (Gomez-Pinilla et al., 2009) and there is still a chance that the Ano1 signal we observed is not specific. Yet, we can exclude cross-reactivity of the Ano1 antibody with Ano2 since the Ano1 signal is still present in *Ano2*-deleted mice.

4.9. CaCCs in the VNO

Ca^{2+}-activated Cl^- currents in vomeronasal neurons have only recently been described and their function is not yet understood. Similar to the postulated function in the MOE, a crucial role in signal amplification has been suggested for vomeronasal CaCCs (Yang and Delay, 2010; Kim et al., 2011). Even though the VNO uses signaling pathways distinct from the MOE the underlying principles are the same. Both pathways involve a G-protein coupled receptor whose activation culminates in activation of a cation channel permeant to mono- and divalent cations such as Na^+ and Ca^{2+}. This Ca^{2+} influx can result in activation of CaCCs. The direction of Cl^- fluxes in the VNO cannot be predicted, though, since so far no

Cl^- measurements are available. Vomeronasal CaCCs could act either excitatory or inhibitory.

We here identified Ano2 as the main CaCC of VSNs. *In situ* patch-clamp measurements of VSNs under steady-state conditions revealed Ca^{2+}-activated Cl^- currents with biophysical properties very similar to the CaCC in the main olfactory epithelium and heterologously expressed Ano2. Cl^- currents with time dependent kinetics and outward rectification were elicited by raising intracellular Ca^{2+} to 1.5 µM. This current was lacking from the *Ano2*$^{-/-}$ VNO. Thus, Ano2 represents the CaCC of VSNs, or at least a major component thereof. In few VSNs, we observed some residual CaCC activity which might be carried by the Ano1 channel. Ano1 also localizes to the sensory layer of the VNO and persists in *Ano2*$^{-/-}$ mice. Assuming that Ano1 is expressed in VSNs our results indicate that it does not contribute significantly to CaCC activity of VSNs or, in this tissue, might not be functional without Ano2. Alternatively, it might be that, due to experimental constraints, we have mostly patched VSNs from the apical layer. In case that Ano1 and Ano2 show layer-specific expression with Ano1 being exclusively expressed in VSNs of the basal layer we might have missed the persistent CaCC activity of the basally located neurons. A functional dependency of Ano1 on Ano2 seems improbable given that its expression is not affected by the loss of Ano2 and that it mediates Ca^{2+}-activated Cl^- currents when expressed on its own.

We did not investigate if the vomeronasal CaCC shows ohmic behavior with saturating intracellular Ca^{2+} concentrations, but given that it is mainly represented by Ano2 such a behavior is a reasonable assumption. The electrophysiological characterization of the vomeronasal CaCC is so far only rudimentary (Yang and Delay, 2010; Kim et al., 2011). Our observation with antibodies generated against the C-terminal epitope C1 that recognized the vomeronasal Ano2 efficiently while they did not or only very faintly give signals in the MOE, suggests that Ano2 isoforms or additional regulatory subunits are expressed in the two distinct olfactory organs. It remains to be seen if such a difference would also be mirrored in differing channel properties. In view of the distinct signaling pathways used by the two olfactory systems functional differences in Ano2 seem reasonable. However, one could also imagine a common role of Ano2 in both olfactory organs. In the light of this work that fundamentally questions the postulated function of CaCCs as amplifiers in the olfactory system, the analysis of the physiological role of vomeronasal Ca^{2+}-activated Cl^- currents could help in assigning an alternative function to these olfactory CaCCs.

To further elucidate the functional consequence of the loss of CaCC activity in VSNs subsequent levels of transduction and information processing could be investigated. It would be interesting to see how the lack of CaCCs affects receptor potential generation in the VSNs and if electro-vomeronasograms (EVGs), which are the equivalent of the electro-olfactograms in the MOE, would show a similar configuration-dependent reduction in amplitudes. Also, for the MOE and the VNO the question remains how the loss of Ca^{2+}-activated Cl^{-} currents translates into neuronal properties, such as spiking rates and synaptic transmission. Further characterization could thus include Ca^{2+} imaging at the first synapses of OSNs in the accessory olfactory bulb. Also, we did not investigate behaviors known to be controlled by vomeronasal signaling such as aggression and mating in detail yet.

However, such experiments would be most informative if performed in a background that lacks any residual CaCC activity in the VNO. To this aim, it would be useful to generate double knock-outs of Ano2 and Ano1. Since constitutive knock-out of Ano1 entails with death within three weeks after birth (Rock et al., 2008) working with conditional Ano1 knock-out mice deleted specifically for olfactory neurons would be required. OMP-Cre mice that express Cre under the control of the promoter of the olfactory marker protein expressed in all mature neurons of the different olfactory subsystems would suit this purpose (Li et al., 2004). These mice would also provide a valuable tool for controlling the specificity of the Ano1 immunolabeling we observed. Double knock-outs of Ano1 and Ano2 in the VNO could be investigated with respect to their molecular physiology, as suggested above, or in terms of their behavior. Aggression is one behavior that is fundamentally disturbed when VNO function is impaired (Tirindelli et al., 2009). To separate which behaviors depend on the function of CaCCs in the VNO it would be most informative to work with double knock-outs of Ano1 and Ano2 in the absence of a functional main olfactory epithelium. In such a system differences between both genotypes might be more prominent because vomeronasal function cannot partly be overtaken by the MOE. A triple knock-out including Cnga2 which abolishes function of the MOE and SOM would provide such a mouse model. Yet, in this background, it might be difficult to choose behavioral aspects that are preserved in mice deleted for Cnga2 but are disturbed when VNO function is compromised. Also, the developmental problems due to anosmia might lead to inter-animal differences that could make it difficult to faithfully detect differences caused by deletion of Ano1 and Ano2.

4.10. Ano2 in the retina

We also characterized expression of Ano2 in the retina. In our knock-out–controlled immunostainings Ano2 localized to synaptic endings of photoreceptors in the outer plexiform layer confirming previously reported stainings (Stöhr et al., 2009). Like in the VNO, Ano1 was co-localized with Ano2 in the same structures and was not affected by the loss of Ano2. Even though a co-expression within photoreceptors seems probable, both channels could also be expressed on joining pre- and postsynaptic membranes which cannot be microscopically resolved. *In situ* hybridization for Ano1 and Ano2 would provide a definite answer to this question. Our Ano1 immunohistochemistry on the retina does not match with studies by Yang et al. (2008) that used a different antibody. Yet the broad Ano1 labeling they observed might suggest a general unspecific staining. A retina-specific knock-out of Ano1 would provide a suitable control for antibody specificity. The persistence of Ano1 in *Ano2*$^{-/-}$ retina could be interpreted in such that Ano2 and Ano1 are functionally independent and that a CaCC activity is left. However, similar to the VNO, it might also be that all Ca^{2+}-activated Cl^{-} currents are missing when *Ano2* is deleted. In preliminary tests with few *Ano2*$^{-/-}$ mice we did not detect any changes in electro-retinograms. However, an effect on vision might only be detectable in a double knock-out of Ano1 and Ano2 in which all Ca^{2+}-activated Cl^{-} currents are absent. Such a double knock-out could be generated by crossing *Ano2*$^{-/-}$ mice with retina-specific knock-outs of Ano1.

Interestingly, when the scaffolding protein MPP4, which is crucial to the organization of a presynaptic complex in the OPL of the retina, is disrupted in mice, Ano2 is lost from the synaptic endings of photoreceptors (Stöhr et al., 2009). Deletion of MPP4 additionally leads to the loss or mislocalization of PSD-95, Veli3 and PMCA from the OPL (Aartsen et al., 2006; Yang et al., 2007). Thus, the loss of Ano2 from the OPL might be an indirect effect of the loss of PSD-95 to which Ano2 binds via its PDZ-binding motif (Stöhr et al., 2009). While Aartsen et al. (2006) did not find changes in ERG measurements, Yang et al. (2007) reported slightly impaired night vision of *Mpp4*$^{-/-}$ mice. Our preliminary ERG measurements in which we did not find any changes comply with a minor role of Ano2 for vision. We tested in our mice if other proteins of this OPL complex such as PMCA and the Ano2 interactor PSD-95 might be affected by the loss of Ano2. We found that both proteins localized normally and assume that Ano2 does not have a major role in organizing this presynaptic complex.

4.11. Ano2 expression pattern

Since Ano2 is expressed in the sensory neurons of smell and vision we also looked for expression in the other sensory systems, namely the inner ear and the somatosensory system. In immunohistochemistry we were not able to detect expression of Ano2 in the auditory system with the protocols and antibodies tested. Yet, further optimization of the tissue preparation and staining procedure of this intricate structure as well as immunoblots might reveal Ano2 expression.

In the somatosensory system we examined Ano2 expression in DRGs by immunohistochemistry and immunoblots but did not detect Ano2 signals. DRG neurons, though, are well known to express CaCCs and maintain elevated intracellular Cl^{-} levels akin to OSNs. One could speculate that in analogy to expression in other sensory neurons Ano2 is most highly enriched in the primary sensory organs of DRGs or in synaptic connections to second-order neurons and thus might have escaped detection at the soma of DRGs. In addition to Ano2 also Ano1 might be expressed in DRG neurons. Ano2 and Ano1 have been detected by RT-PCR in DRGs (Boudes et al., 2009). Expression of Ano2 in DRGs was also reported in *in situ* hybridization of DRGs during mouse embryonic development, while in the same study Ano1 was not detected (Rock and Harfe, 2008). However, in a different study *in situ* hybridization indicated expression of Ano1 in DRGs during cephalic development (Gritli-Linde et al., 2009). Yang et al. (2008) found Ano1 in immunohistochemistry of DRGs, but the antibody broadly labeled all structures and stainings were not knock-out–controlled. More detailed analysis of Ano1 and Ano2 expression in DRGs might reveal the contribution of both channels to CaCC activity of DRGs.

We additionally found low levels of Ano2 in immunoblots of different regions of the central nervous system (CNS). Thus the channel might also be expressed in neuronal cell types that are not characterized by elevated Cl^- concentrations. Ano2 expression in brain had been previously detected by RT-PCR and in immunoblots (Stöhr et al., 2009; Rasche et al., 2010). While we confirm expression of Ano2 at the protein level, our data indicate much lower protein levels and expression restricted to specified areas of the brain. Also, our knock-out–controlled immunoblots find differing apparent molecular weight and banding pattern thus questioning the specificity of the previously reported Ano2 signals in brain. Our attempts to localize the Ano2 protein to specific areas or cell types of the CNS by immunohistochemistry were not successful. Given this restricted expression which was most prominent in brain stem and mid brain Ano2 might have specific roles in selected neuronal cell types. Since in photoreceptors and olfactory receptor cells Ano2 is highly enriched at places of sensory input and synaptic output, respectively, a similar localization at synaptic connections of neurons might occur in the CNS. Considering the known interaction of Ano2 with PSD-95 in the retina (Stöhr et al., 2009), in the CNS Ano2 might be postsynaptically located since here the scaffolding protein PSD-95 is found at postsynaptic membranes. Nevertheless, we cannot exclude that Ano2 is expressed in non-neuronal cell types of the CNS.

However, the overall expression pattern of Ano2 suggests exclusively neuronal expression with most prominent expression in sensory neurons. Even though one might interpret this as an indication for a common function the distinct functional activities postulated for Ca^{2+}-activated Cl^- currents of different neuronal tissues, such as depolarization in OSNs and DRGs and repolarization in taste cells, rather argue against this notion. Our *Ano2*$^{-/-}$ mouse model now allows for detailed functional characterization of the Ano2-mediated Ca^{2+}-activated Cl^- currents in different tissues.

4.12. Ano2 isoforms

One striking difference between the Ano2 protein in different tissues is its apparent molecular weight in immunoblots. In the chemosensory systems of olfaction Ano2 runs at higher apparent molecular weights than in retina and brain tissue. Ano2 bears four predicted N-glycosylation sites (see Figure 2). We found that the distinct running behavior of the olfactory Ano2 isoform is due to more extensive glycosylation in olfactory tissues than in eye. After deglycosylation, Ano2 from MOE and VNO runs at the same size as deglycosylated Ano2 from retina. More complex glycosylation in the olfactory system seems reasonable given that in olfactory cilia the extracellular part of Ano2 is in direct contact with the mucus and the external environment. Strong glycosylation might protect the protein from damage and adapt it to the glycan-rich environment of the mucus. In contrast to the chemosensory systems, in tissues such as retina and brain where neurons do not directly contact the external environment the less glycosylated isoform of Ano2 is predominant. Yet, in the brain we detected the highly glycosylated isoform of Ano2. Its expression was restricted to the olfactory bulb and presumably stems from Ano2 in OSNs axons and synaptic endings considering that in immunohistochemistry we found Ano2 exclusively in the olfactory nerve layer and in glomeruli.

The characteristic triplet banding pattern that persists after deglycosylation of Ano2 in immunoblots from different tissues suggests that Ano2 bears additional posttranslational modifications. Given that the difference in size is very small and that this triplet is also seen with heterologously expressed Ano2, it might rather represent posttranslational modifications, such as phosphorylation, than splice isoforms. Occurrence of differential posttranslational modifications in the distinct organs of the olfactory system is also suggested by the differences in antibody affinity we observed. While our antibodies generated against peptide C1 recognize the vomeronasal Ano2 isoform efficiently they do not or only faintly detect Ano2 in the MOE in immunohistochemistry. The same though less prominent effect is observed in immunoblotting. Given that the peptide does not span any exon boundaries and that skipping of the encoding exon 3 would result in a ~12 kDa shift (see below) this differential binding affinity is probably due to the presence of differing posttranslational modifications and not due to isoforms. The immunizing peptide is rich in serines (see Figure 7) and the ELM prediction algorithms for functional sites (Puntervoll et al., 2003) indicate several phosphorylation sites.

Splice isoforms of Ano2 have so far only been reported on the mRNA level (Stephan et al., 2009). They either lack the 109 amino acids–coding exon 3 or the very short exon 13 which codes for four amino acids. Isoforms that lack larger exons would have been readily detected by their size difference in our immunoblots as observed with the heterologously expressed 104 amino acid–isoform of Ano2. We conclude that the reported isoform lacking exon 3 is physiologically not predominant. Exon 13 is exclusively expressed in the retina and in analogy to Ano1 might mediate enhanced Ca^{2+} sensitivity (Xiao et al., 2011). Functionally, such enhanced Ca^{2+} sensitivity in the retina seems reasonable given that Ca^{2+} levels in synaptic endings of photoreceptors might be more narrowly controlled than in the intricate structure of the cilia where intracellular Ca^{2+} is predicted to rapidly achieve high levels during transduction (Lindemann, 2001). Yet, a four amino acid difference cannot be resolved in western blots and we do not know if these isoforms exist on the protein level.

4.13. Ano2 interactors and modulators

Ano2 is likely to form the major subunit of the olfactory CaCC. This is supported by the lack of any residual CaCC activity in *Ano2*$^{-/-}$ OSNs and the very similar current properties of native and heterologously expressed Ano2. However, additional subunits might exist. Anoctamins presumably function as dimers (Sheridan et al., 2011; Fallah et al., 2011) and Ano2 might form heterodimers with other Anoctamins akin to what is known for CLCs (Jentsch, 2008). Given that in the MOE none of the other Anoctamins expressed is present at levels similar to Ano2 or is affected by its deletion, such a heterodimerization seems unlikely here. However dimer formation with Ano1 might occur when both channels are co-expressed in the same cell, as it could be the case in the VNO and the retina. Provided that more thorough expression analysis confirms such co-expression, interaction studies and biophysical characterization of heterodimers could follow up to further investigate a possible functional interaction. In eye and brain, characterization of the cell type–specific expression of Ano2 together with other Anoctamins could reveal co-localization and potential functional interactions. Ano3 and Ano4, for example, are specifically and highly expressed in neuronal tissue (Schreiber et al., 2010).

Additional modulatory subunits important for Ano2's transport, stability or more detailed aspects of its biophysical properties might exist. For instance, for CNG channels as well as for different CLCs such modulatory or obligatory subunits have been reported and shown to be crucial for proper localization, protein stability and electrophysiological behavior (Bradley et al., 2005; Jentsch, 2008). An obvious candidate for such a modulatory subunit is Best2 which previously had been thought to represent the olfactory CaCC and which localizes specifically to olfactory cilia (Pifferi et al., 2006, 2009b). A general function of Best2 for localization and stability of the Ano1/Ano2 subfamily seems improbable given that Ano1 deletion did not affect Best2 expression levels in salivary gland (Romanenko et al., 2010). Yet, Best2 might interact exclusively with Ano2 or regulate biophysical properties. Even though expression of TMCs was found in only one (Sammeta et al., 2007) out of many expression screens for olfactory genes (Genter et al., 2003; Yu et al., 2005; Mayer et al., 2008; Klimmeck et al., 2008; Mayer et al., 2009; Stephan et al., 2009; Rasche et al., 2010), the predicted structural homology and its role in sensory processes such as hearing could make them interesting candidates for functional interaction.

Besides regulatory subunits, also interacting proteins, soluble factors and components of the channel's microenvironment might be involved in regulating localization and function of Ano2. Evidence for existence of such modulators comes from inside-out patches of the native and heterologously expressed Ano2 channel (Kleene and Gesteland, 1991a; Reisert et al., 2003, 2005; Pifferi et al., 2006, 2009b). In both cases a continuous run-down of the channel activity has been observed after excision indicating either the gradual loss of crucial soluble factors, such as interacting proteins, or the degradation of essential factors of the microenvironment, such as special lipids like, for instance, PIP_2. Measurements of native and heterologously expressed Ano2 showed that a direct regulation by CaM and dNTPs or negative feedback by prolonged exposure to Ca^{2+} can been excluded (Kleene and Gesteland, 1991a; Reisert et al., 2003). A similar run-down of currents in excised patches has also been described for Ano1 implicating that both channels might be regulated by similar factors. So far PSD-95 is the only protein reported to directly interact with Ano2 (Stöhr et al., 2009). Upon deletion of the scaffolding protein MPP-4, PSD-95 and the Ano2 channel are lost from their native localization in the OPL of the retina indicating a crucial role of PSD-95 in keeping Ano2 at the presynaptic membrane. In other tissues PSD-95 or other PDZ domain–harboring proteins might be similarly involved in anchoring Ano2 to its specific membrane localization. It would be interesting to screen OSN expression data for proteins with PDZ domains that might interact with Ano2 and anchor it to the ciliary membrane. Our own preliminary experiments did not detect PSD-95 in the olfactory system though.

4.14. A functional role of Ano2 in humans?

The lack of phenotype in mice is in agreement to what is known from humans. In a severe form of von Willebrand disease a large genomic deletion leads to the disease-causing loss of von Willebrand factor together with the N-terminal part of Ano2 (Schneppenheim et al., 2007). However, there are no reports mentioning olfactory problems in these patients, except one recent personal communication from a widow of a deceased patient (Stephan et al., 2009). Given that only 0.05% of all reported anosmia is due to genetic defects and most of olfactory disorders are due to physical damage to the olfactory system (Gásdal Karstensen and Tommerup, 2011) it seems improbable that the anosmia reported in this patient is due to the partial Ano2 deletion. This notion is further supported by a study that could not find mutations in any of the main olfactory signal transduction components in different families with isolated congenital anosmia (Feldmesser et al., 2007). The authors concluded that mutations in olfactory signaling genes are not a major cause for congenital anosmia in humans. In a recent genome-wide association study a single nucleotide polymorphism in Ano2 was found to be associated with panic disorder (Otowa et al., 2009). The results of that study await independent confirmation, yet the expression of Ano2 in specific brain areas would fit a functional association with such a psychological disorder.

5. MATERIAL AND METHODS

5.1. Material

5.1.1. Mouse strains

PyRAT name*	Official nomenclature	Description and reference
Tm16b C7	B6;129-Tmem16b^{tm3Bil} (B6;129-Ano2$^{\mathrm{tm1.1Tjj}}$)	knock-out of *Ano2/Tmem16b*, generated from ES cell clone C7
Tm16b F2	B6;129-Tmem16b^{tm1Bil}	knock-out of *Ano2/Tmem16b*, generated from ES cell clone F2
Tm16b-lox C7	B6;129-Tmem16b^{tm4Bil} (B6;129-Ano2$^{\mathrm{tm1.2Tjj}}$)	floxed *Ano2/Tmem16b*, generated from ES cell clone C7
Tm16b-lox F2	B6;129-Tmem16b^{tm6Bil} (B6;129-Ano2$^{\mathrm{tm1.3Tjj}}$)	floxed *Ano2/Tmem16b*, generated from ES cell clone F2
Cre-del/Bl6	B6.C-Tg(CMV-cre)1Cgn	transgenic mouse with X-chromosomal CMV promoter-driven Cre expression; ubiquitous germline deletion (Schwenk et al., 1995; Jaxmice 006054)
Flp-del/Bl6	B6.129S4-*Gt(ROSA)26Sor*$^{tm1(FLP1)Dym}$	knock-in of FLPe in *Rosa26* locus; ubiquitous germline deletion (Farley et al., 2000; Jaxmice 009086)
P2-IRES-tauLacZ	B6;129P2-Olfr17^{tm1Mom}/Mom	knock-in; co-expression of the P2 odorant receptor with tau-LacZ fusion protein; for visualization of P2$^+$ OSNs (Mombaerts et al., 1996; Jaxmice 006595)
M72-IRES-tauLacZ	B6;129P2-*Olfr160*^{tm4Mom}/Mom	knock-in; co-expression of the M72 odorant receptor with tau-LacZ fusion protein; for visualization of M72$^+$ OSNs (Zheng et al., 2000; Jaxmice 006596)
Tm16b-P2lacZ	B6;129P2-Olfr17^{tm1Mom}/Mom x B6;129-Tmem16b$^{\mathrm{tm3Bil}}$	crossing of strains Tm16b C7 and P2-IRES-tauLacZ
Tm16b-M72lacZ	B6;129P2-*Olfr160*^{tm4Mom}/MomJ x B6;129-Tmem16b$^{\mathrm{tm3Bil}}$	crossing of strains Tm16b C7 and M72-IRES-tauLacZ
Cnga2	B6;129P2-*Cnga2*^{tm1Mom}/Mom	knock-out of *Cnga2* (X-chromosomal), hemizygous male and homozygous females are anosmic (Zheng et al., 2000; Jaxmice 006644)

* Working name in internal PyRAT animal tracking system

Mouse strains Cnga2, P2-IRES-tauLacZ and M72-IRES-tauLacZ were generously provided by Peter Mombaerts (MPI Biophysics, Frankfurt).

5.1.2. Bacteria strains

E. coli **strain**	Genotype	Application
XL1-Blue	*recA1 endA1 gyrA96 thi-1 hsdR17 supE44 relA1 lac [F´ proAB lacIqZΔM15* Tn*10 (Tet^r)]*	standard cloning
DB3.1	*F$^-$ gyrA462 endA Δ (sr1-recA) mcrB mrr hsdS20 (rB$^-$ mB$^-$) supE44 ara14 galK2 lacY1 proA2 rpsL20(Str^R) xyl5 λ$^-$ leu mtl1*	*ccd*B resistant; propagation of *ccd*B expressing plasmids for Gateway cloning
GM2163	*F$^-$ ara-14 leuB6 fhuA31 lacY1 tsx78 glnV44 galK2 galT22 mcrA dcm$^-$6 hisG4 rfbD1 rpsL136 dam13::*Tn9 *xylA5 mtl-1 thi-1 mcrB1 hsdR2*	*dam* and *dcm* deficient; generation of DNA for cloning with dam/dcm-sensitive restriction enzyme

E. coli **strain**	**Genotype**	**Application**
SURE	*e14⁻(McrA⁻) Δ(mcrCB-hsdSMR-mrr)171 endA1 gyrA96 thi-1 supE44 relA1 lac recB recJ sbcC umuC::Tn5 (Kan^r) uvrC [F´ proAB lacIqZΔM15* Tn*10 (Tet^r)]*	cloning of unstable DNA, increased stability for inverted repeats and Z-DNA

5.1.3. Plasmids

Plasmid name	**No.#**	**Insert**	**Vector backbone**	**Description**
pCMV-SPORT6-Tm16b	3920	mouse *Ano2/Tmem16b* (BC033409.1*)	pCMV-SPORT6	mammalian expression; 913 aa ORF
pDONR211	4078	*ccd*B resistance	–	Gateway cloning of pENTR vectors
pFROG_mTm16b	3951	mouse *Ano2/Tmem16b* (BC033409.1*)	pFROG3_rfA (3943#)	oocyte and mammalian expression; 913 aa ORF
GFP-mTm16b	4080	mouse *Ano2/Tmem16b* (BC033409.1*)	pcDNA3.1_EGFP-rfA (3869#)	mammalian expression with N-terminal GFP-tag; 1166 aa ORF
mTm16b-GFP	4088	mouse *Ano2/Tmem16b* (BC033409.1*)	pcDNA3.1_rfA-EGFP (3870#)	mammalian expression with C-terminal GFP-tag; 1167 aa ORF
pFROG_hTM16B	3945	human *ANO2/TMEM16B* (BC152768.1*)	pFROG3_rfA (3943#)	oocyte and mammalian expression; 999 aa ORF
pFROG_hTM16A	3944	human *ANO1*/*TMEM16A* (AL833582.1*)	pFROG3_rfA (3943#)	oocyte and mammalian expression; 986 aa ORF
pGEM_SP3	4094	genomic part of *Ano2*	pGEM-T Easy (Promega)	*Not*I excisable *Ano2* probe for Southern blot analysis (see Appendix)
pBSSK-3lox	3545	Neomycin resistance cassette	pBluescript-SK	Neomycin resistance cassette for ES cell selection, flanked by FRT sites and one additional loxP site
pKO901_ClC-5lox-targ	3359	genetically modified genomic part of *Clcn5*	pKO901	targeting vector for conditional knock-out of *Clcn5*
pKO_Tm16blox_targ	4092	genetically modified genomic part of *Ano2*	pKO901	targeting vector for conditional knock-out of *Ano2/Tmem16b* (see Appendix)

Number of plasmid in internal plasmid database of the Jentsch laboratory
* GenBank accession number
aa, amino acids; ORF, open reading frame

5.1.4. Primary Antibodies

For details on properties of the Ano2 antibodies listed compare Table 3. The last number in the name indicates the different animals in which the antibodies were produced. Ano2 antibodies from animals not included in Table 3 were positive for Ano2 in MOE and eye, yet gave comparably low signal or/and high background.

No.#	Antibody short name	Target protein	Antigen	Species, clonality	Supplier, article number	Dilution
977	rbAno2_N3-1	Ano2/ Tmem16b	NGETGKERHG GGPGDVELG	rabbit polyclonal	Pineda Antikörper-Service*	WB 1:200 IHC 1:200
1004	rbAno2_N3-2	Ano2/ Tmem16b	NGETGKERHG GGPGDVELG	rabbit polyclonal	Pineda Antikörper-Service*	WB 1:200 IHC 1:200
1005	rbAno2_N3-3	Ano2/ Tmem16b)	NGETGKERHG GGPGDVELG	rabbit polyclonal	Pineda Antikörper-Service*	WB 1:1000 IHC 1:1000
974	rbAno2_N2-1	Ano2/ Tmem16b	LKEEHEKVKLA DEPTQRSQ	rabbit polyclonal	Pineda Antikörper-Service*	WB 1:200 IHC 1:200
975	rbAno2_N2-2	Ano2/ Tmem16b	LKEEHEKVKLA DEPTQRSQ	rabbit polyclonal	Pineda Antikörper-Service*	WB 1:1000 IHC 1:200
976	rbAno2_N2-3	Ano2/ Tmem16b)	LKEEHEKVKLA DEPTQRSQ	rabbit polyclonal	Pineda Antikörper-Service*	WB 1:200 IHC 1:200
971	rbAno2_C1-1	Ano2/ Tmem16b	GDRSRRSRAA SSAPSGRSQP	rabbit polyclonal	Pineda Antikörper-Service*	WB 1:200 IHC 1:200
972	rbAno2_C1-2	Ano2/ Tmem16b	GDRSRRSRAA SSAPSGRSQP	rabbit polyclonal	Pineda Antikörper-Service*	WB 1:200 IHC 1:200
973	rbAno2_C1-4	Ano2/ Tmem16b)	GDRSRRSRAA SSAPSGRSQP	rabbit polyclonal	Pineda Antikörper-Service*	WB 1:200 IHC 1:200
1031	gpAno2_C1-1	Ano2/ Tmem16b	GDRSRRSRAA SSAPSGRSQP	guinea-pig polyclonal	Pineda Antikörper-Service*	WB 1:200 IHC 1:200
1032	gpAno2_C1-3	Ano2/ Tmem16b	GDRSRRSRAA SSAPSGRSQP	guinea-pig polyclonal	Pineda Antikörper-Service*	WB 1:200 IHC 1:200
970	TMEM16A	ANO1/ TMEM16A	peptide within aa 100–450 of human TMEM16A	rabbit polyclonal	ab53212, Abcam	WB 1:250 IHC 1:100
1036	OMP	Olfactory marker protein	purified rat OMP	goat polyclonal	544-10001, Wako	WB 1:1000
1035	C-20	Adenylate cyclase III	C-terminal peptide	rabbit polyclonal	sc-588, Santa Cruz	WB 1:2000 IHC 1:2000
1034	CNG-2/M-20	Cnga2	C-terminal peptide	goat polyclonal	sc-13700, Santa Cruz	WB 1:100 IHC 1:50
1000	AcTub	γ-acetylated α-tubulin	N-terminal epitope	mouse monoclonal clone 6-11B-1,	T7451, Sigma-Aldrich	IHC 1:1000
983	Ezrin	Ezrin	aa 362-585 of human ezrin	mouse monoclonal, clone 3C12	GTX24069, GeneTex	IHC 1:250
831	TH	Tyrosine hydroxylase	purified rat tyrosine hydroxylase	mouse monoclonal, clone 2/40/15	MAB5280, Chemicon	WB 1:5000 IHC 1:1000
171	PMCA	Plasma membrane Ca^{2+}-ATPase	purified human erythrocyte	mouse monoclonal, clone 5F10	MA3-914, Affinity BioReagents	IHC 1:500
1027	PSD-95	PSD-95	purified rat PSD-95	monoclonal mouse, clone 7E3-1B8	MA1-046, ThermoScientific	IHC 1:250
83	α-tubulin	α-tubulin	C-terminal epitope	mouse monoclonal, clone B-5-1-2	T5168, Sigma-Aldrich	WB 1:2000

No.[#]	Antibody short name	Target protein	Antigen	Species, clonality	Supplier, article number	Dilution
913	β-actin	β-actin	DDDIAALVIDN GSGK	mouse monoclonal, clone AC-74	A2228, Sigma-Aldrich	WB 1:1000
–	AP-2α	adaptin α	aa 38-215 of mouse AP-2α	mouse monoclonal	610501, BD Biosciences	WB 1:250

[#] Number of antibody in internal antibody database of the Jentsch laboratory
* Antibodies were affinity-purified from sera supplied by Pineda Antikörper-Service
WB, Western blotting; IHC, immunohistochemistry; aa, amino acids

5.1.5. Chemicals and solutions

All chemicals were purchased from Sigma, Fluka or Roth, if not otherwise stated. Phosphate-buffered saline (PBS), Tris-buffered saline (TBS) and Ringer's solution were prepared as described in Sambrook and Russell (2001).

5.2. Standard molecular biology techniques and reagents

Molecular biology procedures followed protocols in Sambrook and Russell (2001). We used electrocompetent *E. coli* for transformation with a Gene Pulser II electroporation system (Bio-Rad). Bacteria were grown in lysogeny broth medium and on lysogeny broth plates with the appropriate antibiotics.

For PCR cloning we used Phusion (Finnzymes) or OptiTaq (Roboklon) DNA polymerase. Isolation of plasmid DNA from *E. coli* was done with QIAGEN Plasmid Mini or Midi Kits (Qiagen). Restriction enzymes were purchased from Fermentas or New England Biolabs. DNA from enzymatic reactions was purified with the illustra GFX DNA Purification Kit (GE Healthcare). TA cloning was done with the pGEM-T Easy Kit (Promega) and positive clones selected by β-galactosidase screening. In Gateway cloning procedures we used the pDONR221 vector for generation of entry vectors and Gateway BP or LR Clonase II Mix (Invitrogen). Positive clones were identified by restriction digest or colony PCR and cloned plasmids were completely sequenced before use. DNA was stored in water, TE buffer (20 mM Tris (pH 8.0), 1 mM EDTA) or low TE buffer (20 mM Tris (pH 8.0), 0.1 mM EDTA). DNA concentrations were determined by measuring the absorbance at 260 nm with a Nanodrop ND-1000 spectrophotometer (PeqLab). All oligonucleotides were purchased from Biomers. Agarose gels were prepared with UltraPure agarose (Invitrogen) in TAE buffer (40 mM Tris, 40 mM acetic acid, 1 mM EDTA, pH 8.0) and samples for agarose gel electrophoresis were prepared with 6x DNA loading buffer (60 mM Tris-HCl (pH8.0), 60% glycerol, 60 mM EDTA, 0.4% Orange G). All primers for genomic targets were designed with NCBI Primer-BLAST which combines the BLAST algorithm and the Primer3 program (Rozen and Skaletsky, 2000) in order to avoid primer pairs that can cause amplification of targets other than the input template primers.

5.3. Standard biochemistry techniques and reagents

Preparation of lysates was done at 4°C and protein concentrations were determined with the BCA Protein Assay Kit (Pierce) using 20-µl samples and the microplate procedure. Albumin standards were prepared from 2.0 mg/ml stock ampules (Pierce) with water as diluent. Protein samples were denatured and loaded in 1x reducing sample buffer (50 mM Tris-HCl (pH 6.8), 2% SDS, 10% glycerol, 0.2% bromophenol blue, 100 mM DTT). Electrophoresis of 6%, 8% or 12% SDS-polyacrylamide gels was done according to the instructions of the Mini-PROTEAN 3 gel chamber system (Bio-Rad) using the prestained PageRuler Plus (Fermentas) as molecular weight marker. For immunoblots we used tank blotting with either the Mini Trans-Blot Electrophoretic Transfer Cell or the Criterion Blotter system (Bio-Rad) and transfer buffer without methanol (25 mM Tris, 192 mM glycine). Proteins were blotted on polyvinylidene difluoride membranes and protein transfer was controlled by staining with Ponceau S (0.2% Ponceau S, 3% acetic acid). Blocking and antibody incubation were done in PBS supplemented with 0.05% Tween-20 and 5% dry milk powder. Primary antibodies were incubated overnight at 4°C. The wash buffer was PBS with 0.05% Tween-20. Secondary antibodies were coupled to horseradish peroxidase (Chemicon) and signals were visualized by chemiluminescence (home-made ECL and SuperSignal West Pico/Femto, Pierce). Documentation was done with a Chemi-Smart 5000 CCD camera system (PeqLab) and the ChemiCapt 5000 software.

5.4. Standard cell culture techniques and reagents

Mammalian cell tissue culture followed standard procedures (Bonifacino, 2011). Cells were cultured on tissue culture dishes (TPP Techno Plastic products; Greiner Bio-One) at 37°C under a humidified atmosphere with 5% CO_2. Cell culture media and reagents (DMEM cell culture medium, 100x Pen/Strep, fetal calf serum, Dulbecco's PBS, 0.05% Trypsin/EDTA, cell culture grade dimethyl sulfoxide, OPTIMEM) were purchased from Invitrogen or PAN Biotech. Human embryonic kidney 293 cells were transfected during exponential growth with polyethylenimine (1 µg/µl in ultrapure water, pH 7.0) using standard transfection protocols (Bonifacino, 2011).

5.5. Mouse husbandry

Mice were kept in a temperature and humidity-controlled specific pathogen free animal facility with a 12 h light/dark cycle and free access to food and water. All animal care and procedures were in accordance with the German animal protection laws. Behavioral testing was done during the daytime and followed protocols reviewed and approved by the Berlin authorities.

5.6. Mouse genotyping

For routine genotyping genomic DNA was isolated from tail biopsies according to the HotSHOT protocol (Truett et al., 2000). 25-µl PCR reactions were set with 0.1–5 µl of HotSHOT-prepared DNA, 0.5 µM primer each, 0.2 µM dNTPs and 0.025 U of Taq (Invitrogen) or OptiTaq (Roboklon) DNA polymerase according to the manufacturer's instructions. Initial denaturation was done for 5 min at 94℃. Denaturation (94℃) and annealing steps during amplification cycles were 30 s. Details on primers and PCR protocols for genotyping of the different mouse strains are given in the table below. The genomic position of the Ano2 genotyping primers are depicted in Figure 8.

Mouse strain	No.[#]	Primer sequence (5'→3')	PCR protocol	PCR product length [bp]	
Tm16b	7780 8133	GGACACCCCGTACTTGAAGA AGCACAATGCAGACCAAGTT	T_a: 60℃, t_e: 40 s , $MgCl_2$: 2.0 mM, DMSO: 3%, cycles: 38	163 1051	knock-out allele wild-type allele
Tm16b-lox	7780 7781	GGACACCCCGTACTTGAAGA TCATCCCAGAGGTATGAGCA	T_a: 55℃, t_e: 30 s , $MgCl_2$: 1.5 mM, cycles: 38	211 177	floxed allele wild-type allele
Cre-del/Bl6	693 695	GGCCAGCTAAACATGCTTCATCGTC CTTTAACCCTGATCCTGGCAATTTCG	T_a: 64℃, t_e: 30 s , $MgCl_2$: 2.0 mM, cycles: 38	~250	Cre allele
Flp-del/Bl6	6821 6822	CACTGATATTGTAAGTAGTTTGC CTAGTGCGAAGTAGTGATCAGG	T_a: 58℃, t_e: 30 s , $MgCl_2$: 2.0 mM, cycles: 45	~700	FLPe allele
Cnga2	9167 9169	CAGTGCTCCCCATTAGTCACT CAAGTTCTAATTCCATCAGAAG	T_a: 55℃, t_e: 30 s , $MgCl_2$: 3.0 mM, cycles: 42	300	knock-out allele
	9167 9168	CAGTGCTCCCCATTAGTCACT AATGAGTGGGTAGAACCTAG	T_a: 60℃, t_e: 30 s , $MgCl_2$: 2.0 mM, cycles: 35	838	wild-type allele
M72-IRES-tauLacZ	8214 8218 8219	GCAGCTGTGGGCTTGTTCTATGGATCC CAGTAATAAGACCACAAATGCCT TGGAGCCCGTCAGTATCGGC	T_a: 60℃, t_e: 30 s , $MgCl_2$: 2.0 mM, cycles: 35	420 475	P2-IRES-tauLacZ allele wild-type allele
P2-IRES-tauLacZ	8221 8219	AGCCACTTGGAGAATTCATTG TGGAGCCCGTCAGTATCGGC	T_a: 60℃, t_e: 30 s , $MgCl_2$: 2.0 mM, cycles: 35	220	M72-IRES-tauLacZ allele
	8221 8220	AGCCACTTGGAGAATTCATTG ACATACTTCCGGCCACGCTCA	T_a: 60℃, t_e: 30 s , $MgCl_2$: 2.0 mM, cycles: 35	240	wild-type allele

[#] Number of primer in internal oligo database of the Jentsch laboratory
T_a, annealing temperature; t_e, elongation time

5.7. *Ano2* sequencing in mice

We sequenced the part of the *Ano2* gene sequence that codes for the epitope that is recognized by Ano2 antibodies generated against peptide N3 in order to reveal nucleotide polymorphisms between mice from the R1 ES cell background (129X1/SvJ x 129S1) and from the C57BL/6 background. High-quality genomic DNA was isolated from R1 ES cells and from tail biopsies of *Ano2*$^{+/+}$, *Ano2*$^{lox/+}$ and *Ano2*$^{lox/lox}$ mice. A 927-bp fragment spanning exon 3 was amplified by PCR using Phusion polymerase (Finnzymes) and the primer pair 5'-CCGCTCGCAGGTGCAAATGC-3' (9762) and 5'-GCCAACCACCAGGGCCCATC-3' (9760). The PCR product was gel-purified and sequenced using the amplification primers and the more internal primers 5'-GCTCCAGCCCAGCAGCCATCCGGAAG-3' (9757) and 5'-GCTCCAGCCCAGCAGCCATC-3' (9759). The numbers in parentheses give the number of the primers in the internal Jentsch laboratory oligo database.

5.8. Generation of *Ano2*$^{-/-}$ and *Ano2*$^{lox/lox}$ mice

5.8.1. *Ano2* targeting strategy

For disruption of Ano2 we flanked exon 12 with loxP sites and additionally inserted a FRT-flanked neomycin selection cassette between exon 12 and the second loxP site. We used a vector backbone with a diphtheria toxin A cassette for negative selection. Subsequent deletion of exon 12 eliminates a large portion of the first extracellular loop and part of the second predicted transmembrane domain of the Ano2 protein. Splicing from exon 11 to exon 13 results in a frameshift that adds 36 foreign amino acids to the protein after the first transmembrane domain.

5.8.2. Cloning of the *Ano2* targeting vector

An 11 kb genomic region of *Ano2* spanning exon 12 and 13 was cloned from R1 ES cells by PCR amplification with Phusion polymerase (Finnzymes) in three overlapping fragments. The resulting PCR products (fragment-1, fragment-2, fragment-3, see Figure 27) were A-tailed with Taq polymerase and TA-cloned into pGEM-T Easy (Promega). A DNA fragment harboring the first loxP site was generated by recombinant PCR and introduced into the fragment-1 vector via *Xba*I/*Spe*I restriction sites. The neomycin resistance cassette was cut from the pBSSK-3lox vector by *Apa*I/*Cla*I, blunted and subcloned into the fragment-2–harboring plasmid at the *Hpa*I restriction site. The modified fragment-2 was then subcloned into the modified fragment-1 vector via *Sal*I and *Bcl*I restriction sites using sequential and partial digestion of non-methylated DNA purified from *E. coli* strain GM2163. Fragment-3 was introduced into the resulting construct using *Kpn*I and *Sal*I. The complete targeting region was then subcloned from the pGEM-T Easy vector backbone via *Not*I into the pKO Scrambler plasmid 901 (Lexicon Genetics) containing a diphtheria toxin A cassette. It was generated via *Not*I digest from pKO901_ClC-5lox-targ. This resulted in the final targeting vector pKO_Tm16blox_targ (Figure 27). Propagation of plasmids was mostly done in SURE *E. coli* cells grown at 32℃ as other strains and conditions would not allow for sufficient amounts of DNA and result in instability of the plasmid. The final targeting vector was completely sequenced. We found the genomic Ano2 sequence we cloned to be in good agreement with the publically available genomic sequence of C57BL/6 mice. However, given that we cloned from R1 ES cells that have a Svj background we frequently found single nucleotide polymorphisms as well as insertions and deletions of several base pairs in intronic regions. The *Ano2* coding region did not differ.

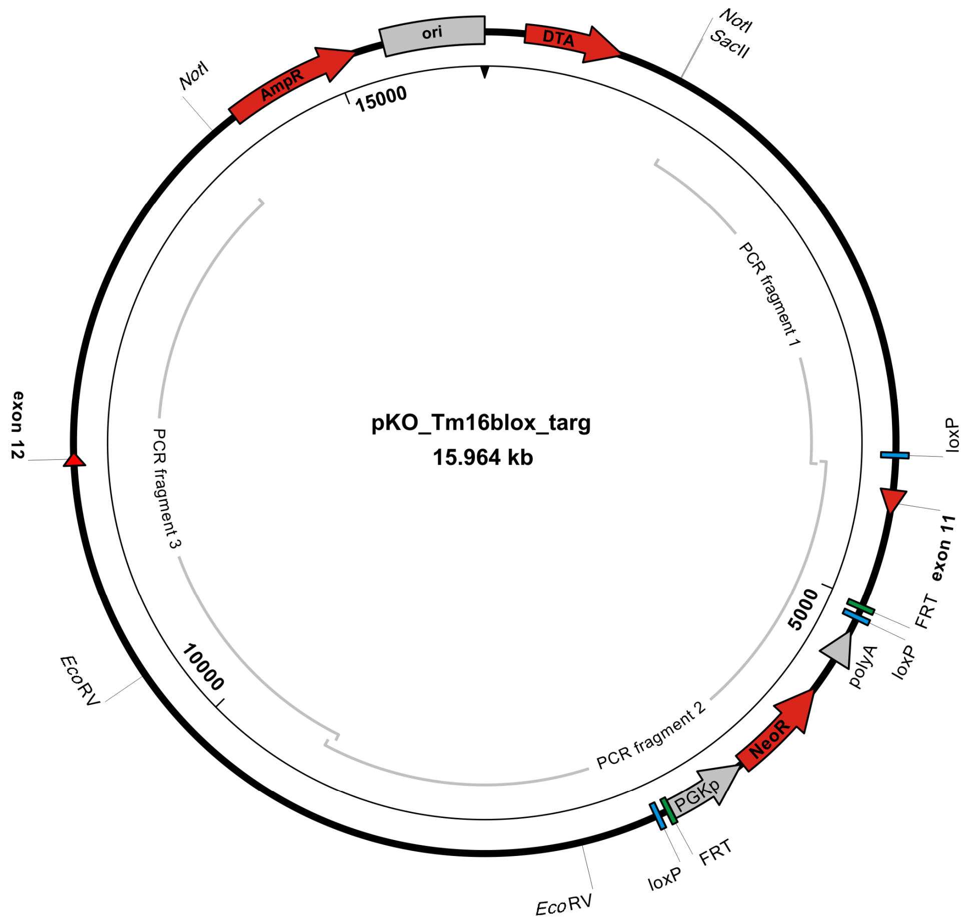

Figure 27 | Ano2_Tm16blox_targ vector map.
The different PCR fragments that were cloned from genomic DNA are indicated as are the elements of the neomycin resistance cassette (NeoR) and the FRT and loxP sites that were introduced. PGKp, phosphoglycerate kinase promoter; poly A, poly A tail.

5.8.3. Mouse ES cell culture and feeder cells

R1 ES cells (Nagy et al., 1993) were used for generation of gene-targeted mice. ES cells were grown on a confluent layer of mitotically inactivated mouse embryonic fibroblasts (feeder cells). All procedures with ES cells used ES cell-qualified fetal calf serum (FCS) from PAN Biotech. The ES cell medium contained: 15% FCS, DMEM (glutamine, 4.5 g/l glucose, 25 mM HEPES, pyridoxine), 1x sodium pyruvate, 1x non-essential amino acids, 1x Pen/Strep, 0.1 mM ß-mercaptoethanol (all from Invitrogen), 1x nucleoside mix (800 mg/l adenosine, 850 mg/l guanosine, 730 mg/l cytidine, 730 mg/l uridine, 240 mg/l thymidine, all from Sigma), and 1000 U/ml leukocyte inhibitory factor (ESGRO). ES cells were passaged every 2–4 days and the medium changed at least once a day. Feeder cells were generated from geneticin-resistant mice at P12 and aliquots frozen and stored in liquid nitrogen. For mitotic inactivation feeder cells were propagated for 7–10 days and treated with 10 µg/ml mitomycin C (Sigma) for 2 h. Inactivated feeder cells were frozen and seeded at $5x10^4$ cells/cm^2 12–24 h before use with ES cells. Feeder cells were always grown on plates coated with 0.1% gelatine (Sigma) and in DMEM with glutamax and 4.5 g/l glucose supplied with 10% FCS and antibiotics (100x Pen/Strep). Only upon culturing with ES cells the medium was changed to ES cell medium. All freezing was done with 15–18% FCS and 10% DMSO in the final freezing medium.

5.8.4. *Ano2* gene targeting by homologous recombination in mouse ES cells

For homologous recombination of the disrupted *Ano2* gene into the wild-type *Ano2* locus we electroporated the linearized targeting vector into ES cells. The targeting vector pKO_Tm16blox_targ was linearized with *Sac*II, purified by phenol/chloroform extraction and the precipitated DNA diluted in TE buffer to 1.0 µg/µl. ES cells for electroporation were trypsinized, triturated several times and counted. 1.1×10^7 cells in 800 µl PBS were mixed with 30 µg of the linearized vector, incubated for 5 min at room temperature and transferred to a 0.4 cm–gap electroporation cuvette. Electroporation was performed with a Bio-Rad GenePulser II at 240 V and 500 µFD. After 5 min at room temperature the cells were transferred to ES cell medium and evenly distributed on three 10-cm dishes plated with feeder cells. Drug selection was started 24 h after electroporation with 200 µg/ml geneticin (Invitrogen) and cells were kept under selection medium for eight days. Two 96-well plates of single ES cell colonies were picked after 12 days, trypsinized and plated on 96-well plates with feeder cells. When the plates reached confluency ES cells were split on two gelatinized plates and on two feeder plates. Cells from gelatinized plates were used for subsequent DNA isolation and feeder cell plates with ES cell colonies were frozen upon reaching the appropriate confluency for later recovery of positive clones.

5.8.5. Isolation of genomic DNA for Southern blot analysis

For isolation of genomic DNA from ES cells in 96-well plates the confluent cells were lysed overnight in 100 µl lysis buffer (10 mM Tris-HCl, pH 8.0, 10 mM EDTA, 0.2 % SDS, 100 mM NaCl, 0.2 mg/ml recombinant PCR grade Proteinase K (Roche)) per well at 55℃ in a humidified chamber. DNA was precipitated by adding 10 µl of 8 M LiCl und 100 µl isopropanol. After overnight incubation at room temperature the plates were centrifuged for 30 min, the supernatant discarded and the pellet washed with ice-cold 70% ethanol. After an additional centrifugation step the DNA pellet was dried and allowed to dissolve in low TE buffer at 55℃ overnight in a humidified chamber. F or isolation from higher numbers of cells or from mouse tail biopsies the protocol was scaled up and precipitated DNA was pelleted by centrifugation at 15,000 g for 30 min at 4℃. Af ter washing with ethanol the centrifugation step was repeated for 10 min, the pellet air-dried and dissolved in low TE buffer.

5.8.6. Southern blotting

The 775-bp Southern probe was cloned from R1 ES cells by PCR amplification with Phusion polymerase (Finnzymes) and the following primers: 5'-TGTGGGTTGAGCAGT ATGGA-3' (7571), 5'-AGGAACATCATATACTCCCTG-3' (7576). It was located upstream of the targeting region as depicted in Figure 8.

*Eco*RV digestion of genomic DNA for Southern blot analysis was done overnight at 37℃ by adding 4 µl of the enzyme (5 U/µl) and 6 µl of 10x EcoRV digestion buffer to 50 µl of isolated DNA (5–10 µg) in low TE buffer. For screening of ES cell clones in 96-well plates the reagents were added directly to the DNA in the wells. After addition of 12 µl 6x sample buffer the complete samples and a size marker that gets visualized during Southern blot development (MassRuler DNA Ladder High Range, Fermentas) were loaded on a 0.7% agarose gel. The gel was run at 50–95 V until satisfactory separation was reached. It was depurinized in 0.25 M HCl for 15 min and then incubated for 20 min in 0.4 M NaOH. The Southern blot stack was setup in 0.4 M NaOH and the DNA allowed to transfer on a Hybond-XL membrane (Amersham) overnight. DNA was cross-linked to the membrane with a UV Stratalinker 2400 (Stratagene) set to 10,000 µJ/cm^2. The membrane was neutralized in 2x SSC (300 mM NaCl, 0.3 M trisodium citrate) and pre-hybridized with Rapid-hyb hybridization buffer (Amersham) for 1–4 h at 65℃ i n a rolling incubator. The Southern probe for Ano2 was generated by *Not*I restriction digest from pGEM_SP3 (811 bp). The gel-purified probe was radioactively labeled with ^{32}P-dCTP and the Prime-It II random primer labeling kit (Stratagene) and purified on Quick Spin Columns (G-50 Sephadex Columns for Radiolabeled DNA Purification, Roche). After denaturation for 5 min at 95℃ it was directly added to the hybridization buffer in the incubation tube. The membrane was incubated overnight at 65℃ and then washed for two times 5 m in with wash buffer A (2x SSC, 0.1%

SDS) and for two times 20 min with wash buffer B (0.1x SSC, 0.5% SDS) at 65℃. The radioactive signal was detected with a Phosphorimager after overnight exposure.

5.8.7. Generation of *Ano2*$^{–/–}$ and *Ano2*$^{lox/lox}$ mouse lines from targeted ES cells

Positive ES cell clones were retrieved from the frozen 96-well plate and expanded to 6-well plates. From each clone three aliquots were frozen for later injection in blastocysts while another part was expanded for DNA isolation. The genotype of the ES cell clones was confirmed by Southern blot analysis. We chose the two positive ES cell clones C7 and F2 for blastocyst injection. Aliquots from these ES cells were thawed and cultured for 3–5 days. Shortly before injection the cells were trypsinized and singularized. After resuspension in ES cell medium most of the feeder cells were removed by allowing them to settle on a non-gelatinized tissue culture plate. Singularized ES cells from the supernatant were transmitted to the transgenic core facility of the MDC that resumed further experimental handling. ES cells were injected into blastocysts of C57BL/6 mice. Implantation into the uterus of foster mothers generated chimeras from both ES cell clones. Chimeras with a high contribution of ES cells were readily identifiable by their brown coat color that characterizes the 129X1/SvJ x 129S1 genetic background of the R1 ES cell line. Male chimeras were directly mated with Cre deleter mice (Schwenk et al., 1995) or FLPe-expressing mice (Farley et al., 2000) in a C57BL/6 background to generate the Ano2$^{–}$ or Ano2^{lox} allele, respectively. Resulting heterozygous animals (*Ano2*$^{+/–}$ or *Ano2*$^{+/lox}$) were bred to yield *Ano2*$^{–/–}$ or *Ano2*$^{lox/lox}$ mice. We got germ line transmission with both ES cell clones and established four independent mouse colonies, one conditional and one constitutive knock-out of *Ano2* for each clone. For our experiments we used mice from the F1 and F2 generation and littermates as control. These mice had a mixed C57BL/6 x 129/Svj background.

5.9. Generation of Ano2 antibodies

Polyclonal Ano2 antibodies were raised in rabbits and guinea pigs against the three Ano2-specific peptides shown in Figure 7 (Pineda Antikörper-Service, Berlin, Germany). For nomenclature and an overview of the different antibodies see Table 3 and chapter 5.1.4. Peptides were coupled via C- and N-terminally added cysteins, respectively, to keyhole limpet hemocyanine. Following the first immunization, animals were boosted seven times within 120–130 days. Antibodies were affinity-purified from final bleeds against the immunizing peptide coupled to a Sulfolink coupling resin (Pierce). Antibodies were allowed to bind overnight and columns were washed with high-salt TBS (TBS with 500 mM NaCl) followed by washing steps with TBS and 0.1x TBS. Antibodies were eluted with 100 mM glycine pH 3.0 and 200-µl fractions were collected. The pH of the eluates was set to pH 7.5–8.0 and protein containing fractions, as identified in Ponceau S–stained dot blots, were pooled. After addition of 0.1% BSA and 0.02% NaN_3 antibodies were aliquoted and shock-frozen in liquid nitrogen. Long-term storage was at –80℃.

5.10. Preparation of protein lysates and deglycosylation

For preparation of complete lysates from mouse tissues, organs were dissected, minced with scissors and sonicated in lysis buffer (10 mM HEPES (pH 7.4), 150 mM NaCl, 5 mM EDTA, 1x complete protease inhibitors, 1% SDS). Debris was sedimented by centrifugation at 10,000 g for 10 min and the supernatant used for assays. Cultured cells were pelleted and prepared accordingly. MOE and VNO samples were prepared from complete turbinates and whole VNO, respectively. For deglycosylation, samples were incubated for 15 min at 55℃ with 5% β-mercaptoethanol, diluted 1:5 into deglycosylation buffer (50 mM HEPES pH 7.4, 10 mM EDTA, 0.5% Nonidet P-40, 1x complete protease inhibitors) and incubated overnight at 37℃ with 1 U of N-Glycosidase F (Roche Diagnostics) per 100 µg of protein. Reactions were stopped by denaturing in 1x reducing sample buffer (50 mM Tris-HCl pH 6.8, 2% SDS, 10% glycerol, 0.2% bromophenol blue, 100 mM DTT).

5.11. Immunohistochemistry

Anesthetized mice were transcardially perfused with PBS followed by 4% paraformaldehyde in PBS and tissues were postfixed for 2 h (olfactory bulb) or overnight (nose, eye). Eyes from knock-out and wild-type mice were embedded side by side in TissueTek O.C.T. compound (Sakura) and 6-µm cryosections were cut. We prepared 10-µm sections from olfactory bulb. Noses were decalcified in 10% EDTA in PBS (pH 8.0) for 3–7 days, postfixed for 2 h and embedded in paraffin. 6-µm sections were cut from the nose. Sections from knock-out and wild-type nose and olfactory bulb, respectively, were mounted side by side on one glass slide. Paraffin sections were de-paraffinized with Roti-histol (Roth), rehydrated with a decreasing ethanol series and incubated for 30 min in TBS before staining. Cryosections were thawed and transferred to TBS buffer until staining. For epitope retrieval, sections were boiled for 5 min in 10 mM citrate buffer (pH 6.0) or Tris/EDTA buffer (10 mM Tris, 1 mM EDTA, pH 9.0). Sections were cooled by transfer to an access of TBS at room temperature. Blocking and antibody incubation were done with 3% BSA in TBS with 0.2% NP-40. After blocking for 1–3 h, the tissue was incubated overnight at 4℃ with the primary antibody in a humidified chamber. We incubated for 1 h at room temperature with secondary antibodies that were coupled to Alexa fluorophores (see table below) and counterstained nuclei with Hoechst 33258 (0.1 µg/ml). Slides were mounted with coverslips using Aqua-Poly/Mount Coverslipping Medium (PolySciences) and stored at 4℃. All pictures were taken with a Zeiss LSM 510 META laser scanning microscope using ZEN software (Zeiss) and a Plan-Apochromat 63x/1.40 Oil DIC M27 or EC Plan-Neofluar 10x/0.3

M27 objective. If not otherwise stated all images are confocal images. Image processing was done with ZEN software (Zeiss). Immunostainings were repeated in at least three independent experiments.

Antibody name	Invitrogen article number	Dilution
Alexa Fluor 488 goat anti-rabbit, highly cross-adsorbed	A11034	1:1000
Alexa Fluor 555 goat-anti-mouse, highly cross-adsorbed	A21424	1:1000
Alexa Fluor 488 goat anti-guinea pig, highly cross-adsorbed	A11073	1:1000
Alexa Fluor 555 goat anti-rabbit , highly cross-adsorbed	A21429	1:1000
Alexa Fluor 488 donkey anti-rabbit	A21206	1:1000
Alexa Fluor 555 donkey anti-goat	A21432	1:1000

5.12. Analysis of OSN axonal convergence

P2-IRES-tauLacZ and M72-IRES-tauLacZ mice were crossed with *Ano2*$^{+/–}$ mice to yield *Ano2*$^{–/–}$ and *Ano2*$^{+/+}$ littermates homozygous for these reporter lines. Mice at 5–24 weeks were anesthetized and transcardially perfused with PBS followed by 4% paraformaldehyde in PBS. The cranium was freed from its surrounding tissue and the brain with the olfactory bulb was carefully dissected. The tissue was washed three times with LacZ buffer A for 10 min and incubated in LacZ buffer B (0.1 M phosphate buffer (pH 7.4), 2 mM $MgCl_2$, 5 mM EGTA, 0.02% NP-40, 0.01% Na-deoxycholate) for at least 30 min. The buffer was changed to X-Gal staining solution (0.1 M phosphate buffer (pH 7.4), 2 mM $MgCl_2$, 5 mM potassium ferricyanide, 5 mM potassium ferrocyanide, 1 mg/ml X-Gal (5-bromo-4-chloro-indolyl-galactopyranoside), 0.2% NP-40, and 0.1% Na-deoxycholate) and upon reaching a satisfactory staining intensity the reaction was stopped by washing several times in PBS. Stained brains were stored in 4% paraformaldehyde at 4℃. To obtain sections from these whole-mount X-Gal–stained bulbs the brain was transferred to 30% sucrose and embedded in TissueTek O.C.T compound (Sakura). The complete bulb was cut in 20-µm sections and mounted onto glass slides. Sections were washed three times with LacZ buffer A and incubated for 20 min with LacZ buffer B before post-staining with X-Gal staining solution for 2 h. The reaction was finished by washing with PBS and the tissue counterstained with Neutral Red. Pictures from whole-mount stainings and bulb sections were taken with a Zeiss stereomicroscope 2000C and a Kappa DX-20 HC-FW camera system with Kappa ImageBase Control 2.7.2 software (Kappa opto-electronics).

5.13. Quantitative real-time PCR

Turbinates were dissected from *Ano2*$^{+/+}$ and *Ano2*$^{-/-}$ mice (three litter pairs, 25–27 weeks old) and the total RNA isolated using the RNeasy Mini Kit (Qiagen). For RNA isolation tissue was disrupted with a mortar and pestle in liquid nitrogen and homogenized with a syringe and needle. We subjected 1 µg of total RNA to amplification grade DNase I (Invitrogen) digestion and transcribed it into cDNA using random primers and Superscript II reverse transcriptase (Invitrogen). 20-µl PCR reactions were set up with the Power SYBR Green PCR Master Mix (Applied Biosystems) and run in triplicates. We used 0.2 µM primer each, 0.4 µl cDNA and a 40-s elongation step at 60°C. Amplification and melting curves were monitored using a StepOnePlus Real-Time PCR System and StepOne Software (Applied Biosystems). Samples lacking reverse transcriptase were run as negative controls. Comparison between *Ano2*$^{-/-}$ mice and wild-type littermates were performed according to the Pfaffl method (Pfaffl, 2001) using β-actin as internal control. Primers spanned introns or exon-exon boundaries and gave products of 100–200 bp length. All primer pairs used are given in the table below.

Gene	No.[#]	Primer sequence (5'→3')	PCR product	Remarks
β-actin	9494 9495	TGTGATGGTGGGAATGGGTCAGAA TGTGGTGCCAGATCTTCTCCATGT	140 bp	internal standard
Adenylate cyclase III	9427 9248	CGGCATCGAGTGTCTACGCTTC GCCAGCGCTCCTTGTCTGACTT	200 bp	MOE marker
Ano2_ex3-4	7749 7545	GATGTTGAACTTGGGCCACT CAAGAACTCTGCTTCCCTGG	186 bp	primer span intron between exon 3 and 4
Ano2_ex20-21	7544 7543	AGGCTGTCTCATGGAGCTGT TGCTCTGGACGTTTTGAGTG	174 bp	primer span intron between exon 20 and 21
Ano6	9403 9404	AAGAGGAACAGGCCCGGCCA AGAAGACGGCGCTCGCACAC	141 bp	–
Ano8	9387 9388	GCGACGCGGCTGGAAGACAG CGGCCAGTGGGAAGGCAGAG	198 bp	–
Ano10	9395 9396	AGCGGAAGTACTGTGCGAGGGT GCAAAGGCAGCTGCTAGCGG	199 bp	–
Nkcc1	9381 9382	CTGGTGGGCTGCGTTGCTCA GCGCTTGTGTGGAGGATCCCC	101 bp	–

[#] Number of primer in internal oligo database of the Jentsch laboratory

5.14. Electro-olfactogram recordings

The head was cut into two halves in the sagittal plane and the endoturbinates were exposed (Nickell et al., 2006; Cygnar et al., 2010). The lateral side of the head was immersed into 0.5% agarose gel with normal Ringer's solution.

In fluid-phased EOGs the turbinates were continuously superfused with normal Ringer's solution with or without 300 µM niflumic acid. The four-barreled application pipette had two channels for continuous flow of normal Ringer's solution, one channel for odorant-free vehicle and one for odorants. The last two channels were connected to a Picospritzer (Toohey). Pressure steps were applied for 200 ms, except for forskolin (2 s). Mixtures of odorants, single odorant or forskolin in aqueous solution containing 0.5% DMSO were used.

In the air-phase configuration, the application tube had a channel for continuous flow of humidified 95% O_2/5% CO_2. Another tube connected to a 15-ml bottle containing 2 ml of odorants or odorant-free vehicle, and a Picospritzer. Pressure steps of 200 ms were used to drive the air from the bottle to the turbinates. In both arrangements, EOGs were recorded in current clamp with an extracellular electrode filled with normal Ringer's solution placed on the middle of turbinate IIb or III. Signals were low-pass filtered at 1 kHz. EOG amplitudes from single turbinates were averaged from ten individual sweeps and subsequently averaged from several experiments. These measurements were performed by Balázs Pál.

5.15. Patch-clamp analysis

5.15.1. Tissue preparation for patch-clamping

Mice were killed at 6–8 weeks by decapitation. The MOE was prepared and embedded in 4% low melting agarose in normal Ringer's solution (140 mM NaCl, 5 mM KCl, 10 mM glucose, 1 mM sodium pyruvate, 10 mM HEPES (pH 7.4), 2 mM $CaCl_2$, 1 mM $MgCl_2$; osmolality, 321 mOsm/kg). A Leica VT1200S vibratome was used to cut 200-µm slices perpendicular to the surface. The soft tissue of the VNO was embedded in 4% low melting agarose and cut in 200-µm coronal slices (Shimazaki et al., 2006). Slices were kept in normal Ringer's solution bubbled with 95% O_2/ 5% CO_2. These preparations were done by Balázs Pál.

5.15.2. Patch-clamp measurements in tissue slices

Pipettes were pulled from borosilicate glass with a DMZ-Universal Puller (Zeitz Instruments). The pipette solution contained 140 mM CsCl, 4 mM HEPES (pH 7.2), 1 mM EGTA, 2 mM Mg-ATP. The free Ca^{2+} concentration was adjusted with $CaCl_2$ to 0 µM, 1.5 µM and 13 µM according to the Maxchelator program (http://maxchelator.stanford.edu/). OSNs from the MOE were patched at the cell body and sometimes at the dendritic knob, with similar results. VSNs were patch-clamped at the dendritic knob. Pipette resistances were ~5 MΩ and 8–10 MΩ when patching OSNs or VSN dendritic knobs, respectively. Recordings were performed in the whole-cell configuration at room temperature in normal Ringer's solution containing 10 mM tetraethylammonium chloride using an Axon CNS MultiClamp 700B amplifier, a Digidata 1322A interface, and pClamp 10 software (Molecular Devices). From a holding potential of 0 mV, voltage was clamped in 700 ms steps from –100 mV to

+100 mV, followed by 100 ms at –100 mV. Pipette solutions included 50 µM Alexa Fluor 488 (Invitrogen) to identify cell types. These measurements were performed by Balázs Pál.

5.15.3. Preparation of isolated OSNs

The MOE was transferred to a low-Ca^{2+} Ringer's solution (140 mM NaCl, 5 mM KCl, 10 mM glucose, 1 mM Na-pyruvate, 1 mM EDTA, 1 mM cysteine, 10 mM HEPES (pH 7.2)) at 4℃. After mincing, it was digested at room temp erature for 20 min with 0.2 mg/ml trypsin in low-Ca^{2+} Ringer's solution. The digestion was terminated with normal Ringer's solution containing 0.2 mg/ml BSA, 0.2 mg/ml leupeptin and 0.025 mg/ml DNase I. Following gentle trituration, cells were allowed to settle on poly-L-lysine–coated coverslips for 30–45 min at 4℃. These preparations were done by Balázs Pál.

5.15.4. Photorelease of caged Ca^{2+} and 8-Br-cAMP

We used [6,7-Bis(carboxymethoxy)coumarin-4-yl]methyl-8-bromoadenosine-3', 5'-cyclic monophosphate (BCMCM-caged 8-Br-cAMP), a generous gift from Volker Hagen, FMP Berlin, and DMNP-EDTA (Invitrogen). For uncaging 8-Br-cAMP, a UV flash lamp JML-C2 (Rapp OptoElektronik) was coupled to an inverted Zeiss Axiovert 200 microscope equipped with a 100x Fluar objective. Ca^{2+} was uncaged with a SP-20 UV flash lamp (Rapp OptoElektronik) coupled to an upright Olympus BX51WI microscope equipped with a 60x LUMPlanFL objective. Isolated OSNs were patched at room temperature in the whole-cell mode. For Ca^{2+} uncaging, the pipette solution contained 140 mM KCl, 2 mM MgATP, 0.3 mM Na_2-GTP, 10 mM HEPES (pH 7.4), 3.5 mM $CaCl_2$, and 5 mM DMNP-EDTA. For uncaging 8-Br-cAMP, the pipette solution contained 145 mM KCl, 4 mM $MgCl_2$, 1 mM MgATP, 0.1 mM Na_2-GTP, 10 mM HEPES (pH 7.4), 0.5 mM EGTA, and 0.1 mM BCMCM-caged 8-Br-cAMP. Settings were 200 V at 1 mF and 300 V at 3 mF for uncaging 8-Br-cAMP and Ca^{2+}, respectively. These measurements were performed by Balázs Pál and Pawel Fidzinski.

5.16. $Cl^–$-sensitive microelectrodes

$Cl^–$-selective electrodes were fabricated (Windmüller et al., 2005) from double-barreled theta-glass capillaries (Warner Instruments) with tip diameters of ~3 µm. Ion-selective barrels were silanized with methyltrichlorosilane in dichloromethane (Fluka/Sigma-Aldrich) and backfilled with "Chloride ionophores I – cocktail A" (Fluka/Sigma-Aldrich). Reference barrels contained 155 mM NaCl. To exclude artifacts by $Cl^–$ diffusion from reference barrels, we also filled them with 40 mM NaCl and 77 mM Na_2SO_4. No differences in measured $Cl^–$ concentrations were found. Measurements with either reference barrel solution were pooled. Double-barreled microelectrodes connected to a differential amplifier

(Windmüller et al., 2005) were lowered at a low angle onto the surface of freshly dissected turbinates. Cl^- concentrations were determined from calibration curves before and after measurements. Measurements were discarded when these calibrations differed by >20%. These measurements were performed by Balázs Pál.

5.17. Olfactometry

Behavioral assessment of odor detection and odor discrimination ability used a computer-controlled 8-channel liquid-dilution olfactometer (Knosys), as described (Slotnick and Restrepo, 2005). In this test paradigm, mice are trained on a go or no-go operant conditioning task in which licking on a water delivery tube upon presentation of an S+ stimulus (odor 1) is associated with a water reward, but not after presentation of an S– stimulus (odor 2 or diluent). Mice that are able to discriminate between stimuli readily stop to answer to the S– stimulus when subjected to successive trials of S+ and S– stimuli presented in random order. Response accuracy is monitored as a measure for odor discrimination and detection ability and represents the percentage of correct answers in a block of 20 trials.

Training programs used were BEGIN and D2 (Slotnick and Restrepo, 2005) with the following settings: 2.5 s stimulus presentation, 1 s final valve time, 4 s intertrial interval and 2 µl water reward. The criterion response for a correct answer was set to ≥ 6 licks in ten 0.2 s periods of the last 2 s of an odor presentation. Odors were diluted 1:20 into the airflow. Odorant were purchased from Sigma or Fluka in the highest purity available and dilutions were prepared freshly every day in 5 ml mineral oil. Before starting a session with a new odor or dilution, bottles were filled with the diluents only and tested with wild-type mice for 200 trials to make sure that no odors intrinsic to the diluents, bottles or tubing could account for discrimination ability. The odor was then directly added to the bottle in the S+ channel and sessions were run with the test animals.

Water-deprived *Ano2*$^{-/-}$ mice and control littermates were trained on the BEGIN program and on the D2 program with a simple odor discrimination task. For testing we used the D2 program. Mice (35–41 weeks old) were tested on 1% (–)-limonene versus 0.5% (–)/0.5% (+)-limonene (six males, two females) and on geraniol dilutions (eight males, four females) starting with the highest concentration. Trials were 200 or 400 (with geraniol dilutions of 10^{-6} and 10^{-7}) and response accuracy was calculated as mean of three consecutive blocks after reaching the criterion response of 90% or of the last three blocks in 400 trials, respectively. Mice at 14 weeks old (four males, two females) were used for 1% hexanal versus 1% octanal discrimination, and six males and four females (at 50 weeks old) were used for the 0.4/0.6% versus 0.6%/0.4% hexanal/octanal discrimination test. Three male *Cnga2*$^{-/y}$ mice (14–16 weeks old) were tested on 1% geraniol.

6. REFERENCES

Aartsen, W. M., Kantardzhieva, A., Klooster, J., van Rossum, A. G. S. H., van de Pavert, S. A., Versteeg, I., Cardozo, B. N., Tonagel, F., Beck, S. C., Tanimoto, N., et al. (2006). Mpp4 recruits Psd95 and Veli3 towards the photoreceptor synapse. Hum. Mol. Genet *15*, 1291–1302.

Adams, D. R. (1992). Fine structure of the vomeronasal and septal olfactory epithelia and of glandular structures. Microsc. Res. Tech *23*, 86–97.

André, S., Boukhaddaoui, H., Campo, B., Al-Jumaily, M., Mayeux, V., Greuet, D., Valmier, J., and Scamps, F. (2003). Axotomy-induced expression of calcium-activated chloride current in subpopulations of mouse dorsal root ganglion neurons. J. Neurophysiol. *90*, 3764–3773.

Antolin, S., Reisert, J., and Matthews, H. R. (2010). Olfactory response termination involves Ca2+-ATPase in vertebrate olfactory receptor neuron cilia. J. Gen. Physiol *135*, 367–378.

Arreola, J., Melvin, J. E., and Begenisich, T. (1998). Differences in regulation of Ca(2+)-activated Cl- channels in colonic and parotid secretory cells. Am. J. Physiol. *274*, C161–C166.

Bakalyar, H. A., and Reed, R. R. (1990). Identification of a specialized adenylyl cyclase that may mediate odorant detection. Science *250*, 1403–1406.

Baker, H., Cummings, D. M., Munger, S. D., Margolis, J. W., Franzen, L., Reed, R. R., and Margolis, F. L. (1999). Targeted deletion of a cyclic nucleotide-gated channel subunit (OCNC1): biochemical and morphological consequences in adult mice. J. Neurosci *19*, 9313–9321.

Baker, H., Morel, K., Stone, D. M., and Maruniak, J. A. (1993). Adult naris closure profoundly reduces tyrosine hydroxylase expression in mouse olfactory bulb. Brain Res *614*, 109–116.

Barnea, G., O'Donnell, S., Mancia, F., Sun, X., Nemes, A., Mendelsohn, M., and Axel, R. (2004). Odorant receptors on axon termini in the brain. Science *304*, 1468.

Belluscio, L., Gold, G. H., Nemes, A., and Axel, R. (1998). Mice deficient in G(olf) are anosmic. Neuron *20*, 69–81.

Bhandawat, V., Reisert, J., and Yau, K.-W. (2005). Elementary response of olfactory receptor neurons to odorants. Science *308*, 1931–1934.

Blaustein, M. P. (1988). Calcium transport and buffering in neurons. Trends Neurosci. *11*, 438–443.

Boccaccio, A., and Menini, A. (2007). Temporal development of cyclic nucleotide-gated and Ca2+ -activated Cl- currents in isolated mouse olfactory sensory neurons. J. Neurophysiol *98*, 153–160.

Bolduc, V., Marlow, G., Boycott, K. M., Saleki, K., Inoue, H., Kroon, J., Itakura, M., Robitaille, Y., Parent, L., Baas, F., et al. (2010). Recessive mutations in the putative calcium-activated chloride channel Anoctamin 5 cause proximal LGMD2L and distal MMD3 muscular dystrophies. Am. J. Hum. Genet *86*, 213–221.

Bonifacino, J. S. (2011). Current Protocols in Cell Biology (John Wiley & Sons).

Bönigk, W., Bradley, J., Müller, F., Sesti, F., Boekhoff, I., Ronnett, G. V., Kaupp, U. B., and Frings, S. (1999). The native rat olfactory cyclic nucleotide-gated channel is composed of three distinct subunits. J. Neurosci *19*, 5332–5347.

Boudes, M., Sar, C., Menigoz, A., Hilaire, C., Péquignot, M. O., Kozlenkov, A., Marmorstein, A., Carroll, P., Valmier, J., and Scamps, F. (2009). Best1 is a gene regulated by nerve injury and required for Ca2+-activated Cl- current expression in axotomized sensory neurons. J. Neurosci *29*, 10063–10071.

Bozza, T. C., and Kauer, J. S. (1998). Odorant response properties of convergent olfactory receptor neurons. J. Neurosci *18*, 4560–4569.

Bozza, T., Feinstein, P., Zheng, C., and Mombaerts, P. (2002). Odorant receptor expression defines functional units in the mouse olfactory system. J. Neurosci *22*, 3033–3043.

Bozza, T., McGann, J. P., Mombaerts, P., and Wachowiak, M. (2004). In vivo imaging of neuronal activity by targeted expression of a genetically encoded probe in the mouse. Neuron *42*, 9–21.

Bradley, J., Reisert, J., and Frings, S. (2005). Regulation of cyclic nucleotide-gated channels. Curr. Opin. Neurobiol *15*, 343–349.

Bradley, J., Reuter, D., and Frings, S. (2001). Facilitation of calmodulin-mediated odor adaptation by cAMP-gated channel subunits. Science *294*, 2176–2178.

Brechbühl, J., Klaey, M., and Broillet, M.-C. (2008). Grueneberg ganglion cells mediate alarm pheromone detection in mice. Science *321*, 1092–1095.

Bronshtein, A. A., and Leont'ev, V. G. (1972). [Sodium and potassium content in the mucus of the olfactory lining of vertebrates]. Zh. Evol. Biokhim. Fiziol *8*, 580–585.

Brunet, L. J., Gold, G. H., and Ngai, J. (1996). General anosmia caused by a targeted disruption of the mouse olfactory cyclic nucleotide-gated cation channel. Neuron *17*, 681–693.

Buiakova, O. I., Baker, H., Scott, J. W., Farbman, A., Kream, R., Grillo, M., Franzen, L., Richman, M., Davis, L. M., Abbondanzo, S., et al. (1996). Olfactory marker protein (OMP) gene deletion causes altered physiological activity of olfactory sensory neurons. Proc. Natl. Acad. Sci. U.S.A *93*, 9858–9863.

Caputo, A., Caci, E., Ferrera, L., Pedemonte, N., Barsanti, C., Sondo, E., Pfeffer, U., Ravazzolo, R., Zegarra-Moran, O., and Galietta, L. J. V. (2008). TMEM16A, a membrane protein associated with calcium-dependent chloride channel activity. Science *322*, 590–594.

Chamero, P., Katsoulidou, V., Hendrix, P., Bufe, B., Roberts, R., Matsunami, H., Abramowitz, J., Birnbaumer, L., Zufall, F., and Leinders-Zufall, T. (2011). G protein G{alpha}o is essential for vomeronasal function and aggressive behavior in mice. Proc. Natl. Acad. Sci. U.S.A *108*, 12898–12903.

Chesler, A. T., Zou, D.-J., Le Pichon, C. E., Peterlin, Z. A., Matthews, G. A., Pei, X., Miller, M. C., and Firestein, S. (2007). A G protein/cAMP signal cascade is required for axonal convergence into olfactory glomeruli. Proc. Natl. Acad. Sci. U.S.A *104*, 1039–1044.

Chiu, D., Nakamura, T., and Gold, G. H. (1988). Ionic composition of toad olfactory mucus measured with ion selective microelectrodes. In Chemical Senses, pp. 677–678.

Crumling, M. A. and Gold, G. H. Ion concentrations in the mucus covering the olfactory epithelium in rodents. Soc. Neurosci. Abstr. 24: 2099, 1998.

Cygnar, K. D., Stephan, A. B., and Zhao, H. (2010). Analyzing responses of mouse olfactory sensory neurons using the air-phase electroolfactogram recording. J Vis Exp.

Von Dannecker, L. E. C., Mercadante, A. F., and Malnic, B. (2005). Ric-8B, an olfactory putative GTP exchange factor, amplifies signal transduction through the olfactory-specific G-protein Galphaolf. J. Neurosci. *25*, 3793–3800.

Das, S., Hahn, Y., Walker, D. A., Nagata, S., Willingham, M. C., Peehl, D. M., Bera, T. K., Lee, B., and Pastan, I. (2008). Topology of NGEP, a prostate-specific cell:cell junction protein widely expressed in many cancers of different grade level. Cancer Res *68*, 6306–6312.

Davis, A. J., Forrest, A. S., Jepps, T. A., Valencik, M. L., Wiwchar, M., Singer, C. A., Sones, W. R., Greenwood, I. A., and Leblanc, N. (2010). Expression profile and protein translation of TMEM16A in murine smooth muscle. Am. J. Physiol., Cell Physiol *299*, C948–C959.

Dawson, T. M., Arriza, J. L., Jaworsky, D. E., Borisy, F. F., Attramadal, H., Lefkowitz, R. J., and Ronnett, G. V. (1993). Beta-adrenergic receptor kinase-2 and beta-arrestin-2 as mediators of odorant-induced desensitization. Science *259*, 825–829.

Demaria, S., and Ngai, J. (2010). Review series: The cell biology of smell. J. Cell Biol *191*, 443–452.

Dixon, R. E., Hennig, G. W., Baker, S. A., Britton, F. C., Harfe, B. D., Rock, J. R., Sanders, K. M., and Ward, S. M. (2011). Electrical Slow Waves in the Mouse Oviduct Are Dependent upon a Calcium Activated Chloride Conductance Encoded by Tmem16a. Biology of Reproduction. Epub ahead of print.

Doty, R. L. (2009). The olfactory system and its disorders. Semin Neurol *29*, 74–81.

Dubin, A. E., and Dionne, V. E. (1994). Action potentials and chemosensitive conductances in the dendrites of olfactory neurons suggest new features for odor transduction. J. Gen. Physiol *103*, 181–201.

Duran, C., and Hartzell, H. C. (2011). Physiological roles and diseases of tmem16/anoctamin proteins: are they all chloride channels? Acta Pharmacol. Sin *32*, 685–692.

Dutta, A. K., Khimji, A.-karim, Kresge, C., Bugde, A., Dougherty, M., Esser, V., Ueno, Y., Glaser, S. S., Alpini, G., Rockey, D. C., et al. (2011). Identification and functional characterization of TMEM16A, a Ca2+-activated Cl- channel activated by extracellular nucleotides, in biliary epithelium. J. Biol. Chem. *286*, 766–776.

Dzeja, C., Hagen, V., Kaupp, U. B., and Frings, S. (1999). Ca2+ permeation in cyclic nucleotide-gated channels. EMBO J *18*, 131–144.

Elsaesser, R., and Paysan, J. (2007). The sense of smell, its signalling pathways, and the dichotomy of cilia and microvilli in olfactory sensory cells. BMC Neurosci *8 Suppl 3*, S1.

Evans, R. L., Park, K., Turner, R. J., Watson, G. E., Nguyen, H. V., Dennett, M. R., Hand, A. R., Flagella, M., Shull, G. E., and Melvin, J. E. (2000). Severe impairment of salivation in Na+/K+/2Cl- cotransporter (NKCC1)-deficient mice. J. Biol. Chem. *275*, 26720–26726.

Fallah, G., Römer, T., Detro-Dassen, S., Braam, U., Markwardt, F., and Schmalzing, G. (2011). TMEM16A(a)/anoctamin-1 shares a homodimeric architecture with CLC chloride channels. Mol. Cell Proteomics *10*, M110.004697.

Farley, F. W., Soriano, P., Steffen, L. S., and Dymecki, S. M. (2000). Widespread recombinase expression using FLPeR (flipper) mice. Genesis *28*, 106–110.

Feinstein, P., and Mombaerts, P. (2004). A contextual model for axonal sorting into glomeruli in the mouse olfactory system. Cell *117*, 817–831.

Feinstein, P., Bozza, T., Rodriguez, I., Vassalli, A., and Mombaerts, P. (2004). Axon guidance of mouse olfactory sensory neurons by odorant receptors and the beta2 adrenergic receptor. Cell *117*, 833–846.

Feldmesser, E., Bercovich, D., Avidan, N., Halbertal, S., Haim, L., Gross-Isseroff, R., Goshen, S., and Lancet, D. (2007). Mutations in olfactory signal transduction genes are not a major cause of human congenital general anosmia. Chem. Senses *32*, 21–30.

Ferrera, L., Caputo, A., and Galietta, L. J. V. (2010). TMEM16A Protein: A New Identity for Ca2+-Dependent Cl- Channels. Physiology (Bethesda) *25*, 357–363.

Ferrera, L., Caputo, A., Ubby, I., Bussani, E., Zegarra-Moran, O., Ravazzolo, R., Pagani, F., and Galietta, L. J. V. (2009). Regulation of TMEM16A chloride channel properties by alternative splicing. J. Biol. Chem *284*, 33360–33368.

Firestein, S. (2001). How the olfactory system makes sense of scents. Nature *413*, 211–218.

Firestein, S., and Werblin, F. (1989). Odor-induced membrane currents in vertebrate-olfactory receptor neurons. Science *244*, 79–82.

Fleischer, J., Mamasuew, K., and Breer, H. (2009). Expression of cGMP signaling elements in the Grueneberg ganglion. Histochem. Cell Biol *131*, 75–88.

Fleischer, J., Schwarzenbacher, K., and Breer, H. (2007). Expression of trace amine-associated receptors in the Grueneberg ganglion. Chem. Senses *32*, 623–631.

Frings, S. (2009). Primary processes in sensory cells: current advances. J. Comp. Physiol. A Neuroethol. Sens. Neural. Behav. Physiol *195*, 1–19.

Frings, S., Reuter, D., and Kleene, S. J. (2000). Neuronal Ca2+ -activated Cl- channels--homing in on an elusive channel species. Prog. Neurobiol *60*, 247–289.

Frisch, D. (1967). Ultrastructure of mouse olfactory mucosa. Am. J. Anat *121*, 87–120.

Fülle, H. J., Vassar, R., Foster, D. C., Yang, R. B., Axel, R., and Garbers, D. L. (1995). A receptor guanylyl cyclase expressed specifically in olfactory sensory neurons. Proc. Natl. Acad. Sci. U.S.A. *92*, 3571–3575.

Fuss, S. H., Omura, M., and Mombaerts, P. (2005). The Grueneberg ganglion of the mouse projects axons to glomeruli in the olfactory bulb. Eur. J. Neurosci *22*, 2649–2654.

Gásdal Karstensen, H., and Tommerup, N. (2011). Isolated and syndromic forms of congenital anosmia. Clinical Genetics. Epub ahead of print.

Genter, M. B., Van Veldhoven, P. P., Jegga, A. G., Sakthivel, B., Kong, S., Stanley, K., Witte, D. P., Ebert, C. L., and Aronow, B. J. (2003). Microarray-based discovery of highly expressed olfactory mucosal genes: potential roles in the various functions of the olfactory system. Physiol. Genomics *16*, 67–81.

Giannetti, N., Saucier, D., and Astic, L. (1995). Analysis of the possible altering function of the septal organ in rats: a lesional and behavioral study. Physiol. Behav *58*, 837–845.

Gomez-Pinilla, P. J., Gibbons, S. J., Bardsley, M. R., Lorincz, A., Pozo, M. J., Pasricha, P. J., Van de Rijn, M., West, R. B., Sarr, M. G., Kendrick, M. L., et al. (2009). Ano1 is a selective marker of interstitial cells of Cajal in the human and mouse gastrointestinal tract. Am. J. Physiol. Gastrointest. Liver Physiol *296*, G1370–G1381.

Greenwood, I. A., and Leblanc, N. (2007). Overlapping pharmacology of Ca2+-activated Cl- and K+ channels. Trends Pharmacol. Sci. *28*, 1–5.

Gritli-Linde, A., Vaziri Sani, F., Rock, J. R., Hallberg, K., Iribarne, D., Harfe, B. D., and Linde, A. (2009). Expression patterns of the Tmem16 gene family during cephalic development in the mouse. Gene Expr. Patterns *9*, 178–191.

Grosmaitre, X., Santarelli, L. C., Tan, J., Luo, M., and Ma, M. (2007). Dual functions of mammalian olfactory sensory neurons as odor detectors and mechanical sensors. Nat. Neurosci *10*, 348–354.

Grüneberg, H. (1973). A ganglion probably belonging to the N. terminalis system in the nasal mucosa of the mouse. Z Anat Entwicklungsgesch *140*, 39–52.

Haga, S., Hattori, T., Sato, T., Sato, K., Matsuda, S., Kobayakawa, R., Sakano, H., Yoshihara, Y., Kikusui, T., and Touhara, K. (2010). The male mouse pheromone ESP1 enhances female sexual receptive behaviour through a specific vomeronasal receptor. Nature *466*, 118–122.

Hahn, Y., Kim, D. S., Pastan, I. H., and Lee, B. (2009). Anoctamin and transmembrane channel-like proteins are evolutionarily related. Int. J. Mol. Med *24*, 51–55.

Hartzell, C., Putzier, I., and Arreola, J. (2005). Calcium-activated chloride channels. Annu. Rev. Physiol *67*, 719–758.

Hartzell, H. C., Yu, K., Xiao, Q., Chien, L.-T., and Qu, Z. (2009). Anoctamin/TMEM16 family members are Ca2+-activated Cl- channels. J. Physiol. (Lond.) *587*, 2127–2139.

Hasin-Brumshtein, Y., Lancet, D., and Olender, T. (2009). Human olfaction: from genomic variation to phenotypic diversity. Trends Genet *25*, 178–184.

He, J., Ma, L., Kim, S., Nakai, J., and Yu, C. R. (2008). Encoding gender and individual information in the mouse vomeronasal organ. Science *320*, 535–538.

Hengl, T., Kaneko, H., Dauner, K., Vocke, K., Frings, S., and Möhrlen, F. (2010). Molecular components of signal amplification in olfactory sensory cilia. Proc. Natl. Acad. Sci. U.S.A *107*, 6052–6057.

Herness, M. S., and Sun, X. D. (1999). Characterization of chloride currents and their noradrenergic modulation in rat taste receptor cells. J. Neurophysiol *82*, 260–271.

Hu, J., Zhong, C., Ding, C., Chi, Q., Walz, A., Mombaerts, P., Matsunami, H., and Luo, M. (2007). Detection of near-atmospheric concentrations of CO2 by an olfactory subsystem in the mouse. Science *317*, 953–957.

Huang, F., Rock, J. R., Harfe, B. D., Cheng, T., Huang, X., Jan, Y. N., and Jan, L. Y. (2009). Studies on expression and function of the TMEM16A calcium-activated chloride channel. Proc. Natl. Acad. Sci. U.S.A *106*, 21413–21418.

Imai, T., Suzuki, M., and Sakano, H. (2006). Odorant receptor-derived cAMP signals direct axonal targeting. Science *314*, 657–661.

Isogai, Y., Si, S., Pont-Lezica, L., Tan, T., Kapoor, V., Murthy, V. N., and Dulac, C. (2011). Molecular organization of vomeronasal chemoreception. Nature *478*, 241–245.

Jaén, C., Ozdener, M. H., and Reisert, J. (2011). Mechanisms of chloride uptake in frog olfactory receptor neurons. J. Comp. Physiol. A Neuroethol. Sens. Neural. Behav. Physiol. *197*, 339–349.

Jentsch, T. J. (2008). CLC chloride channels and transporters: from genes to protein structure, pathology and physiology. Crit. Rev. Biochem. Mol. Biol *43*, 3–36.

Jeon, J. H., Park, J. W., Lee, J. W., Jeong, S. W., Yeo, S. W., and Kim, I.-B. (2011). Expression and immunohistochemical localization of TMEM16A/anoctamin 1, a calcium-activated chloride channel in the mouse cochlea. Cell Tissue Res. *345*, 223–230.

Joshi, H., Getchell, M. L., Zielinski, B., and Getchell, T. V. (1987). Spectrophotometric determination of cation concentrations in olfactory mucus. Neurosci. Lett *82*, 321–326.

Juilfs, D. M., Fülle, H. J., Zhao, A. Z., Houslay, M. D., Garbers, D. L., and Beavo, J. A. (1997). A subset of olfactory neurons that selectively express cGMP-stimulated phosphodiesterase (PDE2) and guanylyl cyclase-D define a unique olfactory signal transduction pathway. Proc. Natl. Acad. Sci. U.S.A *94*, 3388–3395.

Kaneko, H., Putzier, I., Frings, S., Kaupp, U. B., and Gensch, T. (2004). Chloride accumulation in mammalian olfactory sensory neurons. J. Neurosci *24*, 7931–7938.

Kidd, J. F., and Thorn, P. (2000). Intracellular Ca2+ and Cl- channel activation in secretory cells. Annu. Rev. Physiol *62*, 493–513.

Kim, S., Ma, L., and Yu, C. R. (2011). Requirement of calcium-activated chloride channels in the activation of mouse vomeronasal neurons. Nat Commun *2*, 365.

Kimchi, T., Xu, J., and Dulac, C. (2007). A functional circuit underlying male sexual behaviour in the female mouse brain. Nature *448*, 1009–1014.

Kimoto, H., Haga, S., Sato, K., and Touhara, K. (2005). Sex-specific peptides from exocrine glands stimulate mouse vomeronasal sensory neurons. Nature *437*, 898–901.

Kleene, S. J. (1997). High-gain, low-noise amplification in olfactory transduction. Biophys. J *73*, 1110–1117.

Kleene, S. J. (2009). Limits of calcium clearance by plasma membrane calcium ATPase in olfactory cilia. PLoS ONE *4*, e5266.

Kleene, S. J. (1993). Origin of the chloride current in olfactory transduction. Neuron *11*, 123–132.

Kleene, S. J. (2008). The electrochemical basis of odor transduction in vertebrate olfactory cilia. Chem. Senses *33*, 839–859.

Kleene, S. J., and Gesteland, R. C. (1991a). Calcium-activated chloride conductance in frog olfactory cilia. J. Neurosci *11*, 3624–3629.

Kleene, S. J., and Gesteland, R. C. (1991b). Transmembrane currents in frog olfactory cilia. J. Membr. Biol *120*, 75–81.

Kleene, S. J., and Pun, R. Y. (1996). Persistence of the olfactory receptor current in a wide variety of extracellular environments. J. Neurophysiol *75*, 1386–1391.

Klimmeck, D., Daiber, P. C., Brühl, A., Baumann, A., Frings, S., and Möhrlen, F. (2009). Bestrophin 2: an anion channel associated with neurogenesis in chemosensory systems. J. Comp. Neurol *515*, 585–599.

Klimmeck, D., Mayer, U., Ungerer, N., Warnken, U., Schnölzer, M., Frings, S., and Möhrlen, F. (2008). Calcium-signaling networks in olfactory receptor neurons. Neuroscience *151*, 901–912.

Kurahashi, T., and Yau, K. W. (1993). Co-existence of cationic and chloride components in odorant-induced current of vertebrate olfactory receptor cells. Nature *363*, 71–74.

Kurima, K., Yang, Y., Sorber, K., and Griffith, A. J. (2003). Characterization of the transmembrane channel-like (TMC) gene family: functional clues from hearing loss and epidermodysplasia verruciformis. Genomics *82*, 300–308.

Kuruma, A., and Hartzell, H. C. (2000). Bimodal control of a Ca(2+)-activated Cl(-) channel by different Ca(2+) signals. J. Gen. Physiol. *115*, 59–80.

Lagostena, L., and Menini, A. (2003). Whole-cell recordings and photolysis of caged compounds in olfactory sensory neurons isolated from the mouse. Chem. Senses *28*, 705–716.

Lalonde, M. R., Kelly, M. E., and Barnes, S. (2008). Calcium-activated chloride channels in the retina. Channels (Austin) *2*, 252–260.

Larsson, H. P., Kleene, S. J., and Lecar, H. (1997). Noise analysis of ion channels in non-space-clamped cables: estimates of channel parameters in olfactory cilia. Biophys. J *72*, 1193–1203.

Leblanc, N., Ledoux, J., Saleh, S., Sanguinetti, A., Angermann, J., O'Driscoll, K., Britton, F., Perrino, B. A., and Greenwood, I. A. (2005). Regulation of calcium-activated chloride channels in smooth muscle cells: a complex picture is emerging. Can. J. Physiol. Pharmacol *83*, 541–556.

Leinders-Zufall, T., Brennan, P., Widmayer, P., S., P. C., Maul-Pavicic, A., Jager, M., Li, X.-H., Breer, H., Zufall, F., and Boehm, T. (2004). MHC Class I Peptides as Chemosensory Signals in the Vomeronasal Organ. Science *306*, 1033–1037.

Leinders-Zufall, T., Cockerham, R. E., Michalakis, S., Biel, M., Garbers, D. L., Reed, R. R., Zufall, F., and Munger, S. D. (2007). Contribution of the receptor guanylyl cyclase GC-D to chemosensory function in the olfactory epithelium. Proc. Natl. Acad. Sci. U.S.A *104*, 14507–14512.

Leinders-Zufall, T., Lane, A. P., Puche, A. C., Ma, W., Novotny, M. V., Shipley, M. T., and Zufall, F. (2000). Ultrasensitive pheromone detection by mammalian vomeronasal neurons. Nature *405*, 792–796.

Leinders-Zufall, T., Ma, M., and Zufall, F. (1999). Impaired odor adaptation in olfactory receptor neurons after inhibition of Ca2+/calmodulin kinase II. J. Neurosci *19*, RC19.

Leinders-Zufall, T., Rand, M. N., Shepherd, G. M., Greer, C. A., and Zufall, F. (1997). Calcium entry through cyclic nucleotide-gated channels in individual cilia of olfactory receptor cells: spatiotemporal dynamics. J. Neurosci *17*, 4136–4148.

Leypold, B. G., Yu, C. R., Leinders-Zufall, T., Kim, M. M., Zufall, F., and Axel, R. (2002). Altered sexual and social behaviors in trp2 mutant mice. Proc. Natl. Acad. Sci. U.S.A *99*, 6376–6381.

Li, J., Ishii, T., Feinstein, P., and Mombaerts, P. (2004). Odorant receptor gene choice is reset by nuclear transfer from mouse olfactory sensory neurons. Nature *428*, 393–399.

Liberles, S. D., and Buck, L. B. (2006). A second class of chemosensory receptors in the olfactory epithelium. Nature *442*, 645–650.

Liberles, S. D., Horowitz, L. F., Kuang, D., Contos, J. J., Wilson, K. L., Siltberg-Liberles, J., Liberles, D. A., and Buck, L. B. (2009). Formyl peptide receptors are candidate chemosensory receptors in the vomeronasal organ. Proc. Natl. Acad. Sci. U.S.A. *106*, 9842–9847.

Liman, E. R., and Buck, L. B. (1994). A second subunit of the olfactory cyclic nucleotide-gated channel confers high sensitivity to cAMP. Neuron *13*, 611–621.

Liman, E. R., Corey, D. P., and Dulac, C. (1999). TRP2: a candidate transduction channel for mammalian pheromone sensory signaling. Proc. Natl. Acad. Sci. U.S.A *96*, 5791–5796.

Lin, D. M., Wang, F., Lowe, G., Gold, G. H., Axel, R., Ngai, J., and Brunet, L. (2000). Formation of precise connections in the olfactory bulb occurs in the absence of odorant-evoked neuronal activity. Neuron *26*, 69–80.

Lin, W., Arellano, J., Slotnick, B., and Restrepo, D. (2004). Odors detected by mice deficient in cyclic nucleotide-gated channel subunit A2 stimulate the main olfactory system. J. Neurosci *24*, 3703–3710.

Lindemann, B. (2001). Predicted profiles of ion concentrations in olfactory cilia in the steady state. Biophys. J *80*, 1712–1721.

Liu, C. Y., Fraser, S. E., and Koos, D. S. (2009). Grueneberg ganglion olfactory subsystem employs a cGMP signaling pathway. J. Comp. Neurol *516*, 36–48.

Lowe, G., and Gold, G. H. (1993). Nonlinear amplification by calcium-dependent chloride channels in olfactory receptor cells. Nature *366*, 283–286.

Lucas, P., Ukhanov, K., Leinders-Zufall, T., and Zufall, F. (2003). A diacylglycerol-gated cation channel in vomeronasal neuron dendrites is impaired in TRPC2 mutant mice: mechanism of pheromone transduction. Neuron *40*, 551–561.

Ma, M., Grosmaitre, X., Iwema, C. L., Baker, H., Greer, C. A., and Shepherd, G. M. (2003). Olfactory signal transduction in the mouse septal organ. J. Neurosci *23*, 317–324.

Mamasuew, K., Breer, H., and Fleischer, J. (2008). Grueneberg ganglion neurons respond to cool ambient temperatures. Eur. J. Neurosci *28*, 1775–1785.

Mamasuew, K., Hofmann, N., Breer, H., and Fleischer, J. (2011). Grueneberg ganglion neurons are activated by a defined set of odorants. Chem. Senses *36*, 271–282.

Mandiyan, V. S., Coats, J. K., and Shah, N. M. (2005). Deficits in sexual and aggressive behaviors in Cnga2 mutant mice. Nat. Neurosci *8*, 1660–1662.

Mayer, U., Küller, A., Daiber, P. C., Neudorf, I., Warnken, U., Schnölzer, M., Frings, S., and Möhrlen, F. (2009). The proteome of rat olfactory sensory cilia. Proteomics *9*, 322–334.

Mayer, U., Ungerer, N., Klimmeck, D., Warnken, U., Schnölzer, M., Frings, S., and Möhrlen, F. (2008). Proteomic analysis of a membrane preparation from rat olfactory sensory cilia. Chem. Senses *33*, 145–162.

Melvin, J. E., Yule, D., Shuttleworth, T., and Begenisich, T. (2005). Regulation of fluid and electrolyte secretion in salivary gland acinar cells. Annu. Rev. Physiol *67*, 445–469.

Menco, B. P. (1997). Ultrastructural aspects of olfactory signaling. Chem. Senses *22*, 295–311.

Menco, B. P., and Farbman, A. I. (1992). Ultrastructural evidence for multiple mucous domains in frog olfactory epithelium. Cell Tissue Res *270*, 47–56.

Michalakis, S., Reisert, J., Geiger, H., Wetzel, C., Zong, X., Bradley, J., Spehr, M., Hüttl, S., Gerstner, A., Pfeifer, A., et al. (2006). Loss of CNGB1 protein leads to olfactory dysfunction and subciliary cyclic nucleotide-gated channel trapping. J. Biol. Chem *281*, 35156–35166.

Milenkovic, V. M., Brockmann, M., Stohr, H., Weber, B. H., and Strauss, O. (2010). Evolution and functional divergence of the anoctamin family of membrane proteins. BMC Evol Biol *10*, 319.

Mombaerts, P. (2006). Axonal wiring in the mouse olfactory system. Annu. Rev. Cell Dev. Biol *22*, 713–737.

Mombaerts, P., Wang, F., Dulac, C., Chao, S. K., Nemes, A., Mendelsohn, M., Edmondson, J., and Axel, R. (1996). Visualizing an olfactory sensory map. Cell *87*, 675–686.

Mori, K., and Sakano, H. (2011). How is the olfactory map formed and interpreted in the mammalian brain? Annu. Rev. Neurosci *34*, 467–499.

Munger, S. D., Lane, A. P., Zhong, H., Leinders-Zufall, T., Yau, K. W., Zufall, F., and Reed, R. R. (2001). Central role of the CNGA4 channel subunit in Ca2+-calmodulin-dependent odor adaptation. Science *294*, 2172–2175.

Nagy, A., Rossant, J., Nagy, R., Abramow-Newerly, W., and Roder, J. C. (1993). Derivation of completely cell culture-derived mice from early-passage embryonic stem cells. Proc. Natl. Acad. Sci. U.S.A *90*, 8424–8428.

Nakamura, T., Kaneko, H., and Nishida, N. (1997). Direct measurement of the chloride concentration in newt olfactory receptors with the fluorescent probe. Neurosci. Lett *237*, 5–8.

Namkung, W., Phuan, P.-W., and Verkman, A. S. (2011). TMEM16A inhibitors reveal TMEM16A as a minor component of calcium-activated chloride channel conductance in airway and intestinal epithelial cells. J. Biol. Chem. *286*, 2365–2374.

Nguyen-Khoa, B.-A., Goehring, E. L., Jr, Vendiola, R. M., Pezzullo, J. C., and Jones, J. K. (2007). Epidemiologic study of smell disturbance in 2 medical insurance claims populations. Arch. Otolaryngol. Head Neck Surg *133*, 748–757.

Nickell, W. T., Kleene, N. K., and Kleene, S. J. (2007). Mechanisms of neuronal chloride accumulation in intact mouse olfactory epithelium. J. Physiol. (Lond.) *583*, 1005–1020.

Nickell, W. T., Kleene, N. K., Gesteland, R. C., and Kleene, S. J. (2006). Neuronal chloride accumulation in olfactory epithelium of mice lacking NKCC1. J. Neurophysiol *95*, 2003–2006.

Nozawa, M., Kawahara, Y., and Nei, M. (2007). Genomic drift and copy number variation of sensory receptor genes in humans. Proc. Natl. Acad. Sci. U.S.A *104*, 20421–20426.

Otowa, T., Yoshida, E., Sugaya, N., Yasuda, S., Nishimura, Y., Inoue, K., Tochigi, M., Umekage, T., Miyagawa, T., Nishida, N., et al. (2009). Genome-wide association study of panic disorder in the Japanese population. J. Hum. Genet *54*, 122–126.

Ousingsawat, J., Martins, J. R., Schreiber, R., Rock, J. R., Harfe, B. D., and Kunzelmann, K. (2009). Loss of TMEM16A causes a defect in epithelial Ca2+-dependent chloride transport. J. Biol. Chem *284*, 28698–28703.

Park, M. K., Lomax, R. B., Tepikin, A. V., and Petersen, O. H. (2001). Local uncaging of caged Ca(2+) reveals distribution of Ca(2+)-activated Cl(-) channels in pancreatic acinar cells. Proc. Natl. Acad. Sci. U.S.A. *98*, 10948–10953.

Paysan, J., and Breer, H. (2001). Molecular physiology of odor detection: current views. Pflugers Arch *441*, 579–586.

Peppel, K., Boekhoff, I., McDonald, P., Breer, H., Caron, M. G., and Lefkowitz, R. J. (1997). G protein-coupled receptor kinase 3 (GRK3) gene disruption leads to loss of odorant receptor desensitization. J. Biol. Chem *272*, 25425–25428.

Pfaffl, M. W. (2001). A new mathematical model for relative quantification in real-time RT-PCR. Nucleic Acids Res. *29*, e45.

Pifferi, S., Dibattista, M., and Menini, A. (2009a). TMEM16B induces chloride currents activated by calcium in mammalian cells. Pflugers Arch *458*, 1023–1038.

Pifferi, S., Dibattista, M., Sagheddu, C., Boccaccio, A., Al Qteishat, A., Ghirardi, F., Tirindelli, R., and Menini, A. (2009b). Calcium-activated chloride currents in olfactory sensory neurons from mice lacking bestrophin-2. J. Physiol. (Lond.) *587*, 4265–4279.

Pifferi, S., Menini, A., and Kurahashi, T. (2009c). Signal Transduction in Vertebrate Olfactory Cilia. In The Neurobiology of Olfaction, A. Menini, ed. (CRC Press), pp. 203–224.

Pifferi, S., Pascarella, G., Boccaccio, A., Mazzatenta, A., Gustincich, S., Menini, A., and Zucchelli, S. (2006). Bestrophin-2 is a candidate calcium-activated chloride channel involved in olfactory transduction. Proc. Natl. Acad. Sci. U.S.A *103*, 12929–12934.

Del Punta, K., Leinders-Zufall, T., Rodriguez, I., Jukam, D., Wysocki, C. J., Ogawa, S., Zufall, F., and Mombaerts, P. (2002). Deficient pheromone responses in mice lacking a cluster of vomeronasal receptor genes. Nature *419*, 70–74.

Puntervoll, P., Linding, R., Gemünd, C., Chabanis-Davidson, S., Mattingsdal, M., Cameron, S., Martin, D. M. A., Ausiello, G., Brannetti, B., Costantini, A., et al. (2003). ELM server: A new resource for investigating short functional sites in modular eukaryotic proteins. Nucleic Acids Res. *31*, 3625–3630.

Pyrski, M., Koo, J. H., Polumuri, S. K., Ruknudin, A. M., Margolis, J. W., Schulze, D. H., and Margolis, F. L. (2007). Sodium/calcium exchanger expression in the mouse and rat olfactory systems. J. Comp. Neurol *501*, 944–958.

Rasche, S., Toetter, B., Adler, J., Tschapek, A., Doerner, J. F., Kurtenbach, S., Hatt, H., Meyer, H., Warscheid, B., and Neuhaus, E. M. (2010). Tmem16b is specifically expressed in the cilia of olfactory sensory neurons. Chem. Senses *35*, 239–245.

Reisert, J., and Matthews, H. R. (1998). Na+-dependent Ca2+ extrusion governs response recovery in frog olfactory receptor cells. J. Gen. Physiol *112*, 529–535.

Reisert, J., and Zhao, H. (2011). Perspectives on: Information and coding in mammalian sensory physiology: Response kinetics of olfactory receptor neurons and the implications in olfactory coding. J. Gen. Physiol. *138*, 303–310.

Reisert, J., Bauer, P. J., Yau, K.-W., and Frings, S. (2003). The Ca-activated Cl channel and its control in rat olfactory receptor neurons. J. Gen. Physiol *122*, 349–363.

Reisert, J., Lai, J., Yau, K.-W., and Bradley, J. (2005). Mechanism of the excitatory Cl- response in mouse olfactory receptor neurons. Neuron *45*, 553–561.

Reuter, D., Zierold, K., Schröder, W. H., and Frings, S. (1998). A depolarizing chloride current contributes to chemoelectrical transduction in olfactory sensory neurons in situ. J. Neurosci *18*, 6623–6630.

Rivière, S., Challet, L., Fluegge, D., Spehr, M., and Rodriguez, I. (2009). Formyl peptide receptor-like proteins are a novel family of vomeronasal chemosensors. Nature *459*, 574–577.

Rock, J. R., and Harfe, B. D. (2008). Expression of TMEM16 paralogs during murine embryogenesis. Dev. Dyn *237*, 2566–2574.

Rock, J. R., Futtner, C. R., and Harfe, B. D. (2008). The transmembrane protein TMEM16A is required for normal development of the murine trachea. Dev. Biol *321*, 141–149.

Rock, J. R., O'Neal, W. K., Gabriel, S. E., Randell, S. H., Harfe, B. D., Boucher, R. C., and Grubb, B. R. (2009). Transmembrane protein 16A (TMEM16A) is a Ca2+-regulated Cl- secretory channel in mouse airways. J. Biol. Chem *284*, 14875–14880.

Rodolfo-Masera, T. (1943). Su l'estizenza di un particulare organo olfacttivo nel setto nasale della cavia e di altri roditori. Arch. Ital. Anat. Embryol. *48*, 157–212.

Romanenko, V. G., Catalán, M. A., Brown, D. A., Putzier, I., Hartzell, H. C., Marmorstein, A. D., Gonzalez-Begne, M., Rock, J. R., Harfe, B. D., and Melvin, J. E. (2010). Tmem16A encodes the Ca2+-activated Cl- channel in mouse submandibular salivary gland acinar cells. J. Biol. Chem *285*, 12990–13001.

Roppolo, D., Ribaud, V., Jungo, V. P., Lüscher, C., and Rodriguez, I. (2006). Projection of the Grüneberg ganglion to the mouse olfactory bulb. Eur. J. Neurosci *23*, 2887–2894.

de la Rosa-Prieto, C., Saiz-Sanchez, D., Ubeda-Bañon, I., Argandoña-Palacios, L., Garcia-Muñozguren, S., and Martinez-Marcos, A. (2010). Neurogenesis in subclasses of vomeronasal sensory neurons in adult mice. Dev Neurobiol *70*, 961–970.

Rozen, S., and Skaletsky, H. (2000). Primer3 on the WWW for general users and for biologist programmers. Methods Mol. Biol. *132*, 365–386.

Sagheddu, C., Boccaccio, A., Dibattista, M., Montani, G., Tirindelli, R., and Menini, A. (2010). Calcium concentration jumps reveal dynamic ion selectivity of calcium-activated chloride currents in mouse olfactory sensory neurons and TMEM16b-transfected HEK 293T cells. J. Physiol. (Lond.) *588*, 4189–4204.

Sam, M., Vora, S., Malnic, B., Ma, W., Novotny, M. V., and Buck, L. B. (2001). Neuropharmacology. Odorants may arouse instinctive behaviours. Nature *412*, 142.

Sambrook, J., and Russell, D. W. (2001). Molecular cloning: a laboratory manual (CSHL Press).

Sammeta, N., Yu, T.-T., Bose, S. C., and McClintock, T. S. (2007). Mouse olfactory sensory neurons express 10,000 genes. J. Comp. Neurol *502*, 1138–1156.

Sánchez-Vives, M. V., and Gallego, R. (1994). Calcium-dependent chloride current induced by axotomy in rat sympathetic neurons. J. Physiol. (Lond.) *475*, 391–400.

Sato, K., and Suzuki, N. (2000). The contribution of a Ca(2+)-activated Cl(-) conductance to amino-acid-induced inward current responses of ciliated olfactory neurons of the rainbow trout. J. Exp. Biol *203*, 253–262.

Sayers, E. W., Barrett, T., Benson, D. A., Bolton, E., Bryant, S. H., Canese, K., Chetvernin, V., Church, D. M., DiCuccio, M., Federhen, S., et al. (2011). Database resources of the National Center for Biotechnology Information. Nucleic Acids Res. *39*, D38–D51.

Schmid, A., Pyrski, M., Biel, M., Leinders-Zufall, T., and Zufall, F. (2010). Grueneberg ganglion neurons are finely tuned cold sensors. J. Neurosci *30*, 7563–7568.

Schreiber, R., Uliyakina, I., Kongsuphol, P., Warth, R., Mirza, M., Martins, J. R., and Kunzelmann, K. (2010). Expression and function of epithelial anoctamins. J. Biol. Chem *285*, 7838–7845.

Schroeder, B. C., Cheng, T., Jan, Y. N., and Jan, L. Y. (2008). Expression cloning of TMEM16A as a calcium-activated chloride channel subunit. Cell *134*, 1019–1029.

Schwenk, F., Baron, U., and Rajewsky, K. (1995). A cre-transgenic mouse strain for the ubiquitous deletion of loxP-flanked gene segments including deletion in germ cells. Nucleic Acids Res *23*, 5080–5081.

Scott, J. W., and Scott-Johnson, P. E. (2002). The electroolfactogram: a review of its history and uses. Microsc. Res. Tech *58*, 152–160.

Scott, R. H., Sutton, K. G., Griffin, A., Stapleton, S. R., and Currie, K. P. (1995). Aspects of calcium-activated chloride currents: a neuronal perspective. Pharmacol. Ther *66*, 535–565.

Seifert, K., and Ule, G. (1966). Die Ultrastruktur der Riechschleimhaut der neugeborenen und jugendlichen weissen Maus. Zeitschrift für Zellforschung *76*, 147–169.

Serizawa, S., Miyamichi, K., and Sakano, H. (2004). One neuron-one receptor rule in the mouse olfactory system. Trends Genet *20*, 648–653.

Sheridan, J. T., Worthington, E. N., Yu, K., Gabriel, S. E., Hartzell, H. C., and Tarran, R. (2011). Characterization of the oligomeric structure of the Ca(2+)-activated Cl- channel Ano1/TMEM16A. J. Biol. Chem *286*, 1381–1388.

Shimazaki, R., Boccaccio, A., Mazzatenta, A., Pinato, G., Migliore, M., and Menini, A. (2006). Electrophysiological properties and modeling of murine vomeronasal sensory neurons in acute slice preparations. Chem. Senses *31*, 425–435.

Slotnick, B., and Restrepo, D. (2005). Olfactometry with mice. Curr Protoc Neurosci *Chapter 8*, Unit 8.20.

Smith, D. W., Thach, S., Marshall, E. L., Mendoza, M.-G., and Kleene, S. J. (2008). Mice lacking NKCC1 have normal olfactory sensitivity. Physiol. Behav *93*, 44–49.

Song, Y., Cygnar, K. D., Sagdullaev, B., Valley, M., Hirsh, S., Stephan, A., Reisert, J., and Zhao, H. (2008). Olfactory CNG channel desensitization by Ca2+/CaM via the B1b subunit affects response termination but not sensitivity to recurring stimulation. Neuron *58*, 374–386.

Spehr, M., Kelliher, K. R., Li, X.-H., Boehm, T., Leinders-Zufall, T., and Zufall, F. (2006). Essential role of the main olfactory system in social recognition of major histocompatibility complex peptide ligands. J. Neurosci *26*, 1961–1970.

Stephan, A. B., Shum, E. Y., Hirsh, S., Cygnar, K. D., Reisert, J., and Zhao, H. (2009). ANO2 is the cilial calcium-activated chloride channel that may mediate olfactory amplification. Proc. Natl. Acad. Sci. U.S.A *106*, 11776–11781.

Stöhr, H., Heisig, J. B., Benz, P. M., Schöberl, S., Milenkovic, V. M., Strauss, O., Aartsen, W. M., Wijnholds, J., Weber, B. H. F., and Schulz, H. L. (2009). TMEM16B, a novel protein with calcium-dependent chloride channel activity, associates with a presynaptic protein complex in photoreceptor terminals. J. Neurosci *29*, 6809–6818.

Stöhr, H., Mah, N., Schulz, H. L., Gehrig, A., Fröhlich, S., and Weber, B. H. (2000). EST mining of the UniGene dataset to identify retina-specific genes. Cytogenet. Cell Genet *91*, 267–277.

Storan, M. J., and Key, B. (2006). Septal organ of Grüneberg is part of the olfactory system. J. Comp. Neurol *494*, 834–844.

Stowers, L., Holy, T. E., Meister, M., Dulac, C., and Koentges, G. (2002). Loss of sex discrimination and male-male aggression in mice deficient for TRP2. Science *295*, 1493–1500.

Strotmann, J., Levai, O., Fleischer, J., Schwarzenbacher, K., and Breer, H. (2004). Olfactory receptor proteins in axonal processes of chemosensory neurons. J. Neurosci. *24*, 7754–7761.

Su, C.-Y., Menuz, K., and Carlson, J. R. (2009). Olfactory perception: receptors, cells, and circuits. Cell *139*, 45–59.

Suzuki, J., Umeda, M., Sims, P. J., and Nagata, S. (2010). Calcium-dependent phospholipid scrambling by TMEM16F. Nature *468*, 834–838.

Taylor, R., and Roper, S. (1994). Ca(2+)-dependent Cl- conductance in taste cells from Necturus. J. Neurophysiol *72*, 475–478.

Tirindelli, R., Dibattista, M., Pifferi, S., and Menini, A. (2009). From pheromones to behavior. Physiol. Rev *89*, 921–956.

Trinh, K., and Storm, D. R. (2003). Vomeronasal organ detects odorants in absence of signaling through main olfactory epithelium. Nat. Neurosci *6*, 519–525.

Truett, G. E., Heeger, P., Mynatt, R. L., Truett, A. A., Walker, J. A., and Warman, M. L. (2000). Preparation of PCR-quality mouse genomic DNA with hot sodium hydroxide and tris (HotSHOT). BioTechniques *29*, 52, 54.

Tsutsumi, S., Kamata, N., Vokes, T. J., Maruoka, Y., Nakakuki, K., Enomoto, S., Omura, K., Amagasa, T., Nagayama, M., Saito-Ohara, F., et al. (2004). The novel gene encoding a putative transmembrane protein is mutated in gnathodiaphyseal dysplasia (GDD). Am. J. Hum. Genet *74*, 1255–1261.

Vermeer, S., Hoischen, A., Meijer, R. P. P., Gilissen, C., Neveling, K., Wieskamp, N., de Brouwer, A., Koenig, M., Anheim, M., Assoum, M., et al. (2010). Targeted next-generation sequencing of a 12.5 Mb homozygous region reveals ANO10 mutations in patients with autosomal-recessive cerebellar ataxia. Am. J. Hum. Genet *87*, 813–819.

Wang, F., Nemes, A., Mendelsohn, M., and Axel, R. (1998). Odorant receptors govern the formation of a precise topographic map. Cell *93*, 47–60.

Wang, Z., Balet Sindreu, C., Li, V., Nudelman, A., Chan, G. C.-K., and Storm, D. R. (2006). Pheromone detection in male mice depends on signaling through the type 3 adenylyl cyclase in the main olfactory epithelium. J. Neurosci *26*, 7375–7379.

Windmüller, O., Lindauer, U., Foddis, M., Einhäupl, K. M., Dirnagl, U., Heinemann, U., and Dreier, J. P. (2005). Ion changes in spreading ischaemia induce rat middle cerebral artery constriction in the absence of NO. Brain *128*, 2042–2051.

Wong, S. T., Trinh, K., Hacker, B., Chan, G. C., Lowe, G., Gaggar, A., Xia, Z., Gold, G. H., and Storm, D. R. (2000). Disruption of the type III adenylyl cyclase gene leads to peripheral and behavioral anosmia in transgenic mice. Neuron *27*, 487–497.

Wysocki, C. J., and Lepri, J. J. (1991). Consequences of removing the vomeronasal organ. J. Steroid Biochem. Mol. Biol *39*, 661–669.

Xiao, Q., Yu, K., Perez-Cornejo, P., Cui, Y., Arreola, J., and Hartzell, H. C. (2011). Voltage- and calcium-dependent gating of TMEM16A/Ano1 chloride channels are physically coupled by the first intracellular loop. Proc. Natl. Acad. Sci. U.S.A. *108*, 8891–8896.

Xu, F., Schaefer, M., Kida, I., Schafer, J., Liu, N., Rothman, D. L., Hyder, F., Restrepo, D., and Shepherd, G. M. (2005). Simultaneous activation of mouse main and accessory olfactory bulbs by odors or pheromones. J. Comp. Neurol *489*, 491–500.

Yang, C., and Delay, R. J. (2010). Calcium-activated chloride current amplifies the response to urine in mouse vomeronasal sensory neurons. J. Gen. Physiol *135*, 3–13.

Yang, H., Jin, T., Cheng, T., Jan, Y. N., and Jan, L. Y. (2011). Scan: A Novel Small-Conductance Ca2+-Activated Non-Selective Cation Channel Encoded by TMEM16F. Biophysical Journal *100*, 259a.

Yang, J., Pawlyk, B., Wen, X.-H., Adamian, M., Soloviev, M., Michaud, N., Zhao, Y., Sandberg, M. A., Makino, C. L., and Li, T. (2007). Mpp4 is required for proper localization of plasma membrane calcium ATPases and maintenance of calcium homeostasis at the rod photoreceptor synaptic terminals. Hum. Mol. Genet *16*, 1017–1029.

Yang, Y. D., Cho, H., Koo, J. Y., Tak, M. H., Cho, Y., Shim, W.-S., Park, S. P., Lee, J., Lee, B., Kim, B.-M., et al. (2008). TMEM16A confers receptor-activated calcium-dependent chloride conductance. Nature *455*, 1210–1215.

Yu, C. R., Power, J., Barnea, G., O'Donnell, S., Brown, H. E. V., Osborne, J., Axel, R., and Gogos, J. A. (2004). Spontaneous neural activity is required for the establishment and maintenance of the olfactory sensory map. Neuron *42*, 553–566.

Yu, T.-T., McIntyre, J. C., Bose, S. C., Hardin, D., Owen, M. C., and McClintock, T. S. (2005). Differentially expressed transcripts from phenotypically identified olfactory sensory neurons. J. Comp. Neurol *483*, 251–262.

Yuan, P., Leonetti, M. D., Pico, A. R., Hsiung, Y., and MacKinnon, R. (2010). Structure of the human BK channel Ca2+-activation apparatus at 3.0 A resolution. Science *329*, 182–186.

Zhainazarov, A. B., and Ache, B. W. (1995). Odor-induced currents in Xenopus olfactory receptor cells measured with perforated-patch recording. J. Neurophysiol *74*, 479–483.

Zhang, C. (2010). Gap junctions in olfactory neurons modulate olfactory sensitivity. BMC Neurosci *11*, 108.

Zhang, X., Marcucci, F., and Firestein, S. (2010). High-throughput microarray detection of vomeronasal receptor gene expression in rodents. Front Neurosci *4*, 164.

Zhao, H., and Reed, R. R. (2001). X inactivation of the OCNC1 channel gene reveals a role for activity-dependent competition in the olfactory system. Cell *104*, 651–660.

Zheng, C., Feinstein, P., Bozza, T., Rodriguez, I., and Mombaerts, P. (2000). Peripheral olfactory projections are differentially affected in mice deficient in a cyclic nucleotide-gated channel subunit. Neuron *26*, 81–91.

Zheng, J., and Zagotta, W. N. (2004). Stoichiometry and assembly of olfactory cyclic nucleotide-gated channels. Neuron *42*, 411–421.

Zippel, H. P. (1993). Historical aspects of research on the vertebrate olfactory system. Naturwissenschaften *80*, 65–76.

Zou, D.-J., Chesler, A. T., Le Pichon, C. E., Kuznetsov, A., Pei, X., Hwang, E. L., and Firestein, S. (2007). Absence of adenylyl cyclase 3 perturbs peripheral olfactory projections in mice. J. Neurosci *27*, 6675–6683.

Zou, D.-J., Chesler, A., and Firestein, S. (2009). How the olfactory bulb got its glomeruli: a just so story? Nat. Rev. Neurosci *10*, 611–618.

Zou, D.-J., Feinstein, P., Rivers, A. L., Mathews, G. A., Kim, A., Greer, C. A., Mombaerts, P., and Firestein, S. (2004). Postnatal refinement of peripheral olfactory projections. Science *304*, 1976–1979.

Zufall, F., and Munger, S. D. (2001). From odor and pheromone transduction to the organization of the sense of smell. Trends Neurosci *24*, 191–193.

Zufall, F., and Munger, S. D. (2010). Receptor guanylyl cyclases in mammalian olfactory function. Mol. Cell. Biochem *334*, 191–197.

7. PUBLICATIONS

Sievers, C., Billig, G., Gottschalk, K. & Rudel, T. Prohibitins are required for cancer cell proliferation and adhesion. PLoS ONE 5, e12735 (2010).

Billig, G. M., Pál, B., Fidzinski, P., and Jentsch, T. J. (2011). Ca2+-activated Cl− currents are dispensable for olfaction. Nat. Neurosci 14, 763–769.

8. ACKNOWLEDGMENTS

I would like to express my gratitude to Thomas Jentsch for the opportunity to prepare my doctoral thesis in his laboratory. I am grateful for his supervision and support. I appreciate the stimulating work environment, the excellent scientific training and the great technical and financial framework he provides. My thanks go to all members of the Jentsch laboratory for their help, interest and valuable advice, their continuous support and the very good working atmosphere.

I am grateful that I had the opportunity to work on the main part of this project with Balázs Pál who resumed the electrophysiological part of the functional characterization of the *Ano2* knock-out mouse model. I appreciate his technical skills and success with establishing the necessary methods for electrophysiological analysis of the olfactory system in mice. I would like to thank him for keeping his great sense of humor also in the face of time pressure and experimental challenges. I thank Pawel Fidzinski for his work on the Ca^{2+} uncaging experiments. I am obliged to Stefanie Weinert for helping with targeting vector design and gene targeting in ES cells. My special thanks go to Nicole Krönke for technical assistance and Franziska Binder for taking care of the mice. I would also like to acknowledge Tobias Stauber for answering many scientific and technical questions and for always taking the time to think with me on the rationale of experimental procedures and experimental design.